
Electronic Thesis and Dissertation Repository

6-23-2011 12:00 AM

Investigation of Subchondral Bone Abnormalities associated with Osteoarthritis using Image-Based Biomechanics

David D. McErlain
The University of Western Ontario

Supervisor
Dr. David W. Holdsworth
The University of Western Ontario

Graduate Program in Medical Biophysics
A thesis submitted in partial fulfillment of the requirements for the degree in Doctor of Philosophy
© David D. McErlain 2011

Follow this and additional works at: <https://ir.lib.uwo.ca/etd>



Part of the [Medical Biophysics Commons](#)

Recommended Citation

McErlain, David D., "Investigation of Subchondral Bone Abnormalities associated with Osteoarthritis using Image-Based Biomechanics" (2011). *Electronic Thesis and Dissertation Repository*. 183.
<https://ir.lib.uwo.ca/etd/183>

This Dissertation/Thesis is brought to you for free and open access by Scholarship@Western. It has been accepted for inclusion in Electronic Thesis and Dissertation Repository by an authorized administrator of Scholarship@Western. For more information, please contact wlsadmin@uwo.ca.

**INVESTIGATION OF SUBCHONDRAL BONE ABNORMALITIES ASSOCIATED
WITH OSTEOARTHRITIS USING IMAGE-BASED BIOMECHANICS**

Spine title: Investigation of Subchondral Bone Defects in Osteoarthritis

Thesis format: Integrated Article

by

David D. McErlain

Graduate Program in Medical Biophysics

A thesis submitted in partial fulfillment
of the requirements for the degree of
Doctor of Philosophy

The School of Graduate and Postdoctoral Studies
The University of Western Ontario
London, Ontario, Canada

© David D. McErlain 2011

THE UNIVERSITY OF WESTERN ONTARIO
School of Graduate and Postdoctoral Studies

CERTIFICATE OF EXAMINATION

Supervisor

Examiners

Dr. David W. Holdsworth

Dr. Trevor Birmingham

Supervisory Committee

Dr. James A. Johnson

Dr. S. Jeff Dixon

Dr. Abbas M Samani

Dr. Maria Drangova

Dr. David M.L. Cooper

The thesis by

David Donald McErlain

entitled:

**Investigation of Subchondral Bone Abnormalities associated with
Osteoarthritis using Image-Based Biomechanics**

is accepted in partial fulfillment of the
requirements for the degree of
Doctor of Philosophy

Date

Chair of the Thesis Examination Board

Abstract

Osteoarthritis (OA) is degenerative disease caused by a mechanical failure of both bone and cartilage, which occurs most commonly in the hands, hips, spine, and knee joints. Common risk factors for developing OA include: being over-weight, female, having joint malalignment, or a history of prior joint injury or trauma. Post-traumatic, or secondary OA is extremely common in the knee as individuals frequently suffer injuries to the ligaments or meniscus that normally provide stability to the joint. To enhance our understanding of the pathogenesis of OA, animal models are employed where the injury can be induced (i.e. knee ligament transection with partial menisectomy, ACLX) and monitored in a controlled environment. When used in conjunction with pre-clinical imaging techniques, such as micro-computed tomography (micro-CT) or magnetic resonance imaging (MRI), the longitudinal degradation of bone and cartilage can be quantitatively monitored *in vivo*. Recent evidence has identified cystic lesions within the subchondral bone of the knee, as the possible source of painful symptoms and accelerated disease progression, but little is known about their etiology.

The purpose of this thesis was to improve knowledge regarding the mechanism that causes subchondral cysts, with insight into how they affect the biomechanical abilities of OA joints. OA was induced in the rodent knee via ACLX surgery, and the bone soft tissue changes were quantified with *in vivo* micro-CT and MRI for up to 12 weeks. The composition of the cysts was correlated with end-stage histological and immunohistochemistry analysis. Thus, a more accurate definition of OA bone cysts was achieved. To assess the effect of cysts in of human bone, a study was conducted using a CT data set of early knee OA patients retrospectively. Using finite element (FE) analysis – where the strength of the bone was assigned based on the patient-specific properties derived from the image – higher stress values were found within bone surrounding cysts. Therefore, the probable mechanism of cyst expansion, stress induced bone resorption, was identified. Finally, the FE models of the bones were combined with soft tissue structures – segmented from a co-registered MRI – to produce comprehensive patient-specific FE models of the early OA knee.

Keywords

micro-computed tomography, MRI, CT, biomechanics, osteoarthritis, knee, bone, cartilage, finite element analysis, subchondral bone, cyst, human, rat

Co-Authorship Statement

Chapter 2 forms the basis for a paper entitled “Initiation and Progression of Subchondral Cysts in an *in vivo* preclinical model of Osteoarthritis” by D.D. McErlain, V. Ulici, M. Darling, J.S. Gati, V. Pitelka, F. Beier, and D.W. Holdsworth, which is in preparation for submission to the journal of Arthritis Research & Therapy. I was involved in the overall concept and study design, data collection and analysis, and drafting the manuscript. Veronica Ulici was involved in the advanced histological analysis techniques, data analysis, and manuscript preparation. Mark Darling analyzed the histological sections, read and edited the manuscript. Joseph Gati was involved in MRI data acquisition. Vasek Pitelka was involved in study design, animal care, and data collection. Frank Beier read and reviewed the manuscript. David Holdsworth, as my supervisor, oversaw all aspects of the study, and read and reviewed the manuscript.

Chapter 3 appeared as an article in Bone: 48 (2011); 639–646 entitled “Subchondral cysts create increased intra-osseous stress in early knee OA: A finite element analysis using simulated lesions” by D.D. McErlain, J.S. Milner, T.G. Ivanov, L. Jencikova-Celerin, S.I. Pollmann, and D.W. Holdsworth. As lead author, I was responsible for the original concept of the study, design of the experiments, data collection and analysis, and manuscript preparation. Jaques Milner was responsible for study design and data acquisition. Todor Ivanov was involved in the study design, data acquisition, and analysis. Lubica Jencikova-Celerin assisted in the experimental design. Steven Pollmann assisted in experimental design and data acquisition. David Holdsworth, as my supervisor, advised on the study design and data analysis. All co-authors read, reviewed, and approved the final manuscript.

Chapter 4 is in preparation for an original article in the journal of Biomechanics called “Patient-Specific Finite-Element modeling of the Early OA Knee using Image-based Material Properties” by D.D. McErlain, T.G. Ivanov, J.R. Lorusso, A. Huston, J.S. Milner, D.R. Wilson, and D.W. Holdsworth. As lead author, I conceived of the study, and was responsible for experimental design, data acquisition and analysis, and manuscript preparation. Todor Ivanov was involved in study design and data analysis. Jenna Lorusso and Allison Huston were involved in data acquisition and analysis. Jaques Milner was involved in experimental design and data acquisition. David Wilson as collaborator,

provided expertise in human knee loading. David Holdsworth supervised all aspects of study design and data acquisition and analysis. All co-authors read, reviewed, and approved the final manuscript.

Epigraph

“Opportunity is missed by most people because it is dressed in overalls and looks like work.”

- Thomas A. Edison

“Time you enjoy wasting, was not wasted.”

- John Lennon

Acknowledgments

I would like to acknowledge those individuals who have given me guidance and support throughout my time as a graduate student in the Imaging Laboratories at the Robarts Research Institute within the University of Western Ontario.

First and foremost, I would like to thank my supervisor David Holdsworth for his mentorship during my years in his group. I would like to thank my advisory committee, Jeff Dixon and Maria Drangova, for their guidance in preparing and organizing the thesis.

I would like to acknowledge the efforts of all the students and staff within the Holdsworth lab for their support and collaborative efforts that make the day-to-day operations feasible. In particular, Todor Ivanov, Jaques Milner Hristo Nikolov, Chris Norley, and Steve Pollmann, for their assistance in manners both professional and personal over the years. I am also grateful for the exceptional collaborators from other departments. Specifically, Vasek Pitelka for his assistance in project planning and animal work, and Veronica Ulici in Frank Beier's lab for excellent effort in preparing the histology data.

Finally, I would like to thank my family, my friends, and Monika who have helped me stay grounded, and encouraged me to persevere for the duration of my perpetual status as a 'student'.

Table of Contents

CERTIFICATE OF EXAMINATION	ii
Abstract.....	iii
Keywords	iv
Co-Authorship Statement.....	v
Epigraph.....	vii
Acknowledgments.....	viii
Table of Contents	ix
List of Tables	xii
List of Figures	xiii
Preface.....	xv
Chapter 1	1
1 Osteoarthritis review	1
1.1 Impact of Osteoarthritis	1
1.1.1 Bone review	4
1.1.2 Hyaline cartilage review	6
1.1.3 OA Pathology.....	8
1.2 Modeling OA	12
1.2.1 Preclinical models of OA.....	12
1.2.2 Finite element modeling	13
1.3 Musculoskeletal Imaging.....	15
1.3.1 Magnetic Resonance Imaging.....	15
1.3.2 Computed Tomography	17
1.4 Research Objectives.....	18
1.5 Thesis Organization	19

1.5.1	Chapter 2: Quantitative characterization of Subchondral Cysts in a pre-clinical model of OA.....	20
1.5.2	Chapter 3: FEA analysis of simulated SBC in the early OA knee.....	20
1.5.3	Chapter 4: Patient-Specific FEA of the Early OA Knee.....	21
1.6	References.....	22
Chapter 2	36
2	Initiation and Progression of Subchondral Cysts in an <i>in vivo</i> , preclinical model of Osteoarthritis	36
2.1	Introduction.....	36
2.2	Materials and Methods.....	38
2.2.1	Rodent model of secondary OA.....	38
2.2.2	<i>in vivo</i> 9.4 T MRI and micro-CT	38
2.2.3	Histological end-stage analysis.....	40
2.3	Results.....	42
2.3.1	Incidence and Appearance of SBC	42
2.3.2	Quantitative and Histological Analysis	43
2.4	Discussion.....	48
2.5	References.....	51
Chapter 3	55
3	Subchondral Cysts create increased Intra-osseous stress in Early Knee OA: a Finite Element Analysis using Simulated Lesions	55
3.1	Introduction.....	55
3.2	Methods.....	57
3.2.1	Early OA patient data.....	57
3.2.2	SBC design and implementation.....	57
3.2.3	Patient-Specific FE Models	58
3.2.4	Data Analysis	62

3.3 Results.....	64
3.3.1 Patient-Specific Model Creation.....	64
3.3.2 Effect of SBC on Weight-bearing.....	65
3.4 Discussion.....	69
3.5 References.....	73
Chapter 4.....	78
4 Patient-Specific Finite Element modeling of the Early OA Knee using Image-Based Material Properties	78
4.1 Introduction.....	78
4.2 Methods.....	80
4.2.1 Early OA patients and Imaging Protocols	80
4.2.2 Patient-specific FEA model creation	81
4.2.3 Model Assembly and Pilot Studies.....	82
4.2.4 Data Analysis.....	84
4.3 Results.....	84
4.4 Discussion.....	87
4.5 References.....	94
Chapter 5.....	99
5 Conclusion and Future Directions.....	99
5.1 Summary.....	99
5.2 Future Directions	99
6 Appendix.....	105
6.1 Ethics Approval	105
Curriculum Vitae	106

List of Tables

Table 2-1: Descriptive statistics for all ACLX knees containing SBC (n=8). Values are mean \pm SE from SBC diameter and superficial vBMD occurring over time (*p < 0.05, versus 8 weeks).	44
Table 3-1: Design and implementation of OA patient-specific FE models. Note, the von Mises stress (MPa) is reported from the 1 mm thick sample volume (i.e. shell region) in both models.	63
Table 4-1: Mechanical properties assigned for all tissues within our subject-specific FE models. Note the elastic moduli (MPa) for all FE elements in bones were assigned directly from the CT-volume (multiple), using a BMD to elastic modulus conversion.	84
Table 4-2: Pilot study assessing the effect of assigning different elastic moduli for bone on resultant soft tissue stress. Values shown are the mean maximum von Mises stress (\pm SE), derived from all FE elements within the femur and tibia cartila cartilage (cart.) and the lateral (lat.) and medial (med.) menisci observed in four FE models.	86
Table 4-3: Resultant maximal values for the equivalent, von Mises stress, contact pressure, and contact area within all tissues under 750 N load. Values are mean (\pm SE) for the bone inclusive, patient-specific FE models (n = 8) of the early OA knee.	87

List of Figures

Figure 2-1: Dual-modality imaging in an <i>in vivo</i> preclinical model of OA. Sagittal (a,b) and coronal (c,d) plane images of the rat knee obtained from co-registered high-field MRI high-field MRI and micro-CT.	40
Figure 2-2: Longitudinal monitoring of SBC development in the medial tibial plateau. Co-registered sagittal 9.4 T MRI (a-c) and micro-CT (d-f) sections reveal the onset of SBC formation in conjunction with a breach of the subchondral bone plate (d - arrowhead), which never fully repairs over time	43
Figure 2-3: Mean maximal diameter of SBC in the medial tibial plateau for all rodents post-ACLX surgery.....	45
Figure 2-4: Identification of the subchondral plate breach found in SBC in the OA rat knee. Sagittal micro-CT (a) and high-field MRI (b) sections were used to observe and monitor SBC <i>in vivo</i>	46
Figure 2-5: Advanced histological characterization of SBC development in a rodent model of OA.....	47
Figure 3-1: Flow chart describing the assignment of material properties, and creation of patient-specific FE models using <i>in vivo</i> CT images of the human early OA knee	59
Figure 3-2: Comparing the effect of SBC on the weight-bearing properties of the knee, using the same early stage OA knee with (right) and without (left) a synthetic SBC placed in the tibia (b - arrow)	65
Figure 3-3: Maximum von Mises stress (MPa) in knee OA patients without SBC versus with SBC (dotted line vs. solid line) within the tibia (a) and femur (b)	66
Figure 3-4: Enhanced view of elements in the sample volume (i.e. annular shell region of interest, ROI) surrounding the SBC in the femur (a,b) and tibia (c,d), under a 750 N load...	67

Figure 3-5: Linear regression analysis of maximum von Mises stress versus cyst (SBC) diameter..... 68

Figure 3-6: Effect of the simulated cysts (SBC) locations on the increased stress (MPa) within all four regions of the knee. 68

Figure 4-1: Coronal (a,c) and Sagittal (b,d) views of 3D registration for accurate cartilage segmentation using GEHC MicroView 82

Figure 4-2: Medial view of the assembly of a bone-inclusive, multi-material FE model of the early OA knee. 85

Figure 4-3: Cross-section of the lateral compartment in four FE models of the same knee. Effect of the use of a sub-model (b), or rigid body (c) or a homogeneous (d) modulus for bone on the resultant stress values within a patient-specific FE model simulation..... 88

Figure 4-4: Pattern of stress and contact pressure on the tibial surface of the left knee. Values are in MPa with (a,b) and without (c,d) the menisci present to demonstrate the weight-bearing pattern distributed onto the cartilage surface 89

Figure 5-1: Proof of concept for the use of patient-specific FEA in surgical planning of high-tibial osteotomy..... 103

Preface

This work is dedicated in memory of Louise Du.

Chapter 1

1 Osteoarthritis review

1.1 Impact of Osteoarthritis

Osteoarthritis (OA) is the most common form of arthritis that most frequently affects the diarthroidal (i.e. freely moving) joints of the hands, hips, knees, and spine [1-3]. In Canada, OA inflicts painful degeneration of joints amongst approximately 5 million people, and is projected to steadily increase to as many as 6.5 million people by 2031 [4]. However, the actual number is still unknown as incident rate predictions in these earlier studies underestimated OA prevalence when the most recent epidemiological findings are taken into account [5]. The preliminary report projected the increased incidence of OA based on the aging population in Canada alone [4], however once the most current data were evaluated, it was evident that the prevalence of self-reported arthritis within Canada will surpass projections matched with the aging population (i.e. approximately 7 million people by 2021) [5]. Therefore, the actual future burden of OA – measured through both direct and indirect costs to the patient, healthcare system, and economy – cannot be fully characterized, but will inevitably increase.

Other risk factors associated with the occurrence of OA can improve predictions within the North American population. Women tend to have higher rates of OA in the hands and knees later in life, which becomes statistically significant after the age of 50 and may coincide with the onset of menopause [2]. However, men typically have higher rates of OA in the hip throughout their lifespan [6]. Gender-related differences also occur when the effect of obesity on OA prevalence is examined. Individuals with a high body mass index (BMI) (i.e. ≥ 25 , which is calculated as $\text{weight}/\text{height}^2$ or kg/m^2) tend to have more severe OA [7], and obesity is currently understood to precede pathogenesis [2]. This effect is stronger in women with high BMI values who tend to have more severe OA and consistently report lower quality of life scores [8]. In addition, it is interesting to note that although rates of OA in the knee and hip – both weight bearing

joints – increase in step with BMI scores, the incidence of hand OA was also positively correlated with obesity [7]. An increased body mass will influence the ability and pattern of loading within an individual's joints, creating biomechanical changes in the knee where each pound of increased mass can create a 2-3 lb increase in overall force under single-leg stance [2]. The alignment of the joint with respect to the knee can greatly contribute to disproportionate force distribution and is believed to play a major role in OA. Alignment of the knee is typically assessed on standard long-leg, frontal plane radiographs wherein a line is drawn from the head of the femur to the mid-ankle [3]. The position of the knee relative to this axis determines either varus or valgus alignment: varus alignment indicates the joint forces have a medial compartment bias (i.e. bow-legged), and is found amongst patients with medial compartment OA; valgus alignment indicates the tendency for greater lateral compartment joint forces (i.e. knock-kneed), and therefore higher rates of lateral knee OA [9, 10]. However, as abnormal knee alignment has been identified in OA patients with more progressive disease and poor outcomes [9-11], its role in disease initiation remains unclear. An injury to the knee is a significant OA risk factor, and is frequently attributed as the cause of 'secondary' or post-traumatic OA. Damage to either the cruciate ligaments, most notably the anterior cruciate ligament (ACL), or the meniscus can lead to a dramatic risk for developing OA later in life [12]. Furthermore, these injuries – specifically meniscal degeneration or change in position, and ACL rupture – are thought to contribute to malalignment and loss of radiographic joint space in the OA knee, which was previously attributed solely to cartilage loss [9, 10]. In fact, despite the surgical reconstruction of an ACL tear, there remains a 50-80% chance of developing knee OA as early as 10 years post-injury [12, 13]. Consequently, young athletes (especially females) are susceptible to developing OA at a relatively early age (i.e. 35-40) [9], which will generate a large long-term, financial burden on the individual and the health care system.

The overall cost of OA is typically divided between two categories, either the direct or indirect costs. The more easily identified direct costs of OA (i.e. hospital or physician visits, drug and surgical resource use) are quite substantial in Canada, with an estimated value of \$910 million [14]. International estimates place the costs of musculoskeletal disorders at 1-2.5% of the gross national product (GNP) [15], while in Canada alone it

has been found to be as high as 3.4% of the GNP [16]. The majority of the drug costs associated with musculoskeletal disease are used for arthritis treatment [14]. Within the US, the health-care resources utilized by knee OA patients are significantly higher than those without OA; defined by annual physician and non-physician visits, and hospital stays, which are attributed to joint replacements surgery [17]. Total hip and total knee replacements (THR, TKR) were performed upon approximately 35 000 patients each within Ontario between 2001 and 2004 [18], indicating that Canada has a similar volume, and therefore financial burden, associated with these surgeries. Paterson et al. further reported that one third of these cases had a prior or subsequent THR or TKA [18], which identified further hardship and cost to OA patients beyond hospital visits. The indirect costs of OA are attributed to disability (both long and short term), productivity loss, and resultant caregiver costs due to loss of ability to perform daily tasks [19, 20]. These costs average about \$13 000 annually, which is 81% of the total annual economic burden experienced by OA patients; the majority of which is spent on caregivers [19]. Although there is significant variation in the methodology that estimates indirect costs [20], the loss of productivity associated with OA is substantial in all countries. Research and interventions aimed to increase the quality of life and allow OA sufferers to remain employed will dramatically improve the financial burden of the individual and society.

In summary, OA is a painful and progressive degenerative disease that affects an increasing number of people across the world. OA most commonly appears within the hip and knee and has been strongly linked with obesity, joint alignment, and as a result of a previous injury. Women are at a greater risk for developing OA later in life, particularly within the knee after 50 years of age. OA causes millions of Canadian to utilize health care services each year, and this creates a significant financial burden for the patient and the system; a cost that will continue to increase due to our aging population. Therefore, to inhibit the onset of invasive treatments a better understanding of the biomechanical forces acting within the OA joint, through the use of simulations of models, is required. Preclinical models can replicate 'human-like' OA pathogenesis and progression in a high-throughput and reproducible manner, in order to identify the mechanisms or features that cause failure in bone and cartilage. The pathological features found within the joint can be used as input for biomechanical simulations using

inverse kinematics or finite element analysis (FEA) within a human OA cohort. Thus, the effect of any change to the structure and function of bone and cartilage, described in detail below, can be monitored as part of a controlled experiment to better define features of OA that may identify those at greater risk for aggressive disease progression.

1.1.1 Bone review

The major tissue responsible for the biomechanical integrity of joints is bone. In addition to being responsible for adequate force distribution and load bearing, the bones in the human body provide: protection for vital organs; the rigid structure that muscles use for locomotion; production and storage of blood cells, calcium, and phosphate ions [21]. Bone tissue is distinguished as an adaptive composite material, harmoniously composed of inorganic matter, in the form of calcium-based crystals, and organic tissue, made up of three distinct cell types and a collagen matrix [22]. Altering the integrity of either bone component can initiate or cause the rapid progression of joint degradation and osteoarthritis [23, 24]. The remainder of this review will focus on the structure and function of long bones, which are one form of bone that typically form the joints commonly affected by OA.

1.1.1.1 Structure and Composition of Bone

Mature long bones, such as the femur, are divided into three regions. The largest region is called the diaphysis or shaft, which is roughly tube-shaped and produced of dense cortical bone. Approaching either end of the bone, the diameter of the shaft increases as the thickness of cortical bone decreases into the metaphysis region. Here, the bone configuration transitions into cancellous or trabecular bone within its cortex as plates of bone align themselves to support the articulating ends [25]. These ends are referred to as the epiphysis regions – which are not fully fused to the bone until adulthood, leaving an epiphyseal scar – and are almost solely constructed of trabecular bone [25]. The articulating surface of bone, which contacts the other bone across the joint, is called the subchondral bone plate. This plate covers the epiphysis and is derived from a combination of the bone lying under the periosteum (i.e. the fibrous sheath covering all bones), the calcified cartilage, and portions of the tidemark [26, 27]. The subchondral

plate varies in thickness in the weight-bearing regions to accommodate the joint load over varying articulating surfaces, such as the convex femoral head [28].

Specialized cells continually monitor the forces acting upon bone and can alter its composition and structure to accommodate different loads. Osteoblasts (it is useful to think the ‘b’ in osteoblast stands for ‘builder’ cell) are lined along most bone surfaces and are responsible for the synthesis and deposition of the organic bone matrix or osteoid [29]. As new layers of osteoid surround and eventually encase the osteoblasts, the cells differentiate into osteocytes (‘cyte’ is a homonym for ‘site’ as the osteocytes remain ‘on-site’ to regulate mineralization), which are the most abundant cell in bone [25]. Once embedded, the osteocytes form dendritic extensions throughout the canniculi network within the inorganic bone regions in order to access the blood supply and communicate amongst other osteocytes [25, 30]. The final cell type is the osteoclast (‘c’ in osteoclast can symbolize ‘cavity’) that in response to growth factors or regional signaling from the osteocytes [30] forms a large, multicellular unit responsible for the resorption (i.e. breakdown) of bone matrix [31]. The composite extracellular matrix contributes to the overall strength of bone, whose mechanical properties are continually adapted in response to load. Large diameter collagen fibers (type I), proteoglycans, and glycoproteins form the organic component matrix; the tensile strength of bone is derived from these fibers aligning themselves in staggered layers along the length of the bone [25, 32]. The small spaces within the 3D matrix allows for deposition of the mineral crystals that form the inorganic matrix. This inorganic matrix provides the entire body with a reservoir for large ions – mostly, but not limited to, calcium and phosphorus – responsible for cellular homeostasis and polarity of extracellular fluid [25]. The primary crystal that comprises over 90% of the inorganic weight of the bone is the hydroxyapatite crystal, though often the hydroxyl group is missing within bone and is therefore known as the apatite crystal [25]. The presence of apatite crystals interspersed between the collagen fibers give bone its tremendous compressive strength [32, 33].

1.1.1.2 Modeling and Remodeling of Bone

The formation of inorganic crystal from the combination of soluble calcium and phosphate within the gaps of organic matrix is termed mineralization [25, 34]. The initial

phase produces osteoid, which is an immature network of collagen and crystal formation [25]. As further precipitation and apatite crystal development continues, the spaces between the collagen fibrils become completely occupied and the size and distribution of these crystals directly establishes the mechanical properties of the bone [32, 34]. The establishment of the final shape of bone occurs during the modeling phase, while remodeling is defined as the turnover of bone without any alteration to its shape [35]. Remodeling of bone – thought to be initiated through osteocyte signaling [30] – is broken down into four stages: osteoclast activation, resorption of bone, osteoblast activation, and new bone formation [35]. The process is slightly different in cortical bone versus trabecular bone with respect to the location and method of bone resorption. Cortical bone undergoes osteonal remodeling where resorption cavities are formed along the longitudinal direction of the bone. These cavities are subsequently lined with osteoblasts that closely follow the path laid out by the osteoclasts [31, 35] while they produce osteoid. Within trabecular bone, the resorption cavity (called a Howship lacunae) is much smaller and more closely resembles a pit [35]. Remodeling occurs continually within bones in response to external forces as described by Wolff's law in 1892, which essentially states that bone will model itself along the direction of the applied loads in proportion to their magnitude [36-38].

1.1.2 Hyaline cartilage review

Hyaline cartilage is a thin connective tissue that covers the ends of bone in articular joints. Cartilage has a tremendous ability to resist compression and distribute loads to the underlying bone, and provides a nearly frictionless along the joint surfaces despite being only a few millimeters thick [39-41]. Furthermore, the chondrocytes (cartilage contains only one cell type) responsible for the life-long maintenance of this tissue reside in a rather extreme environment that is largely without blood supply or innervation [39, 41]. Though the actual thickness, composition, and mechanical properties of cartilage may vary between anatomical site and species, the major structural components and general organization of hyaline cartilage is identical for all synovial joints in mammals [41].

1.1.2.1 Structure and Composition of Cartilage

As stated above, the chondrocyte is the only cellular component within cartilage and therefore is responsible for the coordination of tissue repair or maintenance. While only accounting for 1% of the total volume of cartilage [41, 42], chondrocytes control the degradation and turnover of extra cellular matrix, and the synthesis and repair of several types of collagen, proteoglycans and macromolecules [41, 43]. The extra-cellular matrix is the major structural component of cartilage and is composed of water, collagen, and proteoglycans [42, 44]. The most common form of collagen in cartilage is Type II (versus Type I in bone), which is distributed as a lattice network of cross-banded fibrils and provides much of the form and tensile strength [42, 44]. Proteoglycans are large molecules, with a net negative charge, that are distributed within the collagen framework and assist in maintaining tissue hydration and shape [39]. The large molecule is made of a protein core that is bonded to several glycosaminoglycan chains, thus forming an aggrecan that can bind with hyaluronic acid and create a large, stable tissue network [42]. The fixed-charge density provided by these closely packed aggrecans provide an osmotic pressure, which pulls water into the extra-cellular matrix and controls its rate of displacement under deformation [41, 44].

Cartilage is divided among four zones that change in concentration of water, proteoglycans, and collagen with depth, along with alterations in the shape and organization of the chondrocytes [42, 44]. The superficial zone is the thinnest and is defined by tight packed layers of thin collagen fibrils, and a high concentration of flattened chondrocytes lying parallel to the articular surface [45]. Relative to other zones, the superficial zone has the highest amount of water – as a result, fluid flow is greatest – and the lowest proteoglycan concentration [44]. This design is believed to protect the cartilage from repeated, compressive loads by allowing fluid exchange between the synovium and the cartilage (i.e. decreasing the coefficient of friction) without allowing any of the large molecules to pass from the synovial fluid into the extra-cellular matrix, which would alter its ability to bear subsequent loads [44, 45]. The transitional zone contains rounded chondrocytes capable of synthesizing large diameter collagen fibrils that are distributed in a more random orientation than the superficial

zone. The radial zone is composed of the largest collagen fibrils that are aligned perpendicular to the articulating surface, some of which extend beyond the tidemark into the calcified cartilage zone [46]. Here, the chondrocytes are large, spherically shaped and stacked perpendicular to the joint surface whereas the concentration of water and proteoglycans are at their lowest and highest, respectively [42]. Beneath the tidemark lies the zone of calcified cartilage. This zone has collagen fibrils oriented perpendicular to the articular surface, similar to the radial zone, though there are no proteoglycans present and the chondrocytes are generally smaller [39]. Therefore, the calcified cartilage zone has relatively low cellular metabolism and, due to its integration with the underlying subchondral bone, is responsible for transmitting joint loads and controlling any possible bone intrusion [47].

The repetitive loads inflicted on cartilage throughout daily life can occur in rapid succession and cause deformation of the tissue. This deformation must be resisted or quickly reversed to prevent strain beyond the physiological limits of the tissue [48]. Under normal circumstances, cartilage achieves this due to the interaction of the 3D collagen network with the interstitial fluid [41, 44]. Consequently, hyaline cartilage is thought to behave as a viscoelastic solid [44, 49] under weight bearing. Under compression, cartilage will deform and create a pressure change within the extra-cellular matrix, causing the extrusion of fluid into the joint space. There is frictional resistance to flow as the pore size between aggrecans in the matrix decreases as it is deformed, which prevents rapid effusion of fluid [44]. The volume of the matrix is subsequently reduced, drawing the neighboring anionic proteoglycans closer together. The resultant effect is two-fold: an increased charge density within the deformed cartilage, causing an intermolecular repulsive force that resist further compression; a greater osmotic pressure gradient preventing further loss of fluid [49, 50]. This effect provides the elastic force that allows cartilage to return to its original shape, whilst the fluid re-enters the tissue matrix.

1.1.3 OA Pathology

In the early stages of OA research, scientists found it difficult to define such a complex disease that affects many distinct tissues. Altman et al. began to distinguish between

forms of OA by separating patients into groups based on how the disease originated – either idiopathic (or primary, with unknown origin) or secondary (or post-traumatic) – in hopes of developing therapeutic criteria [1]. The currently accepted definition considers joints with OA as a form of organ failure, rather than a disease affecting individual tissues, which have different pathological behaviors [51]. Thus, the breakdown of the entire joint, not only the cartilage and bone, but the synovium, ligaments, joint capsule, and surrounding muscles can contribute to OA progression or be affected by the arthritic tissue, which has lost most of its biomechanical integrity. However, the debate continues as the tissue in which the disease originates is inconsistent, even within primary or secondary OA patients. Many feel that OA is initiated within the cartilage - as surface fibrillation or lesions, loss of proteoglycans, vascular invasion from the bone have been found in histological investigations [43, 52]. The opposing view states that the subchondral bone is the instigator of OA, which alters the mechanical properties of the joint through remodeling due to damage caused by trauma or repetitive strain [24, 51]. The remodeling therefore alters the supportive role of bone in distributing the weight-bearing forces inflicted on the overlying cartilage, and the increased stress leads to breakdown within cartilage [53]. Alternatively, the case can be made that when cartilage damage occurs – in the form of a horizontal lesion or matrix degradation – normal loads will cause prolonged or abnormal deformation creating the subsequent high stress concentrations in the bone that lead to its injury [41, 43]. Nonetheless, as more advanced research is performed, particularly the development of models to simulate or initiate the damage to bone and cartilage (discussed in Section 1.2), it is apparent that pathological remodeling of bone and degeneration of cartilage are the primary motivators for the progression and associated symptoms of OA.

1.1.3.1 Cartilage Failure

As previously mentioned, the progression of OA within articular cartilage is summarized into three major events: initial damage and modification of the extracellular matrix, the response of the chondrocytes to this damage, and the eventual loss of tissue, as the response becomes insufficient [41]. The preliminary damage is likely caused by surface fibrillation that disrupts the matrix structure and alters the fluid flow in the superficial

zone [54, 55]. The matrix continues to lose the concentration and aggregation of proteoglycans while the length of glycosaminoglycan chains decrease, which can lead to swelling and softening of the cartilage [41, 43]. This is referred to as chondromalacia since the swollen cartilage is susceptible to greater damage under loading [45]. The chondrocytes respond to the breakdown of the surrounding matrix by removing the damaged aggrecans and releasing cytokines in an effort to rebuild matrix components [40]. Under histological analysis, the chondrocytes begin to appear in clusters within cartilage, representing an advanced stage of disease where the anabolic recovery cannot match the rate of tissue degradation [40, 41].

Finally, as the remaining chondrocytes try to match the synthesis of new tissue with the loss of surrounding matrix, breakdown occurs and cartilage thickness decreases. Chondrocytes, due to the loss of their protective surroundings, become damaged or undergo apoptosis [52, 56, 57]. The few remaining chondrocytes in their altered form begin to secrete the improper form of collagen (i.e. Type I), which is more fibrous and affects the mechanical behavior of cartilage [58]. In addition, the tidemark region will either duplicate or advance closer to the surface [51, 59] as capillaries penetrate from the subchondral bone plate into the calcified cartilage region [59]. The presence of calcified regions within the cartilage [60] above the tidemark further exacerbates the damage causing greater stress within the tissue, and subsequent destruction [61].

1.1.3.2 Subchondral Bone Adaptations

The major adaptation within bones affected by OA is an increased rate of remodeling that leads to changes in the structure, composition, and biomechanical behavior of joints [62, 63]. This remodeling leads to typical features described amongst arthritic bone: an increase in bone mineral density (BMD; defined as bone mineral mass divided by total volume), the presence of osteophytes along the joint margins, edema, or the formation of cyst-like lesions [62-66]. Early research indicated that BMD increased in step with OA progression [67, 68], though recent studies suggest a more complex relationship. The presence of sclerosis or a thickening of the subchondral bone region, normally observed using planar radiographs, is proposed evidence for higher BMD in OA joints. However, this bone is in an immature, disorganized osteoid form [69, 70] as the remodeling process

is never completed. Perhaps due to repeated loads that necessitate an anabolic response to prevent further damage to the trabeculae, the apposition of apatite crystals may continue in the subchondral bone leading to a pathological increase in stiffness at the joint surface [71]. Hence, many believe OA initiates within the subchondral bone first; where an increase in local BMD, caused by sclerosis or advancement of the tidemark, compromises the integrity of overlying cartilage [24, 62, 71]. Remarkably, the area of cancellous bone immediately adjacent to the sclerotic bone volume can become osteoporotic, or lose a dramatic amount bone volume [63, 69, 72]. The eventual collapse or deformity of the joint surface occurs after repetitive loading and wear of the dysfunctional cartilage, which directly exposes the subchondral bone to contact and leads to greater pain and disability.

An emerging feature found in degenerative OA joints is intra-osseous lesions, especially in the hip or knee [65, 73-75]. Commonly known as subchondral cysts (SBC), or 'pseudocysts', they were first described by Ondrouch [64] though little is known about their origin. SBC appear as spherical or elliptical voids in weight-bearing regions of the joint and may be accompanied by a sclerotic margin, which is detectable on radiographs [76]. There are two proposed methods for SBC formation - synovial intrusion or bony contusion. Synovial intrusion requires a breach of the subchondral bone and a loss of cartilage that allows synovial fluid into the bone. An inflammatory response ensues that can lead to further cyst expansion and joint degeneration [23]. The second theory proposed involves a traumatic force applied to the joint that causes a 'bone bruise' to form deep to the surface. The contusion – and subsequent micro-fracture of trabecular bone – causes swelling or fluid accumulation, otherwise known as edema and the formation of SBC. Magnetic resonance imaging (MRI) studies of knee OA patients have found the presence of SBC in approximately 25 - 47% of symptomatic knees [75, 77], though advances in imaging methods may provide a more accurate detection [78, 79]. The effect of SBC on the weight-bearing ability of the OA knee has not been determined, but recent simulations by Durr et al. using finite element analysis (FEA) found that the presence of SBC in hip OA caused increased stress in the femoral head [80]. Durr further explained that stress-induced bone resorption could be the cause for SBC to expand over time [80], which also occurred within a preclinical model of post-

traumatic knee OA [81]. SBC have been longitudinally monitored in human knees once, and the results were startling; those patients who had SBC lost a greater amount of cartilage, and a higher risk of TKR versus patients without SBC [77]. It is evident that further research into the exact pathological mechanisms – using reproducible preclinical and biomechanical models of knee – of SBC expansion is required to better characterize this population of OA patients at an elevated risk of disease progression.

1.2 Modeling OA

1.2.1 Preclinical models of OA

To facilitate investigations into the pathogenesis of OA, animal models that can reproduce human-like OA must be used. This provides researchers with a consistent supply of arthritic bone and cartilage for histological analyses on the cellular origin of OA [82, 83]. With the ability to monitor the initiation and progression of OA at a controlled and predictable rate, there is a greater possibility of elucidating the tissue of origin [40, 62, 84] and identifying mechanisms for therapeutic targets. Furthermore, as the symptoms of OA don't always precede actual joint damage [2], it is difficult to reliably capture the pathogenesis without animal models. The onset of OA or joint injury is typically done in two ways. The first involves the targeting of specific tissues with an adjuvant injection into the joint capsule [85, 86]. This method has been very effective at inducing an aggressive form of arthritis in a short timeframe, which is preferred among researchers interested in the biochemical cause of cartilage degradation [87]. The alternative method for OA induction involves the surgical destabilization of the joint via ligament transection and/or meniscectomy. Surgical destabilization simulates the post-traumatic form, or secondary OA by altering the mechanical load distribution and creating focal stress increases, which manifest with damage to both bone and cartilage [88].

Currently, there is a lack of standardization among pre-clinical models of OA, which can lead to discrepancies in response to experimentally treatments [88]. Larger animals, such as dogs or rabbits, were originally preferred as a post-traumatic OA model that provided

sufficient tissue samples for histology and could be monitored with medical imaging techniques [82, 89]. However, the rat may be preferable for biomedical research; rodents have a number of advantageous features: they are ideal for experiments in pain mechanisms [90], rats can be handled easily due to their size, they are cost-effective with respect to longitudinal care, and rats are compatible with genetic manipulation or expression studies [91]. Furthermore, advances in musculoskeletal imaging techniques (described in Section 1.3) allow for longitudinal, *in vivo* imaging of rodent joints with sufficient spatial resolution to quantify the deterioration of bone and cartilage [92-94]. Rat knee OA is induced by severing the anterior cruciate ligament and removing the anterior horn of the medial meniscus (i.e. partial meniscectomy) (ACLX), which mimics a common injury that occurs in humans, and ruptures of the ACL are often accompanied with damage to the meniscus [95, 96]. Therefore, we have chosen the rat ACLX model for our research to assess the longitudinal changes to cartilage and bone – with the specific intent to monitor the presence and composition of SBC – as it is well known that this injury is the dominant risk factor for secondary OA in human knees [12].

1.2.2 Finite element modeling

Although animal models provide a tremendous utility in capturing the composition of joints as OA progresses, they are limited in their ability to assess the effect these changes have on the dynamic response of the tissue. In addition, the species used are quadrupedal and have weight-bearing loads distributed over all four limbs, which limits the translation of relevant biomechanical information to human joints. One method of monitoring or predicting the biomechanical performance of tissue involves finite element analysis (FEA). FEA simulations can solve for the distribution and magnitude of forces experienced in bone and cartilage using linear algebraic equations within a matrix [97]. Thus, complex shapes or geometries, such as the wedged-shaped meniscus or a network of trabecular bone, can be discretized into a series of elements – with known geometry and deformation behavior – within a 3D mesh. Forces acting on the mesh model will create deformations measured at the nodes of the elements, which provide regional values for stress and strain based on the assigned material properties [97, 98]. Consequently, FEA studies of pathological tissue specimens or a patient's joint can predict whether

mechanical failure will occur without actually destroying the tissue(s) of interest. Moreover, injuries to bone, cartilage, or meniscus can be simulated in healthy or normal joints to assess the potential implications on the overall biomechanical health of the joint [99, 100].

The development of a FEA model involves four major steps: design of a geometry, conversion to a mesh of elements, assignment of material properties, and application of boundary conditions [97, 98, 101]. The earliest geometries used in the development of FEA analysis of bone and cartilage involved the use of simple shapes and patterns to represent tissue [80]. Currently, the unique geometry of a bone or layer of cartilage can be derived directly from Computed Tomography (CT) or Magnetic Resonance Imaging (MRI) scans through the use of surface rendering or semi-automated segmentation [102, 103]. The conversion from geometric to FE model involves choosing the element shape and its properties. The elements need to have an edge length that is small enough to capture the unique features of the tissue of interest, such as the curvilinear shape of femoral cartilage, without escalating computational resources beyond the hardware limitations. Hexahedral elements are preferred over tetrahedral shaped elements [99, 103], as they have more nodes per element, but can cause large increases in solution times. In addition, ‘block’ elements may not accurately depict small differences in the object’s geometry (i.e. cartilage or trabecular thinning) without using extremely small elements (sub-mm edge length), which will further increase the number of elements and resources needed. Thus, linear tetrahedral elements are employed for the majority of FEA studies where an accurate depiction subject or specimen-specific variation is desired [104-106]. Assigning material properties to the elements is a critical step in FEA design. Previous work examining the compressive behavior of bones validated the assigned modulus of elasticity (or Young’s modulus) through mechanical testing of using *ex vivo* specimens [107]. Modern material property assignment – derived from previous work correlating CT-derived BMD with the elastic modulus measured at several anatomical sites [105, 108, 109] – uses a non-linear relationship to apply heterogeneous mapping within the 3D model of bones [110]. Advanced FEA research of cartilage or meniscal behavior has attempted to replicate the heterogeneous material mapping, but these experiments usually involve a small section of the joint to reduce

complexity and solution time [99, 111]. Finally, boundary conditions are assigned to the model in order to prevent any non-physiological motions or abnormal stress concentrations [97]. These are particularly important when analyzing either a subsection of a joint (i.e. medial tibial plateau), or a biopsy-cadaveric specimen that will lack the supporting ligaments and tendons normally responsible for movement beyond the normal range of motion [97, 99, 103, 112, 113].

1.3 Musculoskeletal Imaging

The use of medical imaging techniques to monitor OA in humans has been consistent for clinical and experimental applications since their inception. Radiographs were exclusively employed early in OA research, and the disease severity was assessed with a grading scale that is still in use to date [114]. Although 2D in nature, radiographs give excellent detail of the bony joint margins, aiding in the detection of osteophytes and subchondral plate sclerosis [72]. Cartilage loss is typically inferred from the loss of joint space (i.e. the tibia and femoral condyles appear closer together on anterior-posterior, weight-bearing radiographic views); unfortunately this approach is inconsistent in predicting the severity of damage [115]. In addition, as imaging technology advanced – through the development of high-resolution MRI and CT imaging – in parallel with the consensus that OA is a whole ‘organ’ or joint disease [116], there is an opportunity to gain critical knowledge of musculoskeletal (MSK) disorders using 3D quantitative imaging. The remainder of this review will focus on the imaging modalities and techniques used throughout the experiments in the subsequent chapters, namely MRI and CT.

1.3.1 Magnetic Resonance Imaging

MRI scans produce images of articular joints by placing the desired object into a large magnetic field whereby protons (i.e. typically from water or fat nuclei found in cartilage or marrow, respectively) within the tissue align themselves to the field [117]. Radio frequency (RF) pulses are applied to excite the nuclei into a higher energy state. Once the RF pulse is shut off the nuclei begin to dissipate this energy while returning to their

original state, which provides the signal that is monitored by dedicated antennae [118]. Variations in tissue composition (i.e. water content) will affect the two time constants during the relaxation phase – T1, or spin-lattice relaxation, and T2, or spin-spin relaxation – and will produce differences in the signals measured and produce contrast within the image [118].

MRI is ideal for imaging the soft tissue structures within the knee, such as cartilage and muscle, which have a relatively high degree of water content [119]. Unfortunately, cartilage within the knee is normally between 1 - 3 mm thick and clinical scanners typically have voxel dimensions exceeding 1 mm [118], which inhibits the amount of measurable signal. To enhance the diagnostic quality of the image, many recommend the use of scanners with greater field strengths, as high as 3 - 7 Tesla (T) [10, 116, 118, 120], for greater measurement precision of the deteriorating tissue. Furthermore, with the addition of contrast agents, through intravenous injections or directly in the joint capsule, investigators have begun to differentiate the early pathogenesis in cartilage and the bone marrow edema, which has been highly correlated with SBC formation [78, 121, 122].

Preclinical MSK imaging has evolved rapidly with the introduction of dedicated MRI scanners with field strengths from 4.7 - 14 T [89, 117]. These scanners can improve the signal to noise ratio (SNR) sufficiently to produce reconstructed image volumes with isotropic voxels dimensions as low as $50 \mu\text{m}^3$ [94, 123]. Often the longer scan times required for such high resolution precludes *in vivo* MSK imaging [89], but Goebel et al. have been successful in acquiring longitudinal images of the rodent knee at 7 T [123]. Furthermore, the development of custom RF coil hardware, specifically designed for rat knee imaging, has improved cartilage measurements [124]. It is important to note that although MRI has exquisite soft tissue contrast, it has a very limited ability to quantify the structure of bone due to its low water content [118]. Few studies have tried to compensate for this by combining MRI with another imaging modality such as CT, in order to fully characterize both the bony and soft tissue degeneration occurring in OA [125]. Moreover, with the known chemical shift artifacts associated with imaging the

bone-cartilage interface [126], it is paramount that MSK research continues to improve any deficiencies that effect the accurate measurement of bone and soft tissue geometries.

1.3.2 Computed Tomography

CT scanners produce high-resolution, 3D image volumes (i.e. voxel dimensions < 1 mm) that are reconstructed from a series of 2D x-ray projections [118, 127]. CT imaging has been used clinically since the early 1970s [127] for quantitative imaging of throughout the entire body, including articular joints [118, 128]. Traditional scanners have an x-ray tube mounted opposite a detector to a gantry system that rotates around the stationary specimen [118, 127, 128]. The signal in the reconstructed images is created based on the linear x-ray attenuation coefficient for the tissue that the projection passed through. These values are scaled into the standardized Hounsfield units (HU) – where values for water and air are 0 and -1000, respectively – for quantitative analyses of tissue density [128]. Bone is visualized easily in CT volumes, as it is composed of material with high atomic number, and if a patient or specimen is scanned with a tissue calibration phantom, the mineral density (BMD) throughout the entire bone or joint can be easily quantified [118, 128]. Compared to MRI, CT scans are relatively inexpensive and have rapid acquisition times that are suitable for high-throughput analyses of multiple specimens [81]. CT scans are often preferred clinically to MRI, as they can produce valuable bone and joint data, even when there are metal components surgically introduced into the joint [129]. However, the soft tissue contrast when compared to MRI is quite poor without the use of iodinated contrast agents [129].

Preclinical micro-CT scanners have been in use for more than a decade [113, 130]. With smaller x-ray tube focal spots (i.e. 10 μm) and high-resolution detectors, micro-CT scanners can produce 3D image volumes with isotropic voxel spacing of 10 - 150 μm^3 [131]. Thus, the scanners are scaled down in a manner where rodents induced with OA act as ‘virtual patients’ while being monitored for changing BMD or other bony deformities similar to humans [131]. Additionally, non-destructive micro-CT imaging has proven to be an essential tool for MSK anthropology research, as unique bones or museum specimens can be examined in great detail, in a manner that does not require that the specimen be dissected or destroyed [132, 133]. High-resolution MSK imaging

of human biopsy or cadaveric specimens with micro-CT is popular amongst those seeking to quantify the 3D morphology of trabecular bone [134]. Although the use of *in vivo* micro-CT of humans [135]– specifically the radius or distal tibia – has begun in clinical studies [136], the ionizing radiation dose the patients are exposed to needs to be carefully monitored.

The latest progress in CT imaging research involves the use of the image, and its quantified material properties, for non-destructive mechanical testing simulations using FEA. It is known that the risk of bone fracture is related to its strength, which was previously derived solely from BMD measurements [137]. FEA models of trabecular bone specimens, with detailed geometries that are derived from micro-CT volumes, can predict the fracture risk more accurately than BMD alone, when correlated with mechanical testing to failure [138]. Furthermore, as the BMD for an entire bone is easily calculated from CT images, the 3D heterogeneous material properties can be assigned throughout using a non-linear density-to-modulus conversion [110]. Therefore, within a single CT or micro-CT volume a user can assign different a Young's modulus on a voxel-by-voxel basis in 3D that is regionally specific. This approach has been successfully implemented in various iterations for both *ex vivo* [104] and *in vivo* [139] data sets using either human [140] or rodent [93] joints.

1.4 Research Objectives

Medical imaging of the MSK system has been an invaluable resource for the advancement of our understanding about the mechanisms contributing to the etiology of knee OA. Quantitative analyses of common features associated with disease progression – such as changes in bone mineral density and cartilage thickness – provide accurate measures of the joint's response to altered biomechanical loads, which can be monitored longitudinally in humans or preclinical models. However, degenerative changes to the underlying subchondral bone that lead to the development of cyst-like lesions are poorly understood. Due to the fact that recent evidence has identified the presence of subchondral cysts as a risk factor for greater loss of cartilage and chance of requiring

joint replacement surgery, there is an urgent requirement to characterize the initiation of the cyst and identify the mechanisms by which they expand, or cause joint deformity and greater pain.

The overall purpose of this thesis is to further our understanding about subchondral bone cysts, which are prevalent in knee OA, through the use of advanced medical imaging applications combined with FEA analysis. The specific goals required to achieve this are to:

- 1) Observe and measure the initiation and progression of subchondral cysts *in vivo* as they occur in a well-known preclinical model of knee OA.
- 2) Determine the effect that subchondral cysts may have on the weight-bearing ability of the human knee through FEA using simulated lesions within a cohort of early knee OA patients.
- 3) Further develop patient-specific FEA applications using anatomical images, and material property data that is derived directly from co-registered CT and MRI images, which can be applied retrospectively to existing OA patient data.

1.5 Thesis Organization

The achievement of the goals outlined above is presented in the following three chapters. One of these chapters is in press [141] in the journal of Bone, while the remaining two are in preparation for submission to other peer-reviewed journals. Following this work is a summary chapter, which will include the conclusions and the future applications of this work.

1.5.1 Chapter 2: Quantitative characterization of Subchondral Cysts in a pre-clinical model of OA

In this chapter, the development of subchondral cysts (SBC) is monitored longitudinally in a rodent model of knee OA. Male, Sprague-Dawley underwent anterior cruciate ligament resection with partial medial meniscectomy (ACLX), and the joint damage was observed with *in vivo* micro-CT and high-field MRI. The rat knee was imaged using a dedicated pre-clinical micro-CT and a 9.4 T MRI under a single dose of anaesthetic prior to ACLX and at 1, 2, and 3 months post-ACLX. SBC formation was monitored in 3D using registration to characterize the bone and soft tissue changes simultaneously. The size of the SBC were measured and compared between modalities, and the bone mineral density above the SBC was quantified using micro-CT. After the final time point, the animals were sacrificed and the knee joint was processed with standard OA histological grading and advanced immuno-histochemistry techniques to further characterize the tissue within the SBC, and assess the local cellular response. SBC were found to increase in size over time, and similar to human OA, produced greater damage to the overlying cartilage. The superficial BMD increased over time, and combined with the histological characterization within the lesion, it is evident that the nomenclature of these intra-osseous lesions should change to reflect the presence of necrotic tissue that modifies its shape according to the mechanical forces applied during normal gait.

1.5.2 Chapter 3: FEA analysis of simulated SBC in the early OA knee

This chapter describes the response of bones in the human knee to the presence of SBC under normal weight-bearing. Twenty early-stage OA patients had CT scans of the affected knee prior to arthroscopic surgery. This image data was used retrospectively to produce patient-specific FEA models of the bones, wherein a simulated SBC with a defined shape and size could be inserted into the model. The material properties of the bones were assigned on a voxel-by-voxel basis using an established BMD to modulus conversion, and the SBC was assigned negligible properties (mimicking a void). All FEA models underwent vertically loading of approximately one body weight. The

values for peri-cystic, intra-osseous stress were measured in each model and compared to a duplicate model of the same knee that did not contain the simulated SBC. The presence of SBC lead to greater peri-cystic stress values under weight-bearing, which were concentrated near the joint space. This work adds to our knowledge of the mechanism by which the SBC may expand or lead to further damage of subchondral bone and cartilage.

1.5.3 Chapter 4: Patient-Specific FEA of the Early OA Knee

Chapter 4 describes the implementation of comprehensive FEA models of the early OA knee, which incorporates all of the relevant bone and soft tissue structures required during single leg stance. Eight early knee OA patients had CT and MRI scans acquired prior to arthroscopic surgery. The CT image was registered to, and the FEA model was designed in, the MRI volume's 3D space. This allowed for more accurate semi-automatic segmentation of the cartilage, tendon, and menisci, as the bony borders of these structures were truncated by the CT-segmented bones. All tissue geometries were imported into a commercial FEA software package. Soft-tissue structures were assigned material properties based on established literature values, while the bone had multi-material properties assigned using the same BMD to modulus conversion from Chapter 3. The results indicate that without the inclusion of heterogeneous material mapping of the bone, the values and pattern of stress distributed in cartilage and menisci are misrepresented. Furthermore, the common use of a sub-model – only including a section of the entire knee to reduce computational requirements and complexity – for FEA analysis of soft-tissues will exacerbate this issue due to uneven distribution of the applied load. Therefore, comprehensive modeling of all structures within the knee – incorporating the full dimensions and region-specific material properties – was achieved using dual-modality 3D imaging, which can be applied in future clinical trials.

1.6 References

1. Altman, R., et al., *Development of criteria for the classification and reporting of osteoarthritis. Classification of osteoarthritis of the knee. Diagnostic and Therapeutic Criteria Committee of the American Rheumatism Association.* Arthritis Rheum, 1986. **29**(8): p. 1039-49.
2. Felson, D.T., et al., *Osteoarthritis: new insights. Part 1: the disease and its risk factors.* Ann Intern Med, 2000. **133**(8): p. 635-46.
3. Hunter, D.J. and D.R. Wilson, *Imaging the role of biomechanics in osteoarthritis.* Rheum Dis Clin North Am, 2009. **35**(3): p. 465-83.
4. Badley, E.M. and P.P. Wang, *Arthritis and the aging population: projections of arthritis prevalence in Canada 1991 to 2031.* J Rheumatol, 1998. **25**(1): p. 138-44.
5. Perruccio, A.V., J.D. Power, and E.M. Badley, *Revisiting arthritis prevalence projections--it's more than just the aging of the population.* J Rheumatol, 2006. **33**(9): p. 1856-62.
6. Felson, D.T., et al., *The prevalence of knee osteoarthritis in the elderly. The Framingham Osteoarthritis Study.* Arthritis Rheum., 1987. **30**(8): p. 914-918.
7. Grotle, M., et al., *Obesity and osteoarthritis in knee, hip and/or hand: an epidemiological study in the general population with 10 years follow-up.* BMC Musculoskelet Disord, 2008. **9**: p. 132.
8. Kopec, J.A., et al., *Development of a population-based microsimulation model of osteoarthritis in Canada.* Osteoarthritis Cartilage, 2010. **18**(3): p. 303-11.
9. Englund, M., *The role of biomechanics in the initiation and progression of OA of the knee.* Best Pract Res Clin Rheumatol, 2010. **24**(1): p. 39-46.

10. Hunter, D.J., et al., *Structural factors associated with malalignment in knee osteoarthritis: the Boston osteoarthritis knee study*. J Rheumatol, 2005. **32**(11): p. 2192-9.
11. Martel-Pelletier, J. and J.P. Pelletier, *Is osteoarthritis a disease involving only cartilage or other articular tissues?* Eklem Hastalik Cerrahisi, 2010. **21**(1): p. 2-14.
12. Ratzlaff, C.R. and M.H. Liang, *New developments in osteoarthritis. Prevention of injury-related knee osteoarthritis: opportunities for the primary and secondary prevention of knee osteoarthritis*. Arthritis Res Ther, 2010. **12**(4): p. 215.
13. Lohmander, L.S., et al., *The long-term consequence of anterior cruciate ligament and meniscus injuries: osteoarthritis*. Am J Sports Med, 2007. **35**(10): p. 1756-69.
14. Health, C., *Arthritis in Canada. An ongoing challenge (Cat # H39-4/14-2003E)*, 2003, Health Canada: Ottawa. p. 1
15. March, L.M. and C.J. Bachmeier, *Economics of osteoarthritis: a global perspective*. Baillieres Clin Rheumatol, 1997. **11**(4): p. 817-34.
16. Coyte, P.C., et al., *The economic cost of musculoskeletal disorders in Canada*. Arthritis Care Res, 1998. **11**(5): p. 315-25.
17. Wright, E.A., et al., *Impact of knee osteoarthritis on health care resource utilization in a US population-based national sample*. Med Care, 2010. **48**(9): p. 785-91.
18. Paterson, J.M., et al., *Provider volumes and early outcomes of primary total joint replacement in Ontario*. Can J Surg, 2010. **53**(3): p. 175-83.
19. Gupta, S., et al., *The economic burden of disabling hip and knee osteoarthritis (OA) from the perspective of individuals living with this condition*. Rheumatology (Oxford), 2005. **44**(12): p. 1531-7.

20. Xie, F., *The need for standardization: a literature review of indirect costs of rheumatoid arthritis and osteoarthritis*. *Arthritis Rheum*, 2008. **59**(7): p. 1027-33.
21. McCarthy, E.F., Frassica, F.J., *Anatomy and Physiology of Bone*, in *Pathology of Bone and Joint Disorders: with Clinical and Radiographic Correlation* 1998, Saunders: Philadelphia. p. 25-50.
22. Porter, G.A., et al., *Bone*, in *Histology for Pathologists* 1997, Lippencott-Raven: Philadelphia. p. 85-105.
23. Sabokbar, A., et al., *Macrophage-osteoclast differentiation and bone resorption in osteoarthrotic subchondral acetabular cysts*. *Acta Orthop Scand*, 2000. **71**(3): p. 255-61.
24. Radin, E.L. and R.M. Rose, *Role of subchondral bone in the initiation and progression of cartilage damage*. *Clinical Orthopaedics & Related Research*, 1986(213): p. 34-40.
25. Buckwalter, J.A., et al., *Bone biology. I: Structure, blood supply, cells, matrix, and mineralization*. *Instr.Course Lect.*, 1996. **45**: p. 371-386.
26. Clark, J.M. and J.D. Huber, *The structure of the human subchondral plate*. *J Bone Joint Surg.Br.*, 1990. **72**(5): p. 866-873.
27. Milz, S. and R. Putz, *Quantitative morphology of the subchondral plate of the tibial plateau*. *J Anat.*, 1994. **185 (Pt 1)**: p. 103-110.
28. Wei, H.W., et al., *The influence of mechanical properties of subchondral plate, femoral head and neck on dynamic stress distribution of the articular cartilage*. *Med Eng Phys*, 2005. **27**(4): p. 295-304.
29. Ducy, P., T. Schinke, and G. Karsenty, *The osteoblast: a sophisticated fibroblast under central surveillance*. *Science*, 2000. **289**(5484): p. 1501-1504.

30. Bonewald, L.F., *The amazing osteocyte*. J Bone Miner Res, 2011. **26**(2): p. 229-38.
31. Boyce, B.F., Z. Yao, and L. Xing, *Osteoclasts have multiple roles in bone in addition to bone resorption*. Crit Rev Eukaryot Gene Expr, 2009. **19**(3): p. 171-80.
32. Landis, W.J., *The strength of a calcified tissue depends in part on the molecular structure and organization of its constituent mineral crystals in their organic matrix*. Bone, 1995. **16** (5): p. 533-544.
33. Forwood, M.R., *Mechanical effects on the skeleton: are there clinical implications?* Osteoporos Int, 2001. **12**(1): p. 77-83.
34. Ea, H.K., et al., *Articular cartilage calcification in osteoarthritis: Insights into crystal-induced stress*. Arthritis Rheum, 2010. **2010**(22): p. 27761.
35. Buckwalter, J.A., et al., *Bone biology. II: Formation, form, modeling, remodeling, and regulation of cell function*. Instr.Course Lect., 1996. **45**: p. 387-399.
36. Rubin, C.T. and M.R. Hausman, *The cellular basis of Wolff's law. Transduction of physical stimuli to skeletal adaptation*. Rheum Dis Clin North Am, 1988. **14**(3): p. 503-517.
37. Cowin, S.C., A.M. Sadegh, and G.M. Luo, *An evolutionary Wolff's law for trabecular architecture*. J Biomech Eng, 1992. **114**(1): p. 129-36.
38. Turner, C.H., *On Wolff's law of trabecular architecture*. J Biomech, 1992. **25**(1): p. 1-9.
39. Huber, M., S. Trattnig, and F. Lintner, *Anatomy, biochemistry, and physiology of articular cartilage*. Invest Radiol, 2000. **35**(10): p. 573-580.
40. Goldring, M.B. and S.R. Goldring, *Articular cartilage and subchondral bone in the pathogenesis of osteoarthritis*. Ann N Y Acad Sci, 2010. **1192**: p. 230-7.

41. Buckwalter, J.A., H.J. Mankin, and A.J. Grodzinsky, *Articular cartilage and osteoarthritis*. Instr Course Lect, 2005. **54**: p. 465-80.
42. Buckwalter, J.A. and H.J. Mankin, *Articular cartilage: tissue design and chondrocyte-matrix interactions*. Instr.Course Lect.Journal of Bone and Joint Surgery, 1998. **47**: p. 477-486.
43. Buckwalter, J.A. and H.J. Mankin, *Articular cartilage: degeneration and osteoarthritis, repair, regeneration, and transplantation*. Instr.Course Lect., 1998. **47**: p. 487-504.
44. Wong, M. and D.R. Carter, *Articular cartilage functional histomorphology and mechanobiology: a research perspective*. Bone, 2003. **33**(1): p. 1-13.
45. Cohen, N.P., R.J. Foster, and V.C. Mow, *Composition and dynamics of articular cartilage: structure, function, and maintaining healthy state*. J Orthop.Sports Phys.Ther., 1998. **28**(4): p. 203-215.
46. Redler, I., et al., *The ultrastructure and biomechanical significance of the tidemark of articular cartilage*. Clin Orthop., 1975(112): p. 357-362.
47. Oegema, T.R., Jr., et al., *The interaction of the zone of calcified cartilage and subchondral bone in osteoarthritis*. Microsc.Res.Tech., 1997. **37**(4): p. 324-332.
48. Barker, M.K. and B.B. Seedhom, *The relationship of the compressive modulus of articular cartilage with its deformation response to cyclic loading: does cartilage optimize its modulus so as to minimize the strains arising in it due to the prevalent loading regime?* Rheumatology (Oxford), 2001. **40**(3): p. 274-84.
49. Mow, V.C., M.H. Holmes, and W.M. Lai, *Fluid transport and mechanical properties of articular cartilage: a review*. J Biomech, 1984. **17**(5): p. 377-94.
50. Guilak, F., et al., *The deformation behavior and mechanical properties of chondrocytes in articular cartilage*. Osteoarthritis Cartilage, 1999. **7**(1): p. 59-70.

51. Radin, E.L., et al., *Mechanical determinants of osteoarthritis*. Semin Arthritis Rheum, 1991. **21**(3 Suppl 2): p. 12-21.
52. Findlay, D.M., *Vascular pathology and osteoarthritis*. Rheumatology (Oxford), 2007. **46**(12): p. 1763-8.
53. Burr, D.B., *The importance of subchondral bone in osteoarthritis*. Curr.Opin.Rheumatol, 1998. **10**(3): p. 256.
54. Mankin, H.J., *The reaction of articular cartilage to injury and osteoarthritis (first of two parts)*. New England Journal of Medicine, 1974. **291**(24): p. 1285-92.
55. Mankin, H.J. and A.Z. Thrasher, *Water content and binding in normal and osteoarthritic human cartilage*. J Bone Joint Surg Am, 1975. **57**: p. 76.
56. Colwell, C.W., Jr., et al., *In vivo changes after mechanical injury*. Clin Orthop Relat Res, 2001(391 Suppl): p. S116-23.
57. McKinley, T.O., et al., *Basic science of intra-articular fractures and posttraumatic osteoarthritis*. J Orthop Trauma, 2010. **24**(9): p. 567-70.
58. Grynblas, M.D., D.R. Eyre, and D.A. Kirschner, *Collagen type II differs from type I in native molecular packing*. Biochim.Biophys.Acta, 1980. **626**(2): p. 346-355.
59. Revell, P.A., et al., *Metabolic activity in the calcified zone of cartilage: observations on tetracycline labelled articular cartilage in human osteoarthritic hips*. Rheumatol Int., 1990. **10**(4): p. 143-147.
60. Suan, J.C., et al., *4 T MRI of chondrocalcinosis in combination with three-dimensional CT, radiography, and arthroscopy: a report of three cases*. Skeletal Radiol, 2005. **34**(11): p. 714-21.
61. Ea, H.K., et al., *Articular cartilage calcification in osteoarthritis: insights into crystal-induced stress*. Arthritis Rheum, 2011. **63**(1): p. 10-8.

62. Burr, D.B., *The importance of subchondral bone in the progression of osteoarthritis*. J Rheumatol Suppl, 2004. **70**: p. 77-80.
63. Fazzalari, N.L., et al., *Assessment of cancellous bone quality in severe osteoarthrosis: bone mineral density, mechanics, and microdamage*. Bone, 1998. **22**(4): p. 381-8.
64. Ondrouch, A.S., *Cyst formation in osteoarthritis*. J Bone Joint Surg Br, 1963. **45**: p. 755-60.
65. Ostlere, S.J., L.L. Seeger, and J.J. Eckardt, *Subchondral cysts of the tibia secondary to osteoarthritis of the knee*. Skeletal Radiol, 1990. **19**(4): p. 287-9.
66. Taljanovic, M.S., et al., *Bone marrow edema pattern in advanced hip osteoarthritis: quantitative assessment with magnetic resonance imaging and correlation with clinical examination, radiographic findings, and histopathology*. Skeletal Radiol, 2008. **37**(5): p. 423-31.
67. Hannan, M.T., et al., *Bone mineral density and knee osteoarthritis in elderly men and women. The Framingham Study*. Arthritis Rheum, 1993. **36**(12): p. 1671-80.
68. Hart, D.J., et al., *The relationship of bone density and fracture to incident and progressive radiographic osteoarthritis of the knee: the Chingford Study*. Arthritis Rheum, 2002. **46**(1): p. 92-99.
69. Karvonen, R.L., et al., *Periarticular osteoporosis in osteoarthritis of the knee*. J Rheumatol, 1998. **25**(11): p. 2187-2194.
70. Mansell, J.P., J.F. Tarlton, and A.J. Bailey, *Biochemical evidence for altered subchondral bone collagen metabolism in osteoarthritis of the hip*. Br.J Rheumatol, 1997. **36**(1): p. 16-19.
71. Grynpas, M.D., et al., *Subchondral bone in osteoarthritis*. Calcif Tissue Int, 1991. **49**: p. 20-26.

72. Buckland-Wright, C., *Subchondral bone changes in hand and knee osteoarthritis detected by radiography*. Osteoarthritis Cartilage., 2004. **12 Suppl A**: p. S10-S19.
73. Bianchi, S., et al., *Expansile subchondral degenerative bone cyst secondary to osteoarthritis*. Can Assoc Radiol J, 1995. **46**(4): p. 308-10.
74. Crawford, R., et al., *Expansion of an osteoarthritic cyst associated with wear debris: a case report*. J Bone Joint Surg Br, 1998. **80**(6): p. 990-3.
75. Kornaat, P.R., et al., *Osteoarthritis of the knee: association between clinical features and MR imaging findings*. Radiology, 2006. **239**(3): p. 811-7.
76. Bancroft, L.W., J.J. Peterson, and M.J. Kransdorf, *Cysts, geodes, and erosions*. Radiol Clin North Am, 2004. **42**(1): p. 73-87.
77. Tanamas, S.K., et al., *The association between subchondral bone cysts and tibial cartilage volume and risk of joint replacement in people with knee osteoarthritis: a longitudinal study*. Arthritis Res Ther, 2010. **12**(2): p. R58.
78. Crema, M.D., et al., *Contrast-enhanced MRI of subchondral cysts in patients with or at risk for knee osteoarthritis: The MOST study*. Eur J Radiol, 2009.
79. Marra, M.D., et al., *MRI features of cystic lesions around the knee*. Knee, 2008. **15**(6): p. 423-38.
80. Durr, H.D., et al., *The cause of subchondral bone cysts in osteoarthrosis: a finite element analysis*. Acta Orthop Scand, 2004. **75**(5): p. 554-8.
81. McErlain, D.D., et al., *Study of subchondral bone adaptations in a rodent surgical model of OA using in vivo micro-computed tomography*. Osteoarthritis Cartilage, 2008. **16**(4): p. 458-69.
82. Cook, J.L., et al., *The OARSI histopathology initiative - recommendations for histological assessments of osteoarthritis in the dog*. Osteoarthritis Cartilage, 2010. **18 Suppl 3**: p. S66-79.

83. Gerwin, N., et al., *The OARSI histopathology initiative - recommendations for histological assessments of osteoarthritis in the rat*. Osteoarthritis Cartilage, 2010. **18 Suppl 3**: p. S24-34.
84. Buckwalter, J.A., *Articular cartilage injuries*. Clin Orthop Relat Res, 2002(402): p. 21-37.
85. Hui, W., et al., *Oncostatin M in combination with tumor necrosis factor alpha induces cartilage damage and matrix metalloproteinase expression in vitro and in vivo*. Arthritis Rheum, 2003. **48**(12): p. 3404-18.
86. Pelletier, J.P., et al., *The in vivo effects of intraarticular corticosteroid injections on cartilage lesions, stromelysin, interleukin-1, and oncogene protein synthesis in experimental osteoarthritis*. Lab Invest, 1995. **72**(5): p. 578-86.
87. van den Berg, W.B., *Lessons from animal models of osteoarthritis*. Curr Rheumatol Rep, 2008. **10**(1): p. 26-9.
88. Ameye, L.G. and M.F. Young, *Animal models of osteoarthritis: lessons learned while seeking the "Holy Grail"*. Curr Opin Rheumatol, 2006. **18**(5): p. 537-47.
89. Batiste, D.L., et al., *Ex vivo characterization of articular cartilage and bone lesions in a rabbit ACL transection model of osteoarthritis using MRI and micro-CT*. Osteoarthritis Cartilage, 2004. **12**(12): p. 986-96.
90. Henry, J.L., *Molecular events of chronic pain: from neuron to whole animal in an animal model of osteoarthritis*. Novartis Found Symp, 2004. **260**: p. 139-45; discussion 145-53, 277-9.
91. Appleton, C.T., et al., *Global analyses of gene expression in early experimental osteoarthritis*. Arthritis Rheum, 2007. **56**(6): p. 1854-68.
92. Appleton, C.T., et al., *Forced mobilization accelerates pathogenesis: characterization of a preclinical surgical model of osteoarthritis*. Arthritis Res Ther, 2007. **9**(1): p. R13.

93. Boyd, S.K., E. Szabo, and P. Ammann, *Increased bone strength is associated with improved bone microarchitecture in intact female rats treated with strontium ranelate: A finite element analysis study*. Bone, 2011.
94. Goebel, J.C., et al., *New trends in MRI of cartilage: Advances and limitations in small animal studies*. Biomed Mater Eng, 2010. **20**(3): p. 189-94.
95. Mitsou, A. and P. Vallianatos, *Meniscal injuries associated with rupture of the anterior cruciate ligament: a retrospective study*. Injury, 1988. **19**(6): p. 429-31.
96. Shirakura, K., et al., *Untreated acute anterior cruciate ligament tears of the knee: progression and the influence of associated injuries*. Knee Surg Sports Traumatol Arthrosc, 1995. **3**(2): p. 62-7.
97. Panagiotopoulou, O., *Finite element analysis (FEA): applying an engineering method to functional morphology in anthropology and human biology*. Ann Hum Biol, 2009. **36**(5): p. 609-23.
98. Srirekha, A. and K. Bashetty, *Infinite to finite: an overview of finite element analysis*. Indian J Dent Res, 2010. **21**(3): p. 425-32.
99. Shirazi, R. and A. Shirazi-Adl, *Computational biomechanics of articular cartilage of human knee joint: effect of osteochondral defects*. J Biomech, 2009. **42**(15): p. 2458-65.
100. Zielinska, B. and T.L. Donahue, *3D finite element model of meniscectomy: changes in joint contact behavior*. J Biomech Eng, 2006. **128**(1): p. 115-23.
101. Fagan, M.J., S. Julian, and A.M. Mohsen, *Finite element analysis in spine research*. Proc Inst Mech Eng H, 2002. **216**(5): p. 281-98.
102. Crawford, R.P., W.S. Rosenberg, and T.M. Keaveny, *Quantitative computed tomography-based finite element models of the human lumbar vertebral body: effect of element size on stiffness, damage, and fracture strength predictions*. J Biomech Eng, 2003. **125**(4): p. 434-8.

103. Donahue, T.L., et al., *A finite element model of the human knee joint for the study of tibio-femoral contact*. J Biomech Eng, 2002. **124**(3): p. 273-80.
104. Chen, G., et al., *A new approach for assigning bone material properties from CT images into finite element models*. J Biomech, 2010. **43**(5): p. 1011-5.
105. Austman, R.L., et al., *The effect of the density-modulus relationship selected to apply material properties in a finite element model of long bone*. J Biomech, 2008. **41**(15): p. 3171-6.
106. Ramos, A. and J.A. Simoes, *Tetrahedral versus hexahedral finite elements in numerical modelling of the proximal femur*. Med Eng Phys, 2006. **28**(9): p. 916-24.
107. Cristofolini, L., et al., *Mechanical testing of bones: the positive synergy of finite-element models and in vitro experiments*. Philos Transact A Math Phys Eng Sci, 2010. **368**(1920): p. 2725-63.
108. Chen, G., et al., *A new approach for assigning bone material properties from CT images into finite element models*. J Biomech, 2009.
109. Morgan, E.F., H.H. Bayraktar, and T.M. Keaveny, *Trabecular bone modulus-density relationships depend on anatomic site*. J Biomech, 2003. **36**(7): p. 897-904.
110. Austman, R.L., et al., *Development of a customized density-modulus relationship for use in subject-specific finite element models of the ulna*. Proc Inst Mech Eng H, 2009. **223**(6): p. 787-94.
111. Gu, K.B. and L.P. Li, *A human knee joint model considering fluid pressure and fiber orientation in cartilages and menisci*. Med Eng Phys, 2011.
112. Oxnard, C.E., *Thoughts on bone biomechanics*. Folia Primatol (Basel), 2004. **75**(4): p. 189-201.

113. van Rietbergen, B., *Micro-FE analyses of bone: state of the art*. Adv Exp Med Biol, 2001. **496**: p. 21-30.
114. Kellgren, J.H. and J.S. Lawrence, *Radiological assessment of osteo-arthrosis*. Ann Rheum Dis, 1957. **16**(4): p. 494-502.
115. Wenham, C.Y. and P.G. Conaghan, *Imaging the painful osteoarthritic knee joint: what have we learned?* Nat Clin Pract Rheumatol, 2009. **5**(3): p. 149-58.
116. Roemer, F.W., F. Eckstein, and A. Guermazi, *Magnetic resonance imaging-based semiquantitative and quantitative assessment in osteoarthritis*. Rheum Dis Clin North Am, 2009. **35**(3): p. 521-55.
117. Jacobs, R.E. and S.R. Cherry, *Complementary emerging techniques: high-resolution PET and MRI*. Curr Opin Neurobiol, 2001. **11**(5): p. 621-9.
118. Augat, P. and F. Eckstein, *Quantitative imaging of musculoskeletal tissue*. Annu Rev Biomed Eng, 2008. **10**: p. 369-90.
119. Eckstein, F., D. Burstein, and T.M. Link, *Quantitative MRI of cartilage and bone: degenerative changes in osteoarthritis*. NMR Biomed, 2006. **19**(7): p. 822-54.
120. Kraff, O., et al., *An eight-channel transmit/receive multipurpose coil for musculoskeletal MR imaging at 7 T*. Med Phys, 2010. **37**(12): p. 6368-76.
121. Doria, A.S., et al., *Reliability and Convergent Validity of Different BOLD MRI Frameworks for Data Acquisition in Experimental Arthritis*. Acad Radiol, 2011. **18**(5): p. 615-25.
122. Nissi, M.J., et al., *Estimation of mechanical properties of articular cartilage with MRI - dGEMRIC, T2 and T1 imaging in different species with variable stages of maturation*. Osteoarthritis Cartilage, 2007. **15**(10): p. 1141-8.

123. Goebel, J.C., et al., *In vivo high-resolution MRI (7T) of femoro-tibial cartilage changes in the rat anterior cruciate ligament transection model of osteoarthritis: a cross-sectional study*. Rheumatology, 2010. **49**(9): p. 1654-1664.
124. Rengle, A., et al., *A dedicated two-element phased array receiver coil for high resolution MRI of rat knee cartilage at 7T*. Conf Proc IEEE Eng Med Biol Soc, 2007. **1**: p. 3886-9.
125. Batiste, D.L., et al., *High-resolution MRI and micro-CT in an ex vivo rabbit anterior cruciate ligament transection model of osteoarthritis*. Osteoarthritis Cartilage, 2004. **12**(8): p. 614-26.
126. Peh, W.C. and J.H. Chan, *Artifacts in musculoskeletal magnetic resonance imaging: identification and correction*. Skeletal Radiol, 2001. **30**(4): p. 179-91.
127. Hounsfield, G.N., *Computerized transverse axial scanning (tomography). I. Description of system*. Br J Radiol, 1973. **46**(552): p. 1016-22.
128. Adams, J.E., *Quantitative computed tomography*. Eur J Radiol, 2009. **71**(3): p. 415-24.
129. West, A.T., T.J. Marshall, and P.W. Bearcroft, *CT of the musculoskeletal system: what is left is the days of MRI?* Eur Radiol, 2009. **19**(1): p. 152-64.
130. Pistoia, W., et al., *High-resolution three-dimensional-pQCT images can be an adequate basis for in-vivo microFE analysis of bone*. J Biomech Eng, 2001. **123**(2): p. 176-83.
131. Schambach, S.J., et al., *Application of micro-CT in small animal imaging*. Methods, 2010. **50**(1): p. 2-13.
132. Veselka, N., et al., *A bony connection signals laryngeal echolocation in bats*. Nature, 2010. **463**(7283): p. 939-42.

133. McErlain, D.D., et al., *Micro-computed tomography of a 500-year-old tooth: technical note*. Can Assoc Radiol J, 2004. **55**(4): p. 242-5.
134. Zhang, Z.M., et al., *Micro-CT and mechanical evaluation of subchondral trabecular bone structure between postmenopausal women with osteoarthritis and osteoporosis*. Osteoporos Int, 2009.
135. Burrows, M., D. Liu, and H. McKay, *High-resolution peripheral QCT imaging of bone micro-structure in adolescents*. Osteoporos Int, 2010. **21**(3): p. 515-20.
136. Burghardt, A.J., et al., *Reproducibility of direct quantitative measures of cortical bone microarchitecture of the distal radius and tibia by HR-pQCT*. Bone, 2010. **47**(3): p. 519-28.
137. Griffith, J.F., K. Engelke, and H.K. Genant, *Looking beyond bone mineral density : Imaging assessment of bone quality*. Ann N Y Acad Sci, 2010. **1192**: p. 45-56.
138. Bevill, G., F. Farhamand, and T.M. Keaveny, *Heterogeneity of yield strain in low-density versus high-density human trabecular bone*. J Biomech, 2009. **42**(13): p. 2165-70.
139. Kalkwarf, H.J., T. Laor, and J.A. Bean, *Fracture risk in children with a forearm injury is associated with volumetric bone density and cortical area (by peripheral QCT) and areal bone density (by DXA)*. Osteoporos Int, 2011. **22**(2): p. 607-16.
140. Mawatari, T., et al., *Vertebral strength changes in rheumatoid arthritis patients treated with alendronate, as assessed by finite element analysis of clinical computed tomography scans: a prospective randomized clinical trial*. Arthritis Rheum, 2008. **58**(11): p. 3340-9.
141. McErlain, D.D., et al., *Subchondral cysts create increased intra-osseous stress in early knee OA: A finite element analysis using simulated lesions*. Bone, 2011. **48**(3): p. 639-46.

Chapter 2

2 Initiation and Progression of Subchondral Cysts in an *in vivo*, Preclinical Model of Osteoarthritis

2.1 Introduction

Osteoarthritis is an articular joint disorder that leads to mechanical failure within the knee, causing great pain and deformity. Although this degenerative joint disease is common throughout North America [1-3], there is an unmet need for pharmacological therapies that modify or reverse the structural damage and alleviate symptoms [4]. The erosion of cartilage (i.e. full thickness lesions or loss of surface integrity) is commonly associated with OA [5, 6]. However, changes to the underlying subchondral bone – through variations in the local mineral density, or the rapid unorganized remodeling seen after injury – is likely to cause greater structural damage to joints by inhibiting local blood flow [7] and the formation of sclerosis [8, 9]. Moreover, it has been shown that alterations in the biomechanical integrity of subchondral bone can modify the ability of the overlying cartilage to function normally [4, 10, 11]. Identifying pathological features within patients exhibiting aggressive disease progression is paramount to ensuring the proper treatment regiment is used, whether that includes traditional therapy, pharmacological interventions, or varying surgical interventions [12].

Intra-osseous lesions, commonly known as subchondral bone cysts (SBC), ‘pseudo-cysts’ or ‘geodes’ [13, 14], within OA knees have recently been associated with greater pain and disease progression. SBC were first identified by Ondrouch [15] and Landells [16] in the weight-bearing regions of the femur, patella, and shoulder within arthritic patients, though the exact cause is not well known. Currently, there are two conflicting theories proposed for the origin of SBC in OA: ‘synovial fluid intrusion’, via a breach in the subchondral plate caused by the diminished local cartilage, leading to a rapid inflammatory response; or ‘bony contusion’, where stresses in the bone below the joint surface, due to trauma or thinned cartilage, exceed the functional strength of the

trabecular bone, causing micro-fracture, edema, and focal bone resorption [14, 15, 17]. However, those earlier studies only utilized histological techniques, and were limited to analyzing tissue that was removed during a surgical procedure, such as total knee replacement [19], where the diseased or lesion-occupied area is severely degraded. Concurrently, the ability to monitor the progression of these cystic lesions *in vivo* has been limited to retrospective analyses of patients' MRI scans [18-20], which provide limited information regarding the onset of SBC formation. Given recent evidence that associates the presence of SBC – found in 25 to 47 % of painful OA knees – with greater cartilage loss and increased risk of joint replacement amongst OA patients [18, 21], it is apparent that this subchondral bone feature warrants further study.

Pre-clinical models can provide valuable insights into the cause of SBC by producing the similar patterns of cartilage and bone degeneration seen in human post-traumatic, or secondary OA. The surgical induction of a partial medial menisectomy, combined with a severed anterior cruciate ligament (ACLX), in the rodent knee can emulate several aspects of secondary OA, including SBC, in a predictable and reproducible manner [22, 23]. The use of preclinical imaging, specifically micro-computed tomography (micro-CT), has become routine in the past decade for longitudinal, *in vivo* monitoring of disease progression [24]. When combined with the superior soft-tissue contrast provided by high-field magnetic resonance imaging (MRI) [25, 26], dual-modality imaging has the potential to characterize the complete joint degradation [23] and differentiate the bone, fluid, and tissue components found within SBC [16]. However, few studies have capitalized on the ability to incorporate image registration, which ensures any observations are conducted at the same 3D location within each volume.

The purpose of this study was to use dual modality, *in vivo* micro-imaging techniques to monitor the development of intra-osseous lesions occurring in an established pre-clinical model of OA. By combining our quantitative measurements with end-stage histology and immunohistochemistry, we hope to accurately determine the contents within these SBC and identify the possible existence of an open communication between the subchondral bone and joint space. Thus, these advanced analyses will provide valuable insight into the origin of OA SBC – through the possible confirmation of one of the

prevailing theories – while simultaneously capturing the progressive and disorganized turnover of OA bone. Furthermore, we hope to more accurately define this increasingly prevalent condition that is associated with more actively degenerative OA.

2.2 Materials and Methods

2.2.1 Rodent model of secondary OA

As described previously, our preclinical model of OA involves an anterior cruciate ligament transection with partial medial meniscectomy (ACLX), performed on male Sprague-Dawley rats [22, 27]. The surgery involved an incision through the medial joint compartment of the right knee, with subsequent ligament bisection and removal of the anterior horn of the medial meniscus. All animal manipulations were approved by the Animal Use Subcommittee at the University of Western Ontario. Eight ($n = 8$, body weight = 416 ± 6 g) rats were used throughout the time-course of the imaging experiments, and were permitted free activity with food and water *ad libitum* between scanning sessions. The rats were scanned with our dual-modality imaging protocol prior to ACLX, and at 4, 8, and 12 weeks post-ACLX.

2.2.2 *In vivo* 9.4 T MRI and micro-CT

A custom animal bed was used for both MRI and CT scanning, where the rat's hindlimbs were secured to inhibit any flexion of the knee between scans. This bed could be detached and re-attached to either scanner, allowing for quick transition between the MR and CT scanner facilities with little change in rat knee flexion.

All rats were anaesthetized by an intra-muscular injection of ketamine (100 mg/ml), xylazine (5 mg/ml), and saline prior to imaging, and the dose was maintained at 0.1ml/100 g body mass for each successive imaging session. High-field MR images were acquired using a 9.4 T scanner (Varian, Germany). Slices were acquired in the sagittal plane with a 2 cm surface coil using a 3D FLASH sequence (TE = 3.0 ms, TR = 10ms, FA = 5.5, 12 averages), which required approximately 32 min. of scan time. The 3D reconstructed images had a matrix of $256 \times 256 \times 64$ voxels, with spacing of

0.1 × 0.1 × 0.15 mm. Once MRI was complete, the surface coil was removed and a tissue-calibration phantom was placed near the joint line, prior to micro-CT imaging. This phantom mimics the radiographic properties of cortical bone (SB3, Gamex RMI, Middleton, US), which ensured the CT data set would be scaled in Hounsfield units and calibrated in volumetric bone mineral density (vBMD, mg/cm³ of hydroxyapatite) [22, 28]. Micro-CT scans were performed using a bench-top scanner (explore Locus, General Electric Health Care, London, Canada) with the following parameters: 210 views over 1° increments, 5 exposures averaged per view, using 80 kV and 0.45 mA, isotropic reconstructed voxels with 0.045 mm spacing, scan time approximately 17 minutes.

The reconstructed data sets were examined in multi-planar reformatted view on a workstation using MicroView (v.2.11, General Electric Health Care) software. Due to unequal voxel spacing between the MRI and micro-CT data sets the MRI data was resampled, using in-house software, to an isotropic voxel spacing of 0.045 mm, which allowed for rigid-body registration and the creation of a dual modality image of the knee (Figure 2-1). The presence of cysts were detected in all three anatomical planes, however, the coronal plane was chosen when the maximum diameter of the lesion was determined, which was defined as the maximum extent of focal loss of bone in the medial-lateral direction within the affected joint compartment. Thus, for each rat knee volume per time point, the user identified the lesions as focal areas of bone loss that were spherical or ellipsoidal in shape, and appeared adjacent the joint surface of either the femur or tibia. Upon verification that a SBC had been identified within the dual-modality images, volumetric bone mineral density measurements (vBMD) of the subchondral bone, in the region between the SBC and the articular surface, were acquired using the region of interest tool (ROI) within the micro-CT volume. Cylindrical regions of interest (ROIs), with a diameter and depth of 0.68 mm and 0.23 mm, respectively, were placed in the superficial regions of bone, and values for vBMD were calculated within each rodent knee over time. Therefore, an accurate depiction of the changes to the bone, which occurred *in vivo* as OA progressed and the SBC modified its size, was obtained. In addition, the maximal diameter of the lesion was recorded from the CT data, while the corresponding MRI section was utilized to attempt to identify the heterogeneous tissue types – such as a fibrous or fluid filled cavity – that appeared within the lesion space.

Finally, the diameter of the SBC, occurring in each OA rat knee, was compared between time points to allow for longitudinal analysis of lesion size and any possible changes in SBC composition.

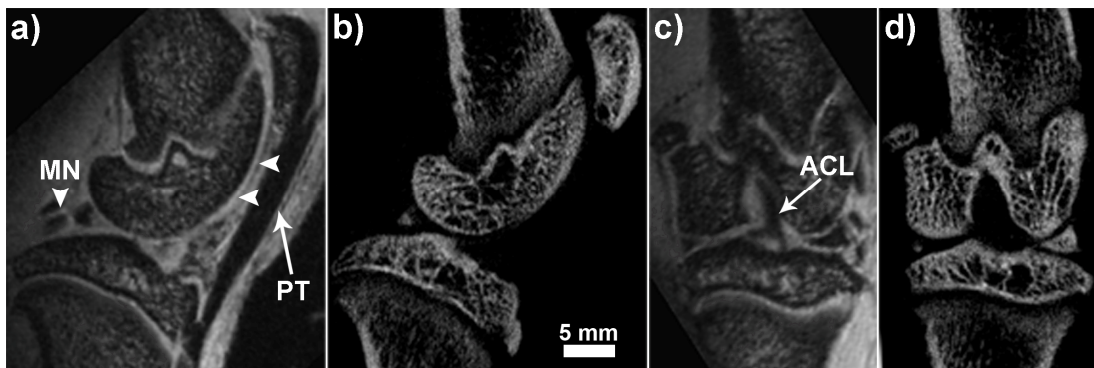


Figure 2-1: Dual-modality imaging in an *in vivo* preclinical model of OA. Sagittal (a,b) and coronal (c,d) plane images of the rat knee obtained from co-registered high-field MRI high-field (a,c) and micro-CT (c,d). The MRI volume was resampled to isotropic voxel dimensions prior to registration, which allowed the delineation of bone and non-bone components in the meniscus (MN) and the accurate depiction of tendon (PT - patellar tendon), ligament (ACL - anterior cruciate ligament), and cartilage (horizontal arrowheads).

2.2.3 Histological end-stage analysis

At 12 weeks post-ACLX, the rats were euthanized by means of intracardial perfusion with 4% paraformaldehyde. Both hind limbs were disarticulated and decalcified in 15% EDTA/glycerol (pH = 7.3) for up to 5 weeks. The knee joints were subsequently embedded in paraffin wax and the medial joint compartment was serially sectioned in the sagittal plane. Sections were selected based on their proximity to the SBC that were identified, and measured from the medial bony joint margin, in the micro-CT images. Three sections, each 5 μ m thick were stained with Safranin-O/Fast Green, and the Osteoarthritis Research Society International (OARSI) scoring method was used to grade and stage OA degradation in the medial joint compartment in the ACLX joint [29]. The grade and stage of both joint surfaces was determined, for three slides within each knee joint, by a skilled observer. The OA score was calculated by multiplication of the grade

and stage values for each slide (a minimum score of 0 represents no OA degradation and a score of 24 represents the maximum degree of OA), and the total score was achieved from the mean score of all slides for each joint surface.

Chemical reagents were purchased from Sigma, unless stated otherwise. Antibodies were purchased from Abcam (ALPL # ab95462; Cathepsin K # ab37259), and Santa Cruz (HRP conjugated goat anti-mouse # sc-2005, HRP conjugated goat anti-rabbit # sc-2004). DAB substrate-chromogen was purchased from Dako (K3468). Knee joint sections, each 5 μ m thick, were dewaxed, re-hydrated (Xylene, 100% Ethanol, 95%, 70% and H₂O), and stained with hematoxylin/eosin, Safranin O/fast green and Picrosirius red, using standard protocols. Immuno-histochemistry protocols were performed as previously described [30] with some modifications. Re-hydrated sections were incubated in 3% hydrogen peroxide for 15 min at room temperature, followed by incubation in preheated (2 min at 100 °C) 10 mM sodium citrate solution (pH = 6.0) for 30 min at 97 °C (ALPL) or 0.1 % TritonX-100 for 10 min (Cathepsin K). Subsequently, they were blocked with 5% goat serum, and incubated with primary antibodies against ALPL and Cathepsin K over night at 4 °C, followed by HRP conjugated- secondary antibody for 1 hour at 4 °C. After washing, the sections were incubated for 2 - 5 min with DAB substrate solution, washed and mounted. Counter-staining was performed with methyl green for 5 min, which was followed by dehydration and mounting of the sections. Images were taken with a Retiga EX camera, connected to a Leica DMRA2 microscope. Primary image analyses were performed using Openlab 4.0.4 and Photoshop software.

Quantitative values for vBMD and SBC diameter – amongst the knees containing a SBC that could be monitored throughout all time points – were compared using a one-way ANOVA with a Tukey's post-hoc test. Differences for each parameter, between all time points, were considered significant for $p < 0.05$. The OARSI grade, between the ACLX and contralateral limb of the same animal, was compared using a Wilcoxon signed rank test.

2.3 Results

2.3.1 Incidence and Appearance of SBC

The *in vivo*, dual-modality imaging protocol was completed in less than 1 hr using a single dose of anesthetic. The reconstructed and registered data sets provided excellent visualization of the major structural components in the rat knee including the subchondral bone, articular cartilage, and meniscus, which contains both bone and non-bone components (Figure 2-1). The presence of SBC were found in all animals throughout the time-course of study (12 weeks), and primarily occurred in the medial tibial plateau (MTP). Focal areas of bone resorption were identified initially in the micro-CT volume among 6 of 8 rat knees (75 %) at 4 weeks post-ACLX, and all knees contained at least one cyst by the endpoint. A second cyst appeared in 63% (i.e. 5 out of 8) of ACLX rats by the final time point (12 weeks). The SBC were primarily pyriform or spherical shaped and were located underneath a breach of the subchondral bone plate, which was more easily distinguished in the micro-CT volume due to its higher spatial resolution (Figure 2-2). The MRI revealed a heterogeneous signal within the SBC that was higher at earlier time points, though not as high as cartilage, and gradually degraded over time revealing a transition from a more fluid-filled to fibrous-filled cavity (Fig 2-2 b,c). The diameter of the SBC increased over time, and was significantly higher at 12 weeks post-ACLX than 4 weeks (Figure 2-3, $p = 0.013$). When comparing measurements between imaging modalities, the micro-CT derived SBC diameters were usually overestimated versus the MRI measurements (Table 2-1), though overall the values were within 10%.

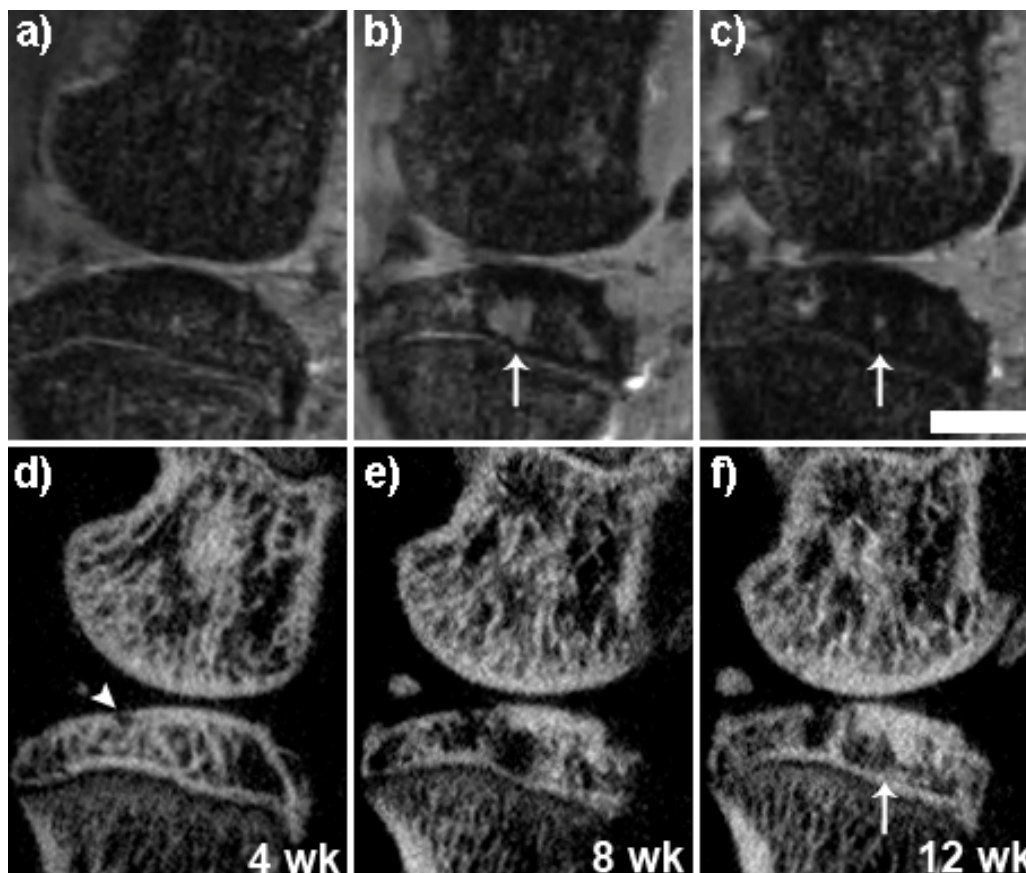


Figure 2-2: Longitudinal monitoring of SBC development in the medial tibial plateau. Co-registered sagittal 9.4 T MRI (a-c) and micro-CT (d-f) sections reveal the onset of SBC formation in conjunction with a breach of the subchondral bone plate (d - arrowhead), which never fully repairs over time. All SBC expanded over time, and appeared to transition from a vacuous, fluid filled cavity (b - arrow) to a more fibrous filled region containing immature or disorganized osteoid (c, f - arrows). Scale bar = 2 mm.

2.3.2 Quantitative and Histological Analysis

Volumetric BMD was calculated within the superficial subchondral bone with cylindrical ROIs that had a total volume of approximately 0.070 mm^3 . The vBMD immediately above the SBC decreased slightly from 4 to 8 weeks post-ACLX, but rose significantly higher at the final time point ($p = 0.01$), which indicated an active remodeling process in the peri-cystic subchondral bone. The OARSI score for the ACLX knees was

significantly higher ($p = 0.008$) than the contralateral knee of the same animal (Table 2-1).

Table 2-1: Descriptive statistics for all ACLX knees containing SBC (n=8). Values are mean \pm SE from SBC diameter and superficial vBMD occurring over time (* $p < 0.05$, versus 8 weeks). OARSI grade, acquired from the histological analysis, is provided for the final time point only and presented versus the contralateral limb score underneath.

Time post-ACLX	CT diameter (mm)	MRI diameter (mm)	vBMD (mg / cc)	OARSI grade
4 weeks	0.63 \pm 0.13	0.66 \pm 0.078	680 \pm 52	
8 weeks	0.92 \pm 0.11	0.83 \pm 0.11	630 \pm 30	
12 weeks	1.1 \pm 0.092	1.1 \pm 0.081	710 \pm 43*	18 \pm 0.82 2.9 \pm 0.58

In addition, the SBC were located at the site within the histological section that received the highest (i.e. most severe OA) grade, often accompanied by superficial or deep lesions, severe proteoglycan loss, and cyst formation within the cartilage itself. Although difficult to identify in every section, a connection or breach of the subchondral plate was confirmed for all SBC located near the joint space (Figure 2-4). However, these gaps were not an open communication with the joint space allowing fluid exchange, but rather filled with either a fibrous or cartilaginous reparative tissue. The bone surrounding the SBC appeared necrotic and lacked any blood vessels or normal marrow components when compared with the contralateral limb. Immunohistochemistry revealed that even at an advanced stage of OA – evidenced by the near complete loss of cartilage – the area surrounding the SBC was still undergoing bone remodeling, with increased markers for both osteoblasts (ALPL) and osteoclasts (Cathepsin K) (Figure 2-5).

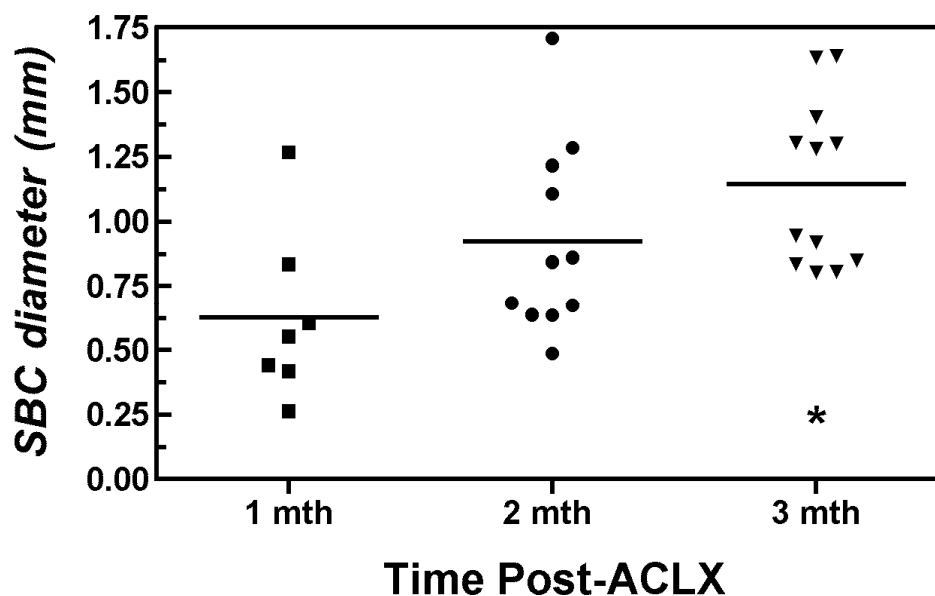


Figure 2-3: Mean maximal diameter of SBC in the medial tibial plateau for all rodents post-ACLX surgery. Shapes represent the SBC measured in the coronal plane using micro-CT at each time point. One-way ANOVA found the diameter increased significantly at 3 months post-ACLX versus the 1 month time point (* $p < 0.01$).

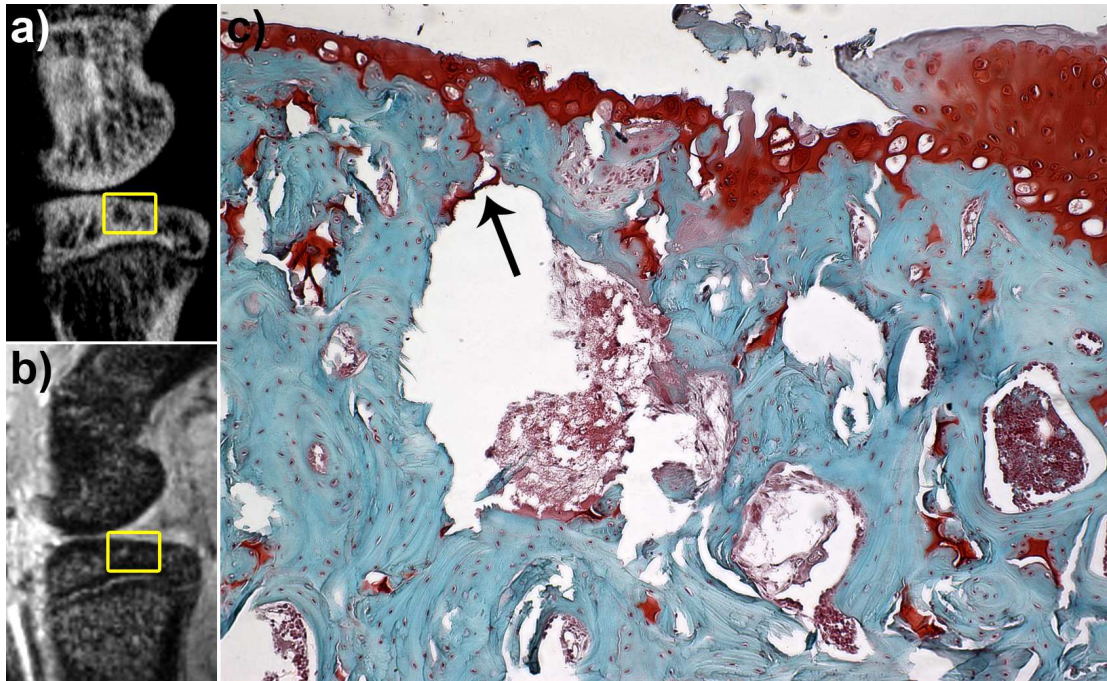


Figure 2-4: Identification of the subchondral plate breach found in SBC in the OA rat knee. Sagittal micro-CT (a) and high-field MRI (b) sections were used to observe and monitor SBC *in vivo*. End stage histological analysis confirmed separation in the subchondral bone (c - arrow, 10x magnification of Safranin-O with fast-green counter stain) that was filled with cartilaginous or fibrous tissue. Note the ‘pear’ shape of the intra-osseous lesion, consistent with SBC in humans.

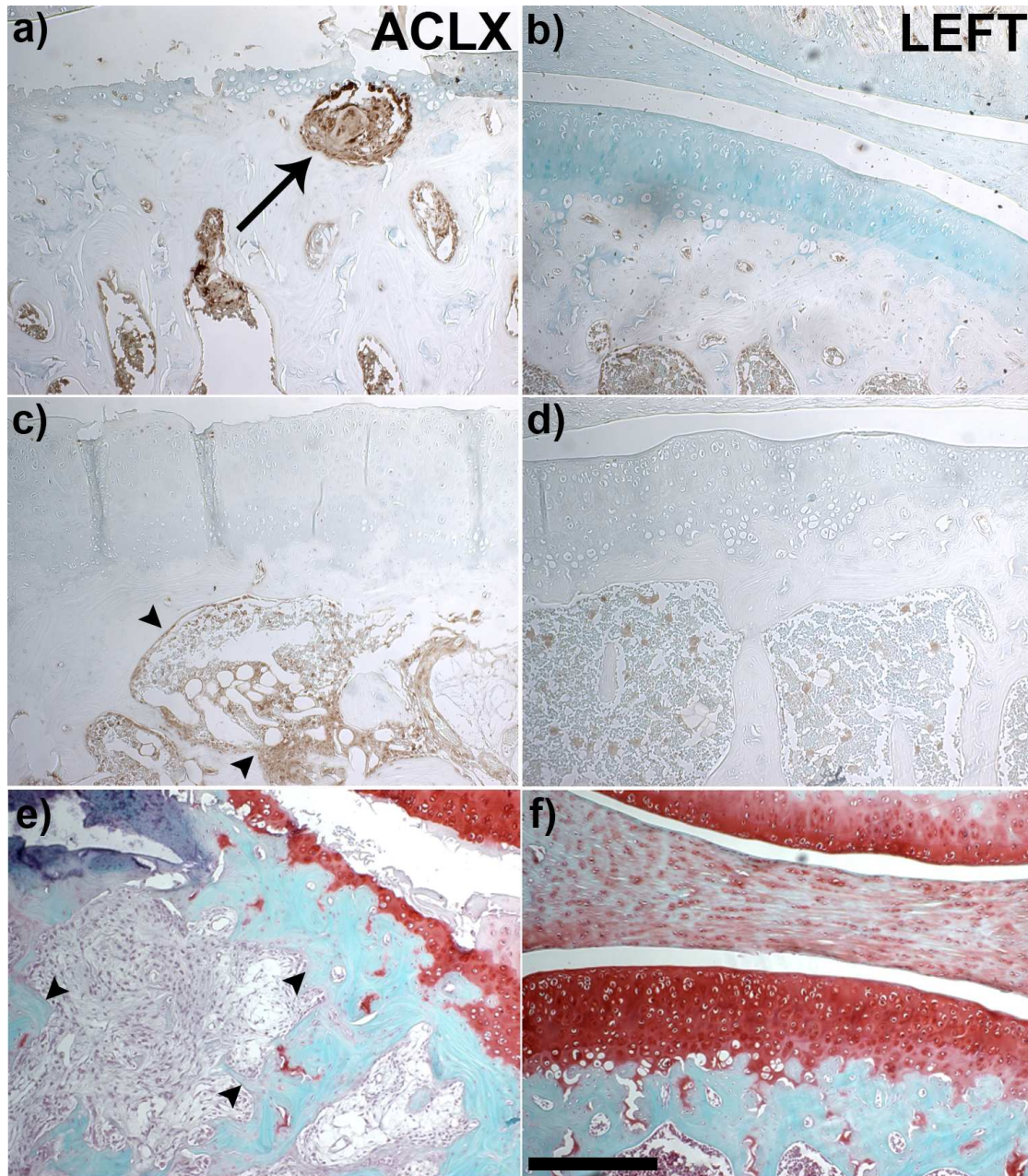


Figure 2-5: Histological characterization of SBC development in a rodent model of OA. Immunohistochemistry revealed an active bone remodeling response within the SBC, as the ACLX (a,c,e) knee showed greater staining for markers of both resorption (Cathepsin K, a-arrow), and bone formation (ALPL, c-arrowheads) against the unoperated knee of the same animal (LEFT, b,d,f). Safranin-O staining (e,f) showed the SBC (3 mth post-ACLX) as a fibrous cavity, surrounded by necrotic bone in the ACLX knee (e-arrowheads). Scale bar = 250 μ m

2.4 Discussion

To the best of our knowledge, this is the first study to identify and monitor SBC as they occur in a preclinical model of OA. The induction of OA through surgical destabilization in the rat knee produced SBC in a consistent manner within the medial tibial plateau, which could be measured with similar medical imaging techniques used in humans. High-field MRI aided in the depiction of SBC having both fluid and fibrous tissue components as they increased in size and number, and the rapid acquisition time enabled us to obtain an *in vivo*, dual-modality image of the rat knee in under an hour. Using histological analyses and a grading system of OA severity designed for humans [31], we found that SBC occur at the site of greatest disease severity, which agrees with previous findings in humans [21]. Thus, further validating the rat ACLX model of secondary OA with SBC development.

The presence of a breached subchondral plate was identified by Landells, and proposed to be the source of SBC formation [16]. As synovial fluid entered the cavity, it was thought to increase the intra-osseous pressure and lead to subsequent cyst expansion. However, this is unlikely as: the defect in the subchondral plate is small relative to the size of the SBC (Fig. 4c); the path from joint space to SBC is tortuous or oblique to the surface, limiting the ability of easy fluid exchange; the defect is filled with fibro-cartilage, which is less stiff than bone, but is unlikely to be as porous as healthy cartilage. In addition, as the SBC were still expanding by the final time point, there was evidence of immature bone deposition in some knees that would further inhibit fluid flow (Fig. 2-2f). Thus, Ondrouch proposed that due to a thinned cartilage layer, normal weight-bearing forces within the adjacent bone are increased beyond its physiological limits, causing focal damage, subsequent resorption, and SBC formation [15]. Recent mechanical simulations have confirmed the higher intra-osseous stress values beneath the joint surface when the amount of overlying cartilage is diminished [17], which could also lead to SBC formation in the opposing bone of the hip. Our results indicate that the SBC are developing and expanding due to the mechanical instability imposed by the ACLX. Increased shear stress on the surface of the cartilage, caused by the loss of the ACL, combined with a medial compartment-weight distribution bias, due to the menisectomy, caused cartilage

reduction or fibrillation and increased intra-osseous stress simultaneously. Therefore, the defect in the subchondral bone is likely a micro-fracture in response to the overloaded region in the joint. Repeated loading during gait prevents sufficient healing and the space remains occupied with fibrous tissue, while the bone below undergoes further damage leading to focal osteonecrosis [32, 33].

The expansion of these SBC in OA joints occurs due to stress-induced bone resorption of necrotic tissue. In the hip, this can continue until the majority of the epiphyseal trabecular bone in the femoral head or acetabulum is resorbed, causing great pain and deformity [14, 16, 17]. The SBC in knee OA tend to be smaller and contain an outer rim of sclerotic bone that makes them distinguishable even when imaged with planar radiographs [13, 34]. This may indicate a form of self-limitation within the bone, where the SBC become more spherical and are surrounded by a necrotic shell to help dissipate the increased loading. Thus explaining how some SBC can resolve or reduce in size over time [21] if the fibro-cartilage tissue within the cavity is provided the opportunity to mineralize. Sclerotic bone formation is emulated in our rat model as vBMD significantly increased (at 12 weeks post-ACLX) on the superficial surface of the SBC after recovering from the initial resorptive phase (4 to 8 weeks). Furthermore, simulations of SBC within the human knee using finite element analysis indicated intra-osseous stress concentrations were higher near the joint surface [28], which could explain the sclerotic bone formation seen in the proximal tibia (Fig. 2-2f).

One of the features lacking in our SBC models was the detectable presence of bone marrow edema, which is commonly associated with human SBC development [18-20]. A diffuse, and high-intensity fluid-like signal upon MRI examination of the trabecular bone is the proposed evidence of edema in the joint compartment, typically as a result of injury and the subsequent initiation of the bone remodeling process [20]. Edema has been found to precede SBC formation in most cases [20, 21], but its presence does not guarantee trabecular remodeling when compared with histological examination [35]. The inability to detect bone edema may have been caused by MRI sequence used, as it did not incorporate fat suppression techniques that enhance edema visualization against the fatty bone marrow [36]. However, we were concerned about masking any marrow

components that may be included within the SBC and chose not to use fat suppression in our MRI protocol. With the development of custom designed rat knee coils [37] – that incorporate longer scan times for increased signal-to-noise ratio – it will be feasible to further quantify the tissue composition of SBC over time, without reliance on destructive histological analysis. Recent work using the rat model of secondary OA combined with dual-modality has further demonstrated the utility of longitudinal imaging by evaluating the effect of anti-inflammatory drugs on disease progression [23]

In summary, the rat ACLX model of post-traumatic knee OA provides valuable insights into the cause and composition of a degenerative feature within the subchondral bone that is associated with greater pain and disease severity. Subchondral cysts, as they are commonly referred to, appeared in a predictable manner within the overloaded joint compartment of the medial tibial plateau. These SBC do not contain any evidence of an epithelial lining and therefore can be referred to as ‘pseudo-cysts’ or geodes, which considers the formation of a lesion in response to stress [13, 14]. Our evidence suggests that these spherical or pyriformal intra-osseous lesions contain fibrous tissue – which may initially contain fluid, and can ossify in later stages – surrounded by regions of osteonecrosis that eventually forms a sclerotic margin in response to repeated, pathological loads. Although, there is a breach of the subchondral bone plate, the expansion of these SBC is more likely due to micro-fracture and stress-induced bone resorption. Therefore, future investigations should refer to SBC as focal, ischemic OA-induced osteonecrotic (FION) lesions to reflect their unique pathogenesis. It remains unclear whether FION lesions first initiate due to a loss of cartilage integrity or as a result of a subchondral bone failure, but this debate is common in OA research and future studies should strive to characterize the response of both tissues to pathological stress conditions. In addition, it should be noted that FION lesions tended to appear in combination with greater cartilage severity scores. Finally, *in vivo* dual-modality imaging is an invaluable method for quantifying the efficacy of therapeutic interventions developed to treat FION lesions in humans [38] or animals [23].

2.5 References

1. Bieleman, H.J., et al., *Work participation and health status in early osteoarthritis of the hip and/or knee: a comparison between the Cohort Hip and Cohort Knee and the Osteoarthritis Initiative*. *Arthritis Care Res (Hoboken)*, 2010. **62**(5): p. 683-9.
2. Kopec, J.A., et al., *Development of a population-based microsimulation model of osteoarthritis in Canada*. *Osteoarthritis Cartilage*, 2010. **18**(3): p. 303-11.
3. Perruccio, A.V., J.D. Power, and E.M. Badley, *Revisiting arthritis prevalence projections--it's more than just the aging of the population*. *J Rheumatol*, 2006. **33**(9): p. 1856-62.
4. Poole, R., et al., *Recommendations for the use of preclinical models in the study and treatment of osteoarthritis*. *Osteoarthritis Cartilage*, 2010. **18 Suppl 3**: p. S10-6.
5. Poole, A.R., *An introduction to the pathophysiology of osteoarthritis*. *Front Biosci*, 1999. **4**: p. D662-70.
6. Mankin, H.J., *The reaction of articular cartilage to injury and osteoarthritis (first of two parts)*. *New England Journal of Medicine*, 1974. **291**(24): p. 1285-92.
7. Findlay, D.M., *Vascular pathology and osteoarthritis*. *Rheumatology (Oxford)*, 2007. **46**(12): p. 1763-8.
8. Burr, D.B., *The importance of subchondral bone in the progression of osteoarthritis*. *J Rheumatol Suppl*, 2004. **70**: p. 77-80.
9. Buckland-Wright, C., *Subchondral bone changes in hand and knee osteoarthritis detected by radiography*. *Osteoarthritis Cartilage*, 2004. **12 Suppl A**: p. S10-S19.
10. Buckwalter, J.A., *Articular cartilage injuries*. *Clin Orthop Relat Res*, 2002(402): p. 21-37.

11. Shirazi, R. and A. Shirazi-Adl, *Computational biomechanics of articular cartilage of human knee joint: effect of osteochondral defects*. J Biomech, 2009. **42**(15): p. 2458-65.
12. Altman, R.D., *Early management of osteoarthritis*. Am J Manag Care, 2010. **16 Suppl Management**: p. S41-7.
13. Bancroft, L.W., J.J. Peterson, and M.J. Kransdorf, *Cysts, geodes, and erosions*. Radiol Clin North Am, 2004. **42**(1): p. 73-87.
14. Resnick, D., G. Niwayama, and R.D. Coutts, *Subchondral cysts (geodes) in arthritic disorders: pathologic and radiographic appearance of the hip joint*. AJR Am J Roentgenol, 1977. **128**(5): p. 799-806.
15. Ondrouch, A.S., *Cyst formation in osteoarthritis*. J Bone Joint Surg Br, 1963. **45**: p. 755-60.
16. Landells, J.W., *The bone cysts of osteoarthritis*. J Bone Joint Surg Br, 1953. **35-B**(4): p. 643-9.
17. Durr, H.D., et al., *The cause of subchondral bone cysts in osteoarthrosis: a finite element analysis*. Acta Orthop Scand, 2004. **75**(5): p. 554-8.
18. Kornaat, P.R., et al., *Osteoarthritis of the knee: association between clinical features and MR imaging findings*. Radiology, 2006. **239**(3): p. 811-7.
19. Marra, M.D., et al., *MRI features of cystic lesions around the knee*. Knee, 2008. **15**(6): p. 423-38.
20. Roemer, F.W., et al., *Subchondral bone marrow lesions are highly associated with, and predict subchondral bone attrition longitudinally: the MOST study*. Osteoarthritis and Cartilage, 2010. **18**(1): p. 47-53.

21. Tanamas, S.K., et al., *The association between subchondral bone cysts and tibial cartilage volume and risk of joint replacement in people with knee osteoarthritis: a longitudinal study*. *Arthritis Res Ther*, 2010. **12**(2): p. R58.
22. McErlain, D.D., et al., *Study of subchondral bone adaptations in a rodent surgical model of OA using in vivo micro-computed tomography*. *Osteoarthritis Cartilage*, 2008. **16**(4): p. 458-69.
23. Jones, M.D., et al., *In vivo microfocal computed tomography and micro-magnetic resonance imaging evaluation of antiresorptive and antiinflammatory drugs as preventive treatments of osteoarthritis in the rat*. *Arthritis Rheum*, 2010. **62**(9): p. 2726-35.
24. Schambach, S.J., et al., *Application of micro-CT in small animal imaging*. *Methods*, 2010. **50**(1): p. 2-13.
25. Batiste, D.L., et al., *High-resolution MRI and micro-CT in an ex vivo rabbit anterior cruciate ligament transection model of osteoarthritis*. *Osteoarthritis Cartilage*, 2004. **12**(8): p. 614-26.
26. Faure, P., B.T. Doan, and J.C. Beloeil, *In-vivo high resolution three-dimensional MRI studies of rat joints at 7 T*. *NMR Biomed*, 2003. **16**(8): p. 484-93.
27. Appleton, C.T., et al., *Forced mobilization accelerates pathogenesis: characterization of a preclinical surgical model of osteoarthritis*. *Arthritis Res Ther*, 2007. **9**(1): p. R13.
28. McErlain, D.D., et al., *Subchondral cysts create increased intra-osseous stress in early knee OA: A finite element analysis using simulated lesions*. *Bone*, 2011. **48**(3): p. 639-46.
29. Howie, D.W., et al., *Progression of acetabular periprosthetic osteolytic lesions measured with computed tomography*. *J Bone Joint Surg Am*, 2007. **89**(8): p. 1818-25.

30. Ulici, V., et al., *Regulation of gene expression by PI3K in mouse growth plate chondrocytes*. PLoS One, 2010. **5**(1): p. e8866.
31. Pritzker, K.P., et al., *Osteoarthritis cartilage histopathology: grading and staging*. Osteoarthritis Cartilage, 2006. **14**(1): p. 13-29.
32. Saini, A. and A. Saifuddin, *MRI of osteonecrosis*. Clin Radiol, 2004. **59**(12): p. 1079-93.
33. Theodorou, S.J., et al., *Osteonecrosis of the tibial plateau: magnetic resonance imaging appearances with quantitation of lesion size and evidence of a pathogenesis of meniscal injury*. J Comput Assist Tomogr, 2010. **34**(1): p. 149-55.
34. Bianchi, S., et al., *Expansile subchondral degenerative bone cyst secondary to osteoarthritis*. Can Assoc Radiol J, 1995. **46**(4): p. 308-10.
35. Zanetti, M., et al., *Bone marrow edema pattern in osteoarthritic knees: correlation between MR imaging and histologic findings*. Radiology, 2000. **215**(3): p. 835-40.
36. Crema, M.D., et al., *Contrast-enhanced MRI of subchondral cysts in patients with or at risk for knee osteoarthritis: The MOST study*. Eur J Radiol, 2009.
37. Goebel, J.C., et al., *New trends in MRI of cartilage: Advances and limitations in small animal studies*. Biomed Mater Eng, 2010. **20**(3): p. 189-94.
38. Menetrey, J., et al., *Epidemiology and imaging of the subchondral bone in articular cartilage repair*. Knee Surg Sports Traumatol Arthrosc, 2010. **18**(4): p. 463-71.

Chapter 3

3 Subchondral Cysts create increased Intra-osseous stress in Early Knee OA: a Finite Element Analysis using Simulated Lesions

A version of this chapter appeared in *Bone* 48 (3): 639–646 (2011) as “Subchondral cysts create increased intra-osseous stress in early knee OA: A finite element analysis using simulated lesions.” by D.D. McErlain, J.S. Milner, T.G. Ivanov, L. Jencikova-Celerin, S.I. Pollmann, D.W. Holdsworth.

3.1 Introduction

Osteoarthritis (OA) is a degenerative disease that causes a progressive loss of cartilage and bone integrity [1], with permanent changes to the mechanical function of joints [2]. While affecting an increasing number of people – due to increases in both the average age and obesity rate in North America [3, 4] – there is incomplete understanding into the mechanisms under which OA or other joint pathologies are initiated, leading to pain and disability [5]. Moreover, current pharmacological treatments of OA have inconsistent benefits on a patient-by-patient basis in treating symptoms while simultaneously modifying disease progression [6, 7]. Progression of OA is related to subtle changes in the ability of an individual’s subchondral bone to respond to an increased or displaced load bearing pattern, a mechanism which has not been adequately addressed [1, 8]. The ability to monitor the patient-specific biomechanical properties of subchondral bone and soft tissue throughout the initiation, progression, and treatment of OA would serve as an invaluable resource in determining the efficacy of emerging surgical or pharmacological interventions.

The presence of a subchondral bone cyst (SBC) in the weight-bearing regions of joints is a characteristic bone adaptation that has been associated with OA [9-11]. SBCs are normally spherical or ellipsoidal in shape and have been predominantly reported in the hip and knee [12, 13], typically lying adjacent to the joint surface where initial load

bearing occurs during activity. Recently, the presence of SBC has even been reported in a preclinical, longitudinal model of OA [14]. The structure of a SBC has been derived and distinguished from other joint pathologies (i.e. bone edema) using advanced medical imaging techniques, such as Magnetic Resonance Imaging (MRI) [10, 15-17]. Unfortunately, planar radiography remains the clinical standard for OA diagnosis, even though intra-osseous abnormalities can be easily distinguished with 3D imaging techniques, such as Computed Tomography (CT), with CT adding the potential for highly accurate and precise, quantitative and functional measurements of joint function.

Recent advances in finite element (FE) analysis have been useful in applying bone-specific material properties to discrete volumes of bone in 3D using CT images [18, 19]. In addition, previous work in 2D has shown the effect of SBC on stress distribution within bone adjacent to an artificial hip lesion [20, 21]. Currently, the use of subject-specific bone images to create 3D FE models – with material properties derived directly from the CT image – is available with commercial software, operating on desktop hardware [18, 22]. Using this approach, it is possible to introduce synthetic defects into patient images (such as spherical voids mimicking a SBC), for use in FE models to assess the effect of SBCs on the biomechanical properties of the joint under physiological loading.

Our objective is to use patient-specific FE models of the knee to characterize the effect of SBC on the relative mechanical properties of the joint. In this study, we determine whether the presence of a virtual SBC within the OA knee leads to significant changes in the values for intra-osseous stress under physiological loading. To date, no analysis has been conducted on the effect of SBC within the weight-bearing regions of human knee joints utilizing mechanical properties derived directly from *in vivo* image data. The results of this study provide further insight into both the cause of cyst initiation, and its subsequent expansion; the exact mechanism of which remains elusive.

3.2 Methods

3.2.1 Early OA patient data

As part of a previous study [23], 50 early knee OA patients (Kellgren-Lawrence score ≤ 2) [24] were scanned in our laboratory with a prototype cone-beam 3D CT system (Multistar, Siemens Medical Solutions, Erlangen, Germany) prior to undergoing arthroscopic surgery. Twenty knee CT volumes from this patient population ($N = 20$) were randomly selected for use in our study. Informed consent was obtained in accordance with the approval from the ethical review board at the University of Western Ontario prior to any imaging experiments and all data was further anonymized before SBC and FE model creation.

All patients had their affected knee affixed with a tissue calibrator prior to 3D CT imaging. This calibration device mimicked the radiographic properties of tissues, including those of cortical bone (SB3, Gamex RMI, Middleton, US), in order to ensure that the reconstructed data set was properly scaled to Hounsfield units (HU) [25] and calibrated in volumetric bone mineral density ($\text{mg}\cdot\text{cm}^{-3}$ of hydroxyapatite). Once in place, the knee was immobilized with a radiolucent plastic splint and the patient was positioned on the scanner bed. The CT acquisition protocol consisted of a series of 135 x-ray projections taken at 1.5° increments over 4.4 seconds, with typical exposure parameters of 90 kVp and 40 mA·s. The final reconstructed 3D data set had an isotropic voxel spacing of 0.55 mm.

3.2.2 SBC design and implementation

Having anonymized the 3D CT patient data, one observer determined a location within each image volume at which the synthetic SBC would be introduced. The observer viewed the images of the knee in multi-planar reformatted view (MPR) using MicroView software (v.2.1.2, General Electric Health Care, London, Canada), which allowed for navigation in all three anatomical planes simultaneously. The location of the SBC was assigned at random with the following constraints: 1) the SBC was located in the weight-

bearing regions of either the tibia or the femur; and 2) did not breach the subchondral bone plate, thereby causing an open communication with the joint space. Therefore, the synthetic SBCs were all placed adjacent to, or within the subchondral bone plate, provided there was at least 1 mm of surrounding bone at all points. The diameter of the SBC was set within a range of values (3 - 12 mm) reflecting the dimensions of actual SBC reported in recent literature [10, 15, 20]. The user subsequently specified the 3D coordinates (in voxels) of the centre of the SBC and created a temporary synthetic, spherical void within the patient's CT volume at that location, using custom software, which ensured its parameters adhered to the previous constraints. The intensity values within the synthetic lesions were set to 0 HU for visual verification of the SBC location, and the coordinates and diameters were recorded for the subsequent creation of the SBCs within the FE models.

3.2.3 Patient-Specific FE Models

3.2.3.1 FE Model creation

A flow chart summarizing the creation of patient-specific FE models is shown in Figure 3-1. The surface geometries of all bones within the knee joint (i.e. patella, femur, tibia, and fibula) were extracted from the 3D CT volume via isosurfacing and image-based thresholding, as implemented in MicroView. The ensuing triangulated surface data was exported in stereolithography (STL) format for post-processing in Geomagic Studio (v.10, Geomagic, North Carolina, USA) to ensure that the imported structure was topologically valid with no holes, rough edges, or non-physiological defects. The soft tissue surrounding the joint was semi-automatically segmented as a series of user-defined spline curves using MicroView, which were interpolated and lofted into a full 3D structure and post-processed as described above.

The resultant surface mesh geometries were subsequently imported into a commercial FE software package (Abaqus CAE v.6.8.3, Simulia, Rhode Island, USA) for model assembly and loading simulations. The FE model, which combined all of the bones and the tissue surface geometries, was limited to 160 mm extent in the Z-direction (i.e. along the long axis of the femur).

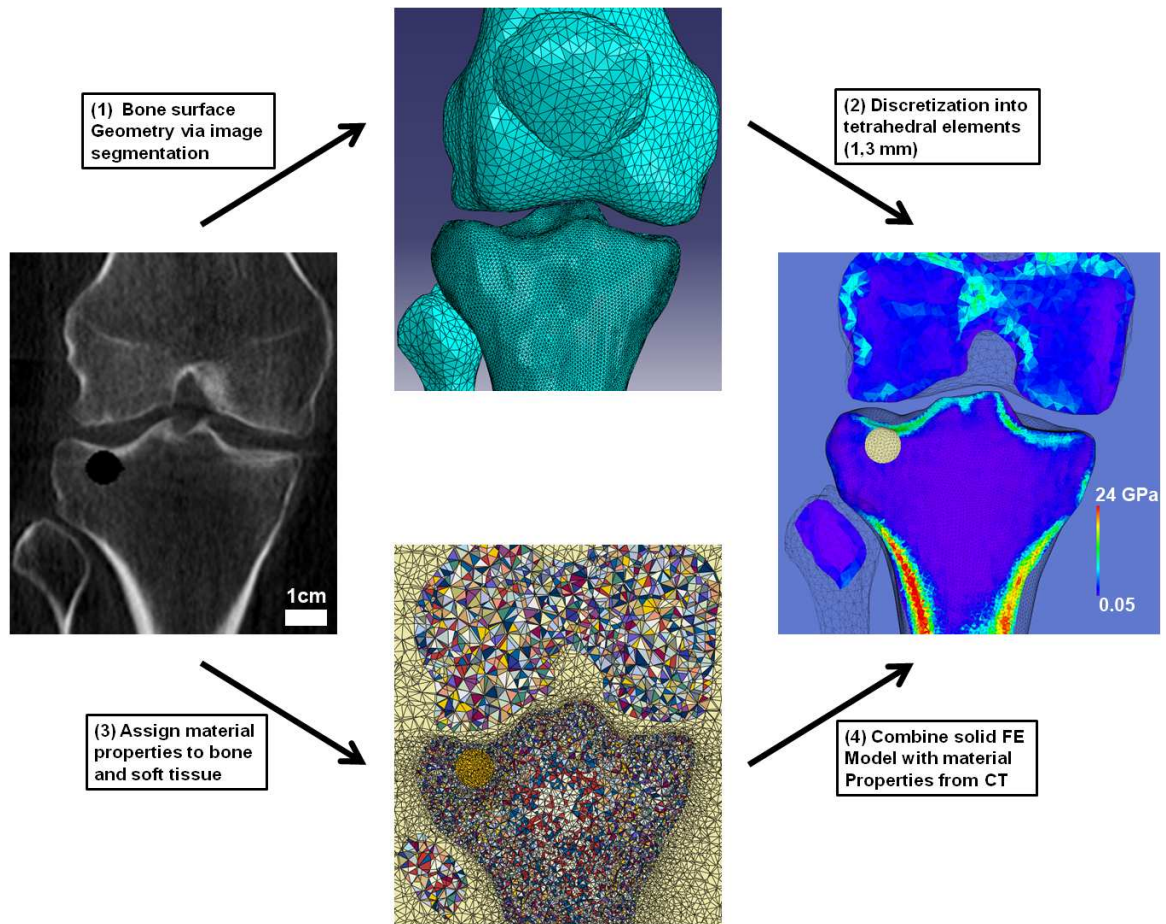


Figure 3-1: Flow chart describing the assignment of material properties, and creation of patient-specific FE models using *in vivo* CT images of the human knee. Note the defined area of the synthetic SBC, which is defined to have a uniform material property, $E = 1e-6$ (bottom; orange region). For enhanced visualization of the heterogeneous material properties assigned in step 3, a discontinuous look-up table has been selected; neighboring elements typically exhibited similar mechanical properties (step 4).

The operator subsequently defined the synthetic SBC within the second, duplicate copy of each model at the prescribed 3D location derived from the CT image (section 3.2.2 above), which was implemented as a sphere of elements with equivalent diameter as prescribed in the image data. Afterwards, a separate sphere (concentric with the SBC) was created, with a diameter exactly 1 mm wider than the prescribed SBCs. Through a Boolean difference operation, this larger sphere created a spherical shell of elements that defined a 1 mm region surrounding the SBC; this shell defined the region of interest

(ROI) where the measurements for peri-cystic, maximum von Mises stress under loading were isolated and collected. Thus, for each patient there were two FE knee models; the first had the shell ROI within the bone around the supposed SBC site (without altering the material properties within the site), while the second contained the ROI surrounding a sphere of elements that had modified material properties assigned to mimic a SBC (see section 3.2.3.2 below). Time to completion from patient image to joint specific FE model was approximately 2 hours.

Linear, 4-node tetrahedral elements were chosen for all tissues modeled [26], which ensured high bone material resolution within the elements of the FE models, while maintaining reasonable simulation times [27] and allowed for the high throughput of a relatively large sample size ($N = 40$). Element edge lengths were 1 mm in the bone that contained the SBC and 3 mm in the remaining bones and soft tissue. An initial loading run, with only 2 material properties assigned (i.e. bone and tissue), was undertaken to test the model with a specified load direction, boundary conditions, and obtain the final set of FE. The mesh was subsequently processed as described below in order to design image-based, inhomogeneous, patient-specific bone densities and elastic moduli for each element.

3.2.3.2 Image-based Assignment of Material Properties

We assigned material properties within our FE models using a CT derived, bone density to modulus conversion that has been described previously [18]. Briefly, the patient-specific material properties assigned to the finite elements of the bones were calculated from the 3D-CT data (Fig. 3-1 - step 3) using a bone mineral density (BMD) to elastic modulus relationship, developed by Morgan et al. [28]. The non-linear, BMD-modulus relationship was developed experimentally, in a manner that minimized experimental artifacts [29], using human trabecular bone samples from various anatomical sites. Ash density (as determined from the calibration sample in each CT image) was converted to apparent density using a ratio of 0.55 between ash and apparent density [29]. Thus, the FE model for each knee had a heterogeneous 3D mapping of computed elemental elastic moduli (Fig. 3-1 – step 5) for all bones prior to loading simulations. The exact range and resolution of the bony elastic moduli was determined from a pilot study, which examined

the elastic modulus resolution required to adequately resolve strain energy density to within 1% RMSE in the elements of the SBC shell ROI in comparison to an over-resolved material model containing modulus increments of 10 MPa. This initial study showed that a material resolution of 50 MPa was sufficient to meet the convergence criteria. Therefore, the bones were modeled using 640 incremental materials that consisted of moduli from ranging 50 to 32000 MPa. A uniform Poisson ratio of 0.3 was assigned for all bone elements [30]. The surrounding soft tissue was modeled using the compressive properties of cartilage under compression at equilibrium, which may be represented as an isotropic, linearly elastic solid [31, 32]. As the 3D-CT has limited soft tissue contrast with respect to cartilage surface delineation – and in order to reduce the model complexity and solution times – all elements outside the bony margins were assigned the material properties of cartilage. Young's modulus and Poisson's ratio for soft tissue was assigned values of 0.7 MPa and 0.1, respectively, which fell within the previously described ranges for the intrinsic, equilibrium properties of articular cartilage in compression [33].

The material properties assigned to the synthetic SBC were determined by a pilot study that simulated loading in the joint with varying elastic moduli assigned to the sphere of elements within the weight-bearing bone. No significant differences in values for stress were detected in the elements contained within the shell ROI surrounding the SBC for elastic moduli ranging from $1e-6$ to 30 MPa. Consequently, each patient's duplicate FE model had a simulated SBC placed within the knee with a negligible elastic modulus (Young's modulus of $1e-6$ MPa).

3.2.3.3 Loading Simulation

The loading simulations were all performed on a commercially available desktop workstation (Intel Core 2 Duo, 2.66 GHz processor; 8 GB RAM; NVIDIA 8600GT, 256 MB graphics card) within our laboratory. Loading was developed to approximate the physiologic conditions in a single-leg standing position. A 750 N load was applied for all cases, which is representative of a 75 kg individual standing on one leg. Time-dependent cartilage response was removed from the analysis by obtaining a steady-state solution

under equilibrium conditions. Short-term, high strain-rate, impulse loading was therefore not considered.

The study was designed such that the bone with the SBC was fixed while being acted upon by the non-SBC bone during the loading simulation. At one end of the model, the nodes on the axial surface area of the cortical shell of the loading bone were manually selected and constrained to allow displacements in the vertical direction only, in order to prevent unrestrained rotation of the knee joint in lieu of supporting musculature and ligaments. In addition, the nodes on the axial surface area of the SBC-containing bone at the other end of the model were constrained for all degrees of freedom to prevent rotation and displacement. Identical boundary conditions were used for the matched, non-SBC FE model of each patient's knee for reliable comparison between the response of SBC and non-SBC containing models under loading.

3.2.4 Data Analysis

The resultant values for von Mises stress (MPa) within the peri-cystic shell ROI surrounding the SBC were compared between cyst and non-cyst models using a paired T-test, with an alpha level for $p < 0.05$ considered significant. Note that the *in vivo*, patient-specific models in this study ($N = 40$) were derived from CT data only, which provided complete material property information solely for the bones without a comprehensive inclusion of all soft tissue structures involved in single leg weight-bearing. For this reason, we consider these stress values to be accurate for relative comparisons, and not necessarily indicative of absolute intra-osseous stress. A two-way ANOVA was conducted to assess the effect of the location of the SBC on intra-osseous stress. The FE models were grouped ($n = 5$ per group) by the bone (tibia versus femur) and compartment (medial versus lateral) in which the cyst was located (Table 3-1). In addition, a linear regression analysis was performed to assess the effect of SBC diameter on intra-osseous stress using the SBC model data only ($N = 20$).

Table 3-1: Design and implementation of OA patient-specific FE models. Note, the von Mises stress (MPa) is reported from the 1 mm thick sample volume (i.e. shell region) in both models. Patients 1-10 and 11-20 have a SBC located in the tibia and femur, respectively. Simulation Time is in minutes.

Patient	Cyst diameter (mm)	Region	FEs in Model	FEs in Cyst 'Shell'	Simulation Time; No SBC vs SBC	Max Stress (MPa) - No SBC	Max Stress (MPa) - SBC
1	5.50	Medial	1179018	1923	54.4/53.3	1.263	1.898
2	9.89	Lateral	1087738	3614	59.7/60.0	1.023	1.519
3	12.0	Medial	1120663	4245	61.8/57.8	0.943	2.069
4	4.40	Medial	890438	1249	29.7/41.1	1.387	2.504
5	6.60	Medial	1192686	2327	66.3/52.5	1.042	1.659
6	3.30	Medial	1136461	505	70.3/61.8	0.888	1.121
7	6.60	Lateral	1091294	2262	58.5/56.1	0.934	1.565
8	9.34	Lateral	991652	3415	47.1/45.0	1.729	2.588
9	4.95	Lateral	1027364	1112	50.3/45.9	1.307	2.273
10	11.54	Lateral	1062664	4148	62.0/56.7	1.040	3.067
11	3.30	Medial	1354162	626	66.6/70.6	0.716	0.992
12	6.60	Medial	1092087	2219	46.7/47.9	0.993	2.110
13	4.95	Medial	1619674	1225	113.8/103.0	0.525	0.909
14	9.89	Medial	1466116	3441	86.1/84.9	0.832	1.546
15	12.09	Medial	1197240	4252	54.1/54.1	1.106	2.923
16	4.40	Lateral	1204968	1026	55.3/55.8	0.611	1.271
17	4.40	Lateral	1538725	1050	92.3/94.7	0.678	0.757
18	3.30	Lateral	1608690	484	101.8/104.0	0.511	0.801
19	7.70	Lateral	1441348	2799	80.5/80.9	0.479	1.024
20	7.15	Lateral	1594090	2227	94.7/96.5	0.668	1.177

3.3 Results

3.3.1 Patient-Specific Model Creation

The numerical results of the patient-specific model creation and loading simulations are summarized in Table 3-1. All pairs of FE models made from the *in vivo* CT data set of each OA patient was successfully created using a mean of approximately 1.2 million elements. The mapping of heterogeneous material properties to the bone, and the homogeneous material properties assigned to the soft tissue and SBC – in half of the models – was achieved in a relatively short period of time (Figure 1 - step 5, approximately 2 hours per pair of models), which allowed for a large sample size used in the loading simulations (N = 40). The mean (\pm standard deviation) overall BMD for the early OA knees, calculated within the weight-bearing regions of the tibia and femur, was 278.1 ± 38.3 mg/cc. All loading simulations were completed successfully with a mean time of 67 ± 21 and 66 ± 20 min. for the non-SBC and SBC models, respectively (Table 3-1). Each pair of patient-specific model simulations were completed in sequence, which allowed for seamless comparison of both measured stress and the effect of SBC on weight-bearing bone (Figure 3-2).

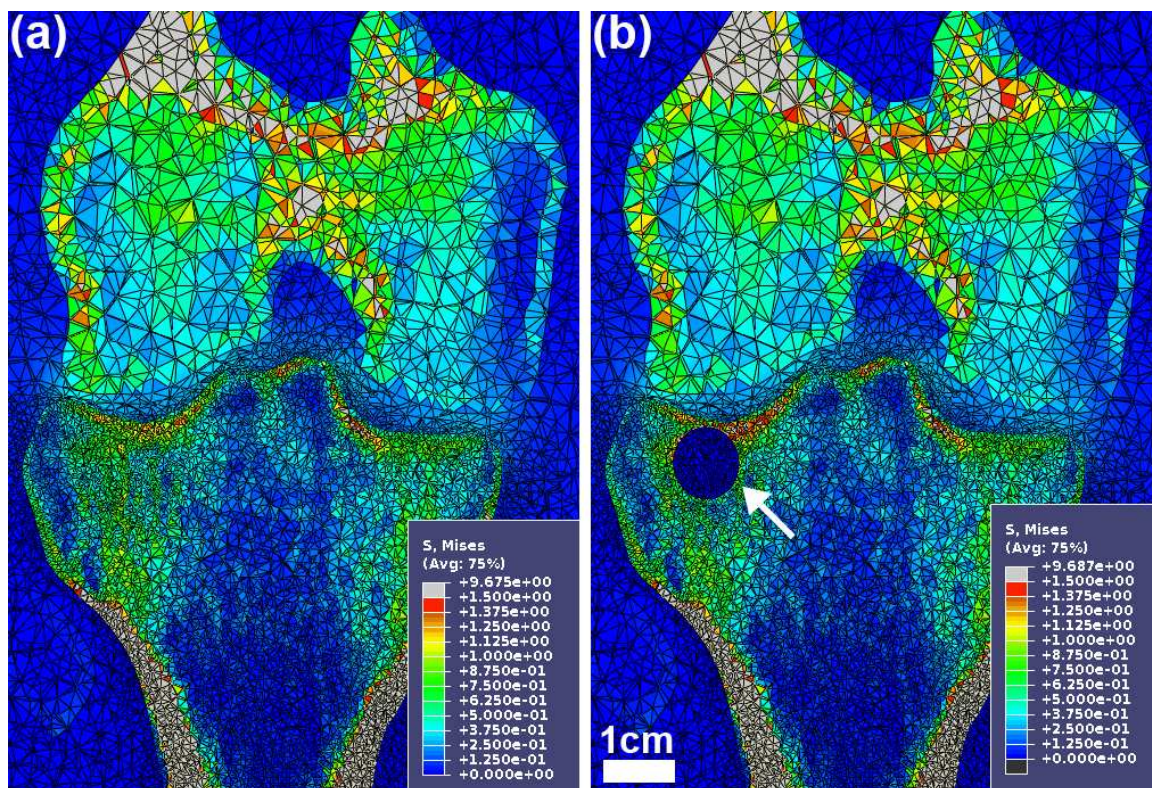


Figure 3-2: Comparing the effect of SBC on the weight-bearing properties of the knee, using the same early stage OA knee with (right) and without (left) a synthetic SBC placed in the tibia (b - arrow). Each FE model underwent a 750 N load that simulated a single-leg stance position.

3.3.2 Effect of SBC on Weight-bearing

The resultant values for intra-osseous, peri-cystic stress – obtained from the FE loading simulation of single-leg weight-bearing – in the patient models that contained a synthetic SBC were significantly higher than those reported in the matched, non-SBC FE models (Figure 3-3; paired T-test, $p < 0.0001$). The mean (\pm standard error) values for maximum stress were 0.934 ± 0.073 MPa and 1.69 ± 0.159 MPa for the non-SBC and SBC models, respectively. Qualitative observations of the shell ROI under load, as seen in Figure 3-4, revealed a trend where the maximum stress values often appeared in the region of bone closest to the joint space, which generally contained bone with higher elastic modulus; as determined by the tendency for elevated *in vivo* BMD in subchondral regions (Fig. 3-1 - step 4). This trend was especially evident upon evaluation of SBC versus non-SBC FE

models, wherein the ROI of elements surrounding the SBC displayed maximum stress values significantly greater than the ROI surrounding the non-SBC, for the shared patient model under a 750 N load (Fig. 3-4, a,c versus b,d). Moreover, the result of the linear regression analysis confirmed that an increase in SBC diameter was positively correlated with an increase in intra-osseous stress ($r^2 = 0.372$).

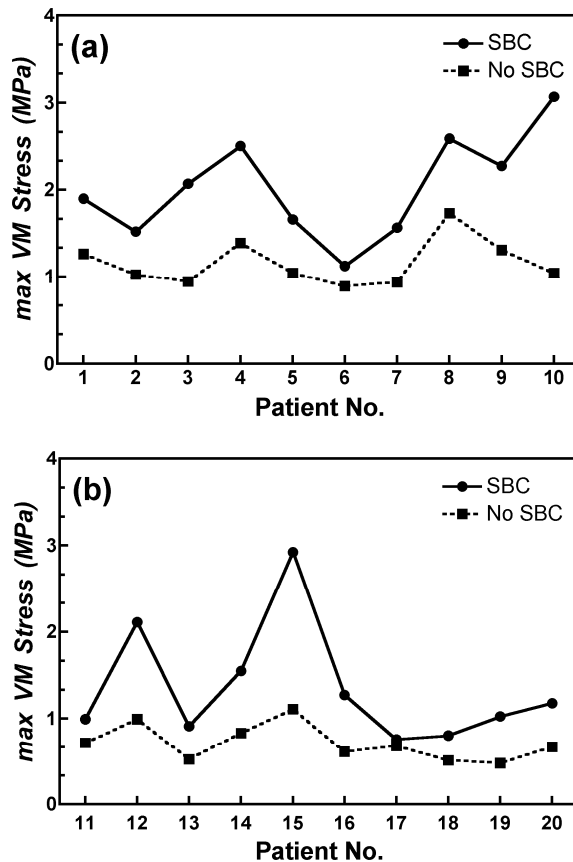


Figure 3-3: Maximum von Mises stress (MPa) in knee OA patients without SBC versus with SBC (dotted line vs. solid line) within the tibia (a) and femur (b). Paired t-test for all patients showed significant difference between groups ($p < 0.0001$).

The slope of the regression line was significantly non-zero ($p = 0.0043$) and is plotted with the 95% confidence intervals in Figure 3-5. No significant differences were detected by the two-way ANOVA ($p > 0.05$) that compared the change in intra-osseous stress within the medial versus lateral compartment and between the femur and tibia (Figure 3-6).

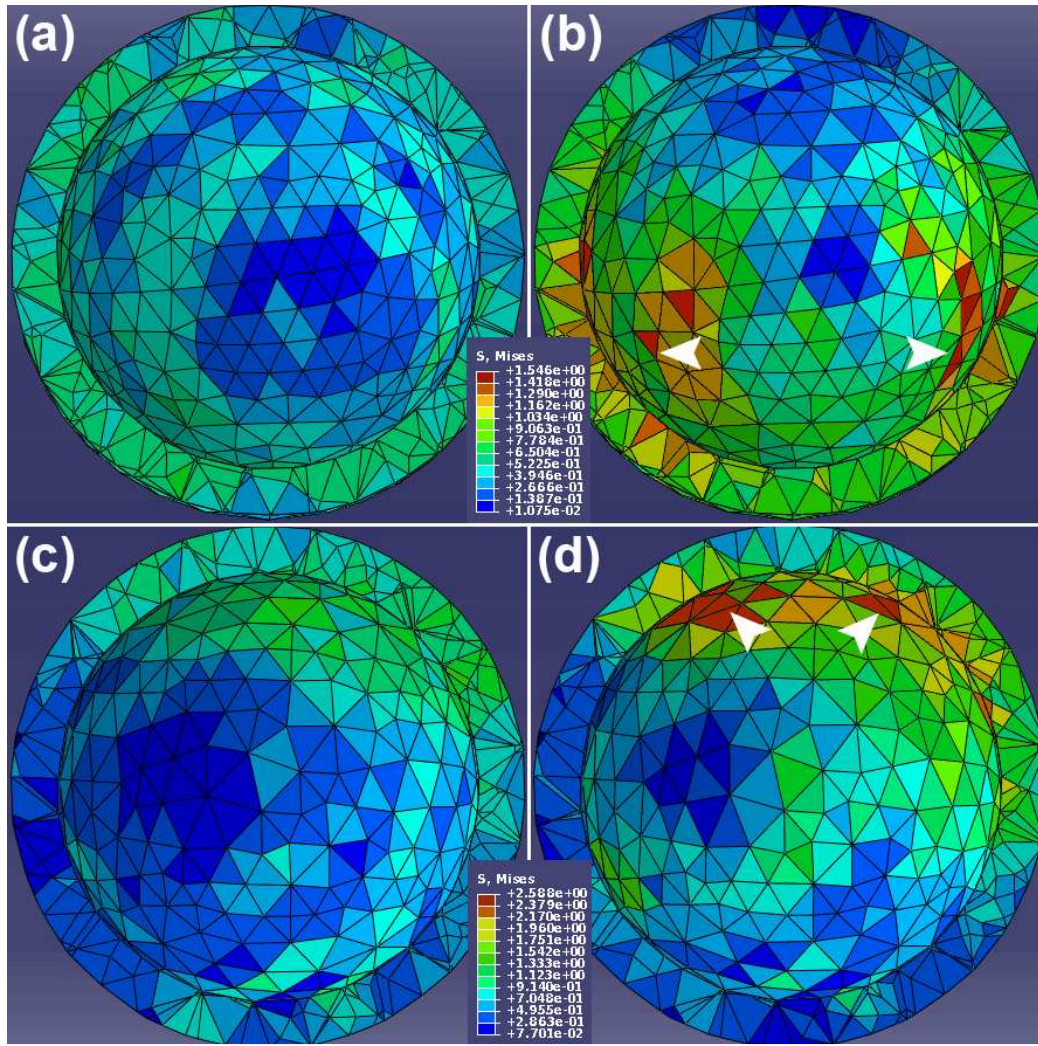


Figure 3-4: Enhanced view of elements in the sample volume (i.e. annular shell region of interest, ROI) surrounding the SBC in the femur (a,b) and tibia (c,d), under a 750 N load. Note the increased values for intra-osseous stress (b,d - arrowheads) in the cross section of the shell ROI with the synthetic SBC when compared to the same patient's knee without a SBC (a,c).

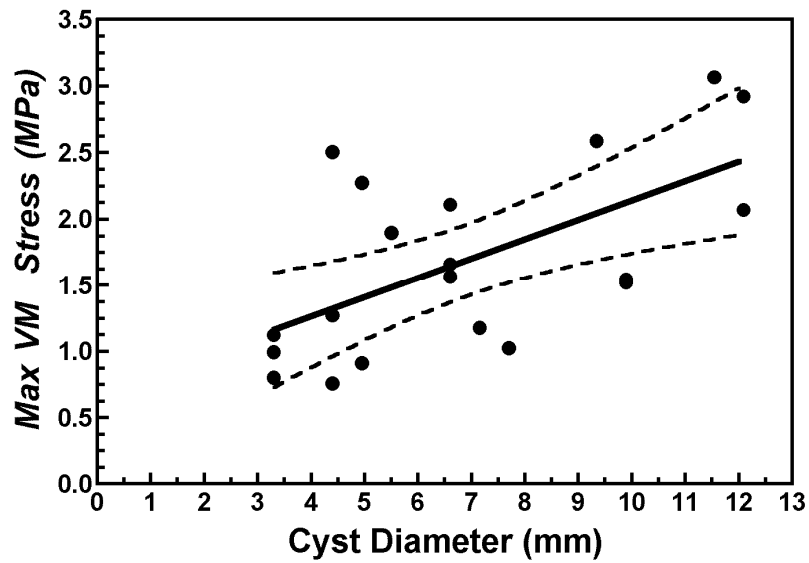


Figure 3-5: Linear regression analysis of maximum von Mises stress versus cyst (SBC) diameter. The slope of the line (i.e. solid line; 95% confidence intervals, dashed lines) was significantly non-zero ($p = 0.0043$) with an r-squared value of 0.372, suggesting that an increase in the diameter of the intra-osseous SBC contributed to the increase in stress values in the surrounding bone.

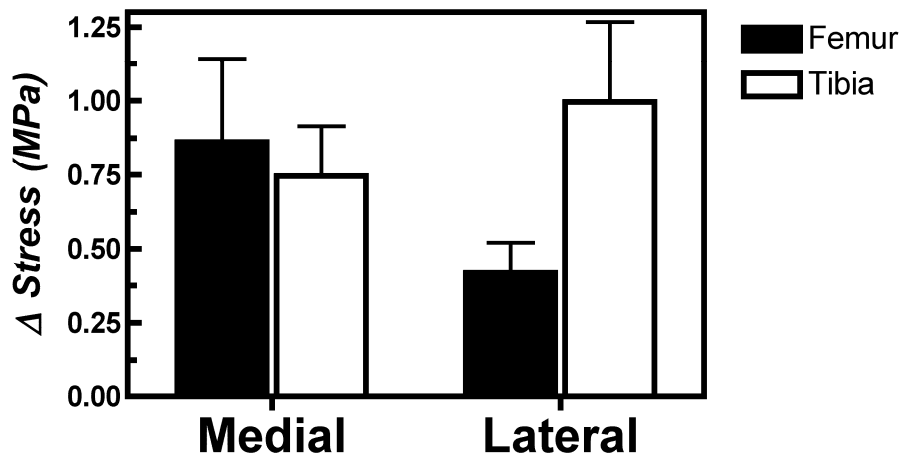


Figure 3-6: Effect of the simulated cysts (SBC) locations on the increased stress (MPa) within all four regions of the knee. SBC (5 per region) were placed within the weight-bearing bone of the medial and lateral femur or tibia. A two-way ANOVA found no significant differences between either the bones, nor the compartments ($p > 0.05$).

3.4 Discussion

The purpose of this study was to determine the effect, if any, of the presence of synthetic SBC on the intra-osseous stress pattern in the knee under a single-leg stance simulation. In order to do so, we utilized *in vivo* 3D CT data from a cohort of early OA patients, previously acquired for another study, to create FE models with heterogeneous material properties. Our findings demonstrate that within the identical early OA knee, the presence of an intra-osseous defect lead to a significant increase (approximately 81% for all patients) in the maximum peri-cystic stress values under mild static loading (i.e. one body weight). The SBC design and implementation was based on clinical findings of SBC in symptomatic knees [10, 34], and the linear regression indicated that 37% of the variance in intra-osseous stress is explained by the variance in the SBC diameter; the slope of the regression line was significantly non-zero.

Ondrouch first reported the effect of cysts on the biomechanical properties of bone under physiological load [13] in a study that modeled the stress distribution in the hip and indicated that the SBCs in OA may develop as a result of stress-induced bone resorption. Recent work using FE analysis corroborated the theory that the presence of SBC in the hip led to dramatic increases in intra-osseous stress on either bone under weight-bearing [20]. A major strength of our study was the fact that we performed our FE simulations in 3D using full knee models from actual OA patients, rather than assembled from basic shapes or patterns that resemble human joints. In our study, no immediate changes were found in the opposing bone of the knee that did not contain the SBC, similar to the ‘kissing’ lesions found in the acetabulum, which may be due to different anatomical configurations of the knee versus the hip joint.

We found that major increases in peri-cystic stress were concentrated on the volume of bone that was closest to the joint surface when a SBC was present (Fig. 3-4b). Here, the subchondral bone plate is susceptible to breach through unhealed microfracture, due to excessive loading or in response to trauma, and could allow synovial fluid into the bone, which is one proposed mechanism for SBC formation in OA [35]. This more closely resembles the pattern of sclerotic bone formation adjacent to the joint space found in a previous investigation on SBC formation and disease progression in a preclinical, post-

traumatic model of OA [14]. Furthermore, the inflammatory cells found within the lining of human SBC are capable of differentiating into osteoclasts [36], which would promote further bone resorption and subsequent cyst expansion. Sabokbar et al. implied that increased pressure within the OA bone could evoke a macrophage response within the marrow regions [36]. Our results suggest that the cells within the bone, adjacent to the SBC, are responding to the mechanical forces, as there was an almost two-fold (81%) increase in peri-cystic, intra-osseous stress under modest loading. Further analysis on the effect of the exact 3D location of the SBC within weight-bearing regions of the knee is possible using the full joint FE models described in this study, which may further our understanding of the impact of SBC. Our results indicated that less than half of the variance in stress was attributed to the change in SBC diameter (Fig. 3-5), and in one case the patient's stress values only increased by about 12% (Fig. 3-3b, Table 3-1).

To the best of our knowledge, this is the first application of patient-specific FE models to evaluate the biomechanics of the whole knee under normal weight-bearing conditions. The processing time for each patient's knee data was under 2 hours, and when combined with the average FE solution time (slightly over 1 hour), indicate the utility of patient-specific biomechanical modeling in both clinical and basic science research. As seen in Figure 3-2, the knee models – using heterogeneous material property mapping of the bones, and a uniform mapping of soft tissue – produced a realistic weight-bearing pattern as the distribution of stress was adequately transmitted from the initial contact on the joint surface, through the subchondral bone where SBCs are typically found, to the cortical bone of the tibial diaphysis. This subject-specific technique and FE analysis methods could be applied retrospectively to any patient population – particularly with unique pathologies, such as SBC – that have previously acquired CT volumes of articular joints, to further validate our findings. Furthermore, the combination of CT and MRI images could lead to more elaborate patient-specific FE models that could provide comprehensive analysis of bone and soft tissue biomechanics, which would be able to detect the subtle variations in joint composition and structure that cause the initiation and progression of OA. The use of a spherical shell ROI, created from the elements immediately adjacent to the SBC, was a unique utility that allowed for direct statistical comparison between the matched patient data. This method was adapted from previous

work investigating the distribution of stress surrounding SBC in the hip, which was two-dimensional in nature [20].

The use of subject-specific FE models has become increasingly common, though normally these studies utilize cadaveric specimens [22, 37] to ensure a large sample size in conjunction with either validation, or correlation with mechanical testing [28, 38]. Our study demonstrates the feasibility of patient-specific FE analysis, through the retrospective use of a large sample of *in vivo* knee OA data exclusively. Each FE model was composed of the material properties unique to each bone within that individual at the time of their CT scan. Often, a global material property is assigned to the bone while incorporating other soft tissues [39] such as cartilage, in order to reduce model complexity and increase the rate of convergence. However, our work was focused on the specific response of early OA bone, surrounding synthetic SBCs in the knee, under basic loading conditions, which required a more comprehensive depiction of material properties. Morgan et al. developed several bone density-modulus relationships experimentally using samples taken from several anatomic sites [28], which have demonstrated excellent prediction characteristics when applied to subject-specific FE models validated against in-vitro testing of human cadaveric specimens [38].

Conventional CT imaging does not exhibit adequate soft-tissue contrast to accurately delineate the layer of cartilage lining the joint surfaces of the knee, thereby precluding the use of CT to define specific geometries for these tissues. The use of the patient's actual cartilage, derived from a co-registered MRI, would enhance the accuracy of the model, however, this would cause a significant increase in complexity for both model convergence and computational time. To compensate for this limitation, we chose to assign material properties to the non-bone elements that represented the behaviour of cartilage under compression [33]. Another limitation to this study was the introduction of a synthetic SBC to monitor its effect on OA joints. The patient knee data used were all in the early stage of disease, and no naturally occurring SBCs were found. However, this was expected, as previous studies confirmed SBCs occur primarily in more advanced stages of OA [15, 16, 34]. Our study is not the first to employ synthetic bone damage to study its influence on joint mechanics. Shirazi et al. simulated damage to subchondral

bone and calcified cartilage by reducing the elastic moduli of specified elements within their FE model of the knee [39]. Conversely, our synthetic SBCs were geometrically designed within the FE model, and assigned negligible material properties under the assumption that, with quasi-static equilibrium loading, the fluid filled regions of the SBC would freely diffuse under load at a slow rate to offset any drag forces or hydraulic stiffening [40] found within the trabeculae, thereby negating any possible increase in intra-osseous pressure or impedance. The presence of a sclerotic margin around the SBC has been described for some cases [13], though there is no consensus of the presence of any membrane surrounding the SBC [16, 41], which could also prevent fluid flow amongst the trabeculae.

Monitoring the effect of SBC on intra-osseous stress in early OA joints was achieved using pre-existing imaging technology, which is able to produce highly specified patient-by-patient biomechanical analyses of articular joints. We feel that through future developments in hardware design – with few infrastructure improvements – patient-specific biomechanical modeling could be performed routinely to assess: the *in vivo* response of diseased bone to novel pharmacological therapies; the impact, or design, of orthopaedic implants; or the efficacy of patient bone to surgical interventions designed to alter joint loading. This study was the first to incorporate these methods using a cohort of OA knee image volumes to perform patient-specific FE analysis, leading to a better understanding of how intra-osseous defects can alter the stress distribution within the knee under a single-leg stance. Our results indicate that increased peri-cystic stress within the bone of OA knees is the mechanism by which the majority SBCs tend to expand over time [34], as the values under relatively mild loading (i.e. only 1 body weight) are within the reported range for the ultimate compressive strength of trabecular bone (0.51 - 5.6 MPa) [42]. Repeated, or increased, loading beyond 1 body weight may lead to stress-induced bone resorption and further cyst expansion; this type of expansion has been previously described in hip lesions [20, 21]. However, in the knee, the tendency for the increased peri-cystic, intra-osseous stress appeared closer to the articular surface that corresponds to the formation of sclerotic margins seen in clinical and preclinical studies of cyst formation [13, 14].

3.5 References

1. Lajeunesse, D. and P. Reboul, *Subchondral bone in osteoarthritis: a biologic link with articular cartilage leading to abnormal remodeling*. *Curr Opin Rheumatol*, 2003. **15**(5): p. 628-33.
2. Dequeker, J., L. Mokassa, and J. Aerssens, *Bone density and osteoarthritis*. *J Rheumatol Suppl*, 1995. **43**: p. 98-100.
3. Badley, E.M. and P.P. Wang, *Arthritis and the aging population: projections of arthritis prevalence in Canada 1991 to 2031*. *Journal of Rheumatology*, 1998. **25**(1): p. 138-44.
4. Davis, M.A., et al., *The association of knee injury and obesity with unilateral and bilateral osteoarthritis of the knee*. *Am J Epidemiol*, 1989. **130**(2): p. 278-88.
5. Badley, E.M. and P.P. Wang, *The contribution of arthritis and arthritis disability to nonparticipation in the labor force: a Canadian example*. *Journal of Rheumatology*, 2001. **28**(5): p. 1077-82.
6. Goldstein, J.L., L.R. Larson, and B.D. Yamashita, *Prevention of nonsteroidal anti-inflammatory drug-induced gastropathy: clinical and economic implications of a single-tablet formulation of diclofenac/misoprostol*. *Am J Manag Care*, 1998. **4**(5): p. 687-97.
7. Mukherjee, D., S.E. Nissen, and E.J. Topol, *Risk of cardiovascular events associated with selective COX-2 inhibitors*. *JAMA*, 2001. **286**(8): p. 954-9.
8. Felson, D.T. and T. Neogi, *Osteoarthritis: is it a disease of cartilage or of bone?* *Arthritis Rheum*, 2004. **50**(2): p. 341-4.
9. Javaid, M.K., et al., *Pre-radiographic MRI findings are associated with onset of knee symptoms: the most study*. *Osteoarthritis Cartilage*, 2009.

10. Crema, M.D., et al., *Contrast-enhanced MRI of subchondral cysts in patients with or at risk for knee osteoarthritis: The MOST study*. Eur J Radiol, 2009.
11. Felson, D.T., et al., *The association of bone marrow lesions with pain in knee osteoarthritis*. Ann Intern Med, 2001. **134**(7): p. 541-9.
12. Crawford, R., et al., *Expansion of an osteoarthritic cyst associated with wear debris: a case report*. J Bone Joint Surg Br, 1998. **80**(6): p. 990-3.
13. Ostlere, S.J., L.L. Seeger, and J.J. Eckardt, *Subchondral cysts of the tibia secondary to osteoarthritis of the knee*. Skeletal Radiol, 1990. **19**(4): p. 287-9.
14. McErlain, D.D., et al., *Study of subchondral bone adaptations in a rodent surgical model of OA using in vivo micro-computed tomography*. Osteoarthritis Cartilage, 2008. **16**(4): p. 458-69.
15. Kornaat, P.R., et al., *Osteoarthritis of the knee: association between clinical features and MR imaging findings*. Radiology, 2006. **239**(3): p. 811-7.
16. Marra, M.D., et al., *MRI features of cystic lesions around the knee*. Knee, 2008. **15**(6): p. 423-38.
17. Roemer, F.W., F. Eckstein, and A. Guermazi, *Magnetic resonance imaging-based semiquantitative and quantitative assessment in osteoarthritis*. Rheum Dis Clin North Am, 2009. **35**(3): p. 521-55.
18. Austman, R.L., et al., *The effect of the density-modulus relationship selected to apply material properties in a finite element model of long bone*. J Biomech, 2008. **41**(15): p. 3171-6.
19. Viceconti, M., et al., *Automatic generation of accurate subject-specific bone finite element models to be used in clinical studies*. J Biomech, 2004. **37**(10): p. 1597-605.

20. Durr, H.D., et al., *The cause of subchondral bone cysts in osteoarthritis: a finite element analysis*. Acta Orthop Scand, 2004. **75**(5): p. 554-8.
21. Ondrouch, A.S., *Cyst formation in osteoarthritis*. J Bone Joint Surg Br, 1963. **45**: p. 755-60.
22. Crawford, R.P., C.E. Cann, and T.M. Keaveny, *Finite element models predict in vitro vertebral body compressive strength better than quantitative computed tomography*. Bone, 2003. **33**(4): p. 744-50.
23. Suan, J.C., et al., *4 T MRI of chondrocalcinosis in combination with three-dimensional CT, radiography, and arthroscopy: a report of three cases*. Skeletal Radiol, 2005. **34**(11): p. 714-21.
24. Kellgren, J.H. and J.S. Lawrence, *Radiological assessment of osteo-arthritis*. Ann Rheum Dis, 1957. **16**(4): p. 494-502.
25. White, D.R., *Tissue substitutes in experimental radiation physics*. Med Phys, 1978. **5**(6): p. 467-79.
26. Chen, G., et al., *A new approach for assigning bone material properties from CT images into finite element models*. J Biomech, 2009.
27. Perillo-Marcone, A., A. Alonso-Vazquez, and M. Taylor, *Assessment of the effect of mesh density on the material property discretisation within QCT based FE models: a practical example using the implanted proximal tibia*. Comput Methods Biomech Biomed Engin, 2003. **6**(1): p. 17-26.
28. Morgan, E.F., H.H. Bayraktar, and T.M. Keaveny, *Trabecular bone modulus-density relationships depend on anatomic site*. J Biomech, 2003. **36**(7): p. 897-904.
29. Helgason, B., et al., *Mathematical relationships between bone density and mechanical properties: a literature review*. Clin Biomech (Bristol, Avon), 2008. **23**(2): p. 135-46.

30. Wirtz, D.C., et al., *Critical evaluation of known bone material properties to realize anisotropic FE-simulation of the proximal femur*. J Biomech, 2000. **33**(10): p. 1325-30.
31. Boschetti, F., et al., *Biomechanical properties of human articular cartilage under compressive loads*. Biorheology, 2004. **41**(3-4): p. 159-66.
32. Mow, V.C., et al., *Biphasic creep and stress relaxation of articular cartilage in compression? Theory and experiments*. J Biomech Eng, 1980. **102**(1): p. 73-84.
33. Mow, V.C. and X.E. Guo, *Mechano-electrochemical properties of articular cartilage: their inhomogeneities and anisotropies*. Annu Rev Biomed Eng, 2002. **4**: p. 175-209.
34. Tanamas, S.K., et al., *The association between subchondral bone cysts and tibial cartilage volume and risk of joint replacement in people with knee osteoarthritis: a longitudinal study*. Arthritis Res Ther, 2010. **12**(2): p. R58.
35. Resnik, D. and M. Kransdorf, *Degenerative Diseases*, in *Bone and Joint Imaging*, A. Ross, Editor. 2005, Elsevier Inc.: Philadelphia, PA. p. 356-443.
36. Sabokbar, A., et al., *Macrophage-osteoclast differentiation and bone resorption in osteoarthrotic subchondral acetabular cysts*. Acta Orthop Scand, 2000. **71**(3): p. 255-61.
37. Cody, D.D., et al., *Femoral strength is better predicted by finite element models than QCT and DXA*. J Biomech, 1999. **32**(10): p. 1013-20.
38. Schileo, E., et al., *Subject-specific finite element models can accurately predict strain levels in long bones*. J Biomech, 2007. **40**(13): p. 2982-9.
39. Shirazi, R. and A. Shirazi-Adl, *Computational biomechanics of articular cartilage of human knee joint: effect of osteochondral defects*. J Biomech, 2009. **42**(15): p. 2458-65.

40. Ochoa, J.A., et al., *Stiffening of the femoral head due to inter-trabecular fluid and intraosseous pressure*. J Biomech Eng, 1991. **113**(3): p. 259-62.
41. Bancroft, L.W., J.J. Peterson, and M.J. Kransdorf, *Cysts, geodes, and erosions*. Radiol Clin North Am, 2004. **42**(1): p. 73-87.
42. Rohl, L., et al., *Tensile and compressive properties of cancellous bone*. J Biomech, 1991. **24**(12): p. 1143-9.

Chapter 4

4 Patient-Specific Finite Element modeling of the Early OA Knee using Image-Based Material Properties

4.1 Introduction

Osteoarthritis (OA) is complex disorder of the bone and overlying cartilage within articular joints [1, 2] that leads to significant pain and disability [3, 4]. Despite extensive research and development on disease modifying therapies, an effective treatment that can reverse or cease the disease progression remains elusive [5]. Often clinical or pre-clinical OA research will focus on individual tissue types when attempting to modify or characterize its pathogenesis, though there is no consensus on the role of bone, cartilage, or synovium as the initiator of the disease [6-9]. Nonetheless, the ability to monitor the biomechanical behaviour of synovial joints offers the potential to identify early-stage risk factors for OA progression. In addition, the composition and function of the various components within early OA joints could be used as objective and quantitative measures for disease-modifying therapies, whether surgical [10, 11] or pharmacological [12] in nature.

The use of finite-element analysis (FEA) to describe the mechanical behavior of joints has become increasingly prevalent. Often, FEA studies within the knee employ the use of cadaveric specimens to explore a specific injury mechanism that can be surgically introduced in the joint [13, 14], or to validate the model design and behavior of specific tissues [15, 16]. Studies in other joints – and those using cylindrical core specimens from the femur or tibia – focused on validation of observed behavior with mechanical testing, often to failure, which precluded *in vivo* application to a patient population [17-19]. Moreover, the applied load during validation studies often approaches the physiological limits of healthy tissue [20] and therefore may not be sensitive to subtle changes in tissue behavior that can distinguish between loads that may or may not cause progression. In Chapter 3, we reported that the presence of a subchondral cyst within the knee caused a

nearly two-fold increase in intra-osseous stress under a simple, single-leg stance load; possibly initiating sclerosis or further cyst expansion [21].

The incorporation of high-resolution medical imaging techniques with sub-mm voxel dimensions has enhanced current FE model design and complexity. Specifically, the use of computed tomography (CT) has rapidly advanced our understanding of the mechanical behavior of bone through the use of voxel-based conversions from bone mineral density (BMD) – derived directly from the Hounsfield number within the voxel – to elastic modulus in many anatomical sites [22, 23]. Thus, the concept of subject and patient-specific FEA that utilizes the external geometry of joints – coupled with the intrinsic mechanical properties unique to each bone – has emerged [14, 24]. However, due to hardware limitations (or the need to reduce complexity to improve the probability of mesh convergence) previous studies simplified the depiction of the cartilage and menisci or eliminated them entirely. Moreover, those FEA studies that monitor the biomechanics of cartilage or meniscus typically assign bones as non-deformable rigid-bodies; producing accurate measures of contact pressure or area while relinquishing any valuable intra-osseous information [15, 25]. The enhanced detail required to monitor the intricate micro-fibril architecture in cartilage may require the creation of a sub-model of the knee (i.e. only one compartment or contact surface) [26], which must make assumptions about the natural loading conditions. It is unclear whether a sub-model, or a model using a single bone [27], has any effect on the loading pattern experienced within the FE model, and if it reflects what is actually occurring in the *in vivo* setting. Recent work has utilized *in vivo* clinical imaging data [12, 28] to construct and test subject-specific biomechanics in the ankle and spine with relatively large sample sizes, although the soft tissue was not derived from MRI data. Moro-oka et al. successfully combined CT and MRI data in several healthy knee volunteers [29] but only for the purpose of collecting kinematic data.

We report the implementation of patient-specific FEA modeling in an inclusive manner, which will allow for high-throughput analyses of the biomechanical properties in the early OA knee. Our models combine heterogeneous material mapping of the bones, obtained from a low-dose CT image, with a small element size to allow for the detection

of subtle changes in joint configuration and their effect on the mechanical ability of the knee under simple weight-bearing. In addition, our methods are capable of accurate and reproducible results for cartilage and meniscus, without an adverse effect on FE solution time, by utilizing a co-registered MRI image to capture the relevant soft tissue components within the knee. This retrospective study will show that comprehensive modeling of all tissues involved in the weight-bearing knee can improve our ability to detect and monitor stress and contact variations in bone and soft tissues with the intent to apply this technique in future high-throughput clinical studies.

4.2 Methods

4.2.1 Early OA patients and Imaging Protocols

As part of a previous study, 50 early knee OA patients (Kellgren-Lawrence score ≤ 2) were scanned in our laboratory with a prototype cone-beam 3D CT system (Multistar, Siemens Medical Solutions, Erlangen, Germany) and a 4T MRI (Unity Inova; Varian, Palo Alto, Calif.; Siemens, Erlangen, Germany), prior to undergoing arthroscopic surgery [30]. Informed consent was obtained in accordance with the approval from the ethical review board at the University of Western Ontario prior to any imaging experiments, and all data was anonymized before FE model design and implementation. Prior to CT imaging, all patients had their affected knee splinted and a tissue calibrator was placed along the joint line. This calibration device (SB3, Gamex RMI, Middleton, US) ensured that the reconstructed data set was scaled in appropriate Hounsfield units (HU), and voxels containing bone were calibrated to values of volumetric bone mineral density ($\text{mg} \cdot \text{cm}^{-3}$ of hydroxyapatite). CT scan parameters were: 135 x-ray projections, taken at 1.5° increments over 4.4 seconds, exposures of 90 kVp and 40 mA·s, and reconstructed 3D data set with 0.55 mm isotropic voxel spacing. Two MRI sequences, both using fat suppression, were acquired in the sagittal plane: a 3D T1-weighted spoiled gradient (SPGR) sequence with a $512 \times 256 \times 64$ matrix and $0.23 \times 0.47 \times 1.5 \text{ mm}^3$ voxels, and a 2D proton density-weighted fast spin echo (FSE) sequence with a 512×384 matrix and $0.23 \times 0.32 \times 3.0 \text{ mm}^3$ voxels. The SPGR and FSE sequences had acquisition times of

13.6 and 12.8 min, respectively. Eight patients' dual-modality knee images ($N = 8$) were selected for use in our study, based on image quality and a sufficient field of view to extract all relevant tissues.

4.2.2 Patient-specific FEA model creation

The reconstructed 3D MRI images were resampled with isotropic voxel spacing (0.55 mm), which allowed for landmark-based, rigid-body registration with the CT volumes. All images were analyzed in multi-planar reformatted view using MicroView (v.2.1.2, General Electric Health Care, London, Canada) software. To increase the accuracy of the registration – and account for the patients movement between CT and MRI scans – the individual bones in the CT image (i.e. patella, femur, tibia and fibula) were registered separately to the MRI, which maintained the true bone-cartilage and ligament-bone interfaces. The surface geometry of each bone was automatically segmented using threshold-based, isosurface rendering. The geometries for soft-tissue structures (i.e. patella-femoral and femoral-tibial cartilage, menisci, cruciate ligaments, patellar tendon) that are relevant to single-leg weight-bearing were semi-automatically segmented and interpolated from key-frames in the MRI image via the advanced region of interest (ROI) tool in MicroView. As the bone-cartilage and bone-ligament interfaces were acquired from the CT-MRI registration (described below, Figure 4-1), the user concentrated on an accurate segmentation of the articulating cartilage surfaces and ligament dimensions for more efficient workflow. All resultant triangulated surfaces were exported in stereolithography (STL) format into Geomagic Studio (v.10, Geomagic, North Carolina, USA) for post-processing. This ensured that the imported structures were topologically valid, with no holes, rough edges, or non-physiological defects prior to importing them as solid, deformable bodies into the commercial FE software package (Abaqus CAE v.6.8.3, Simulia, Rhode Island, USA). All components were oriented in 3D to the MRI coordinate system to maintain their relative locations. The femoral and tibial cartilage solids were converted initially to a shell, preserving the outer boundaries, and joined to the respective bones (i.e. merging procedure) where the inner bone-cartilage interface is defined by the outer surface of the bone. This process eliminated any material erroneously segmented as 'cartilage' from the interior structure; subsequently

the remaining portion between the boundary of bone and the articulating cartilage surface (i.e. layer of cartilage seen in MRI) is converted back to a solid body.

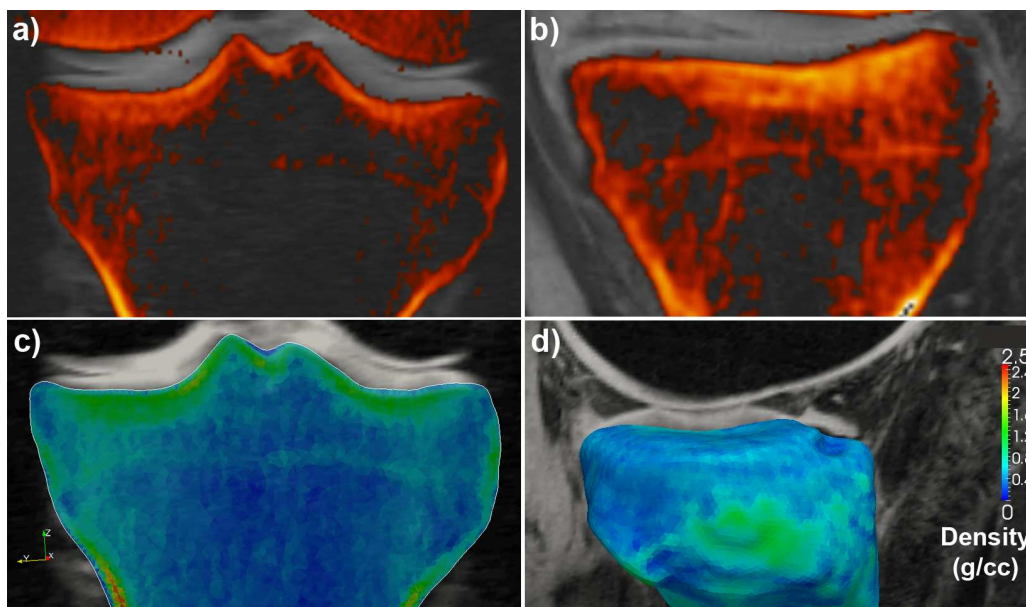


Figure 4-1: Coronal (a,c) and Sagittal (b,d) views of 3D registration for accurate cartilage segmentation using GEHC MicroView. Individual knee bones from the CT image were sequentially co-registered to the MRI volume that reduced the time required for soft-tissue segmentation of each subject-specific FE models (shown in orange overlying the MRI - a,b). The outer surface of the femur and tibia bones served as the templates when merged in the FE model with the corresponding cartilage components. Consequently, the bone-cartilage interfaces are defined more accurately using a dual-modality approach versus MRI imaging alone. The CT image can be converted and displayed in volumetric BMD values (c,d), or rendered in 3D to extract the contact surfaces (d - scale bar depicts apparent mineral density).

4.2.3 Model Assembly and Pilot Studies

Linear, 4-node tetrahedral elements, with a 1 mm edge length, were used for all tissues within the FE models of the knee, which ensured reasonable solution times [21, 31] while maintaining the inter- and intra-subject variability in tissue shape and dimension. Once the lateral and medial menisci were added to the model, six finite sliding, contact pairs were defined between: the femoral and patellar cartilage, femoral and tibial cartilage, femoral cartilage and both menisci, and the tibial cartilage and both menisci. The

cartilage-cartilage contact pairs were defined as frictionless, while the cartilage-menisci pairs were assigned a coefficient of friction of 0.1 [8]. The menisci horns were attached to the bone with a series of linear springs (10 per horn; 200 N/mm each, resulting in 2000 N/mm total stiffness) [15], and the anterior horns were connected via a 900 N/mm spring, which mimicked the transverse ligament [32].

A subset of FE models ($n = 4$) were used for pilot studies that assessed the effect of both bone material property assignment, and reduction in size of the FE model, which are common approximations. To assess how different assumptions of bone material properties affect the final FE results, the subset models underwent loading trials where the bone properties were assigned by three different approaches: (1) as a rigid-body, allowing no deformation; (2) with a uniform modulus of elasticity (5 GPa) for all elements [25]; (3) with material properties assigned on an element-by-element basis using a non-linear, BMD-to-elastic-modulus conversion, derived directly from the CT scan [21, 33]. For each patient in the pilot study, all three FE models underwent identical loading simulations, where the soft tissues were assigned identical properties described below. To assess the effect of the reduction in model size on the FE results, each model within the group had a duplicate model designed that was limited to a 50 mm axial extent (i.e. extending 25 mm on each side of the femoral-tibial junction). Careful attention was made to include as much of the contacting cartilage surfaces on either bone as possible. However due to the size constraint, the patella and its tendon were not included.

The elastic modulus for all soft tissues was chosen based on established literature values [15, 34-36], and is summarized in Table 4-1. All models underwent a 750 N compressive load in the vertical direction wherein the femur acted upon the tibia, which was fixed at the inferior end. The load was distributed along a 4 mm wide band in the cortical bone of the femur for all full-length models; the vertically reduced FE models in the pilot study had an identical plane created in the metaphyseal bone of the femur. The patellar tendon had a 150 N tensile load that was applied evenly over the cross-sectional area along the oblique course of the tendon on the superior aspect of the patella (Figure 4-2), which represented any passive tension that may occur during single-leg stance [37]. Once more, this load was omitted in the pilot study using the 50 mm FE models. Due to the lack of

collateral ligaments and supporting tendons present in the models, the femoral bone elements were limited to vertical movements, which prevented non-physiological stress concentrations or motions.

Table 4-1: Mechanical properties assigned for all tissues within our subject-specific FE models. Note the elastic moduli (MPa) for all FE elements in bones were assigned directly from the CT-volume (multiple), using a BMD to elastic modulus conversion.

	Bone	Cartilage	Meniscus	Ligaments	Tendon
Elastic Modulus	50 – 21000	15.0	59.0	50	300
Poisson's Ratio	0.3	0.475	0.49	0.3	0.35

4.2.4 Data Analysis

The resultant maximum von Mises stress values for the medial and lateral menisci and the tibial and femoral cartilage, in the pilot study that assessed the effect of different bone moduli, were compared using a one-way, repeated measures ANOVA. The differences in stress values between the full length and the reduced (50 mm) FE models of the same knees ($n = 4$) were compared using a paired t-test. An alpha level for values of $p < 0.05$ was considered significant. All of the full length, multi-material bone FE models ($n = 8$) were monitored for maximum contact pressure (MPa), contact area (mm^2), and von Mises stress (MPa) within the bones, in addition to tissues listed above.

4.3 Results

The full length, patient-specific FE models were assembled successfully with an average of 1.5 million elements (Figure 4-2). The solutions were obtained in approximately 25 hours using commercially available hardware, while the simulations in the pilot studies took an average 46, 8, and 12 hours for the models with homogeneous bone, rigid body bone, and vertically reduced models, respectively.

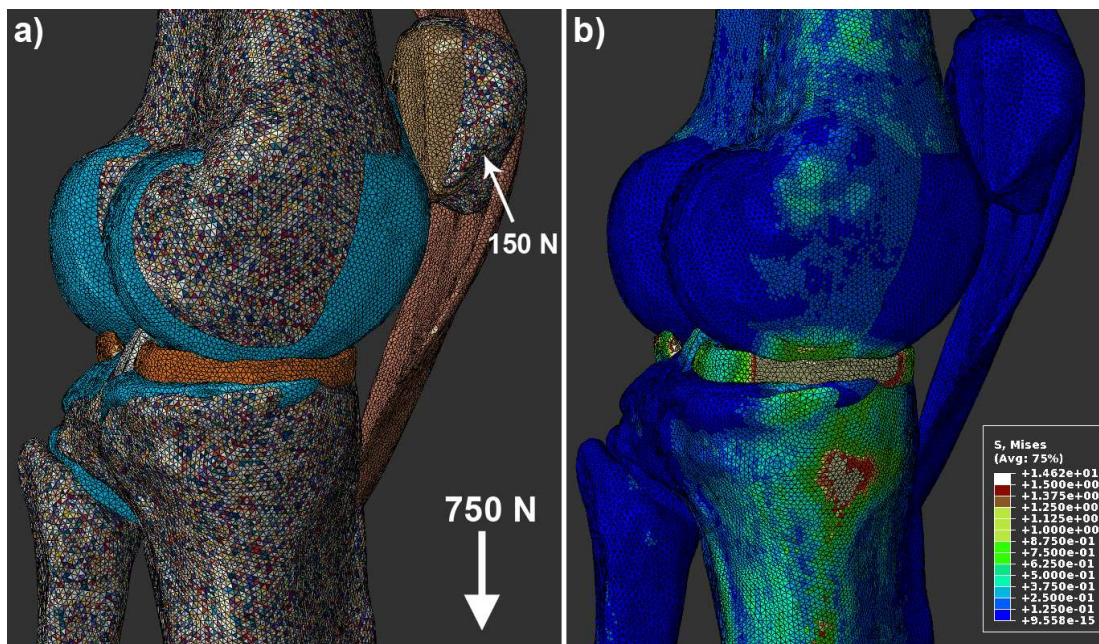


Figure 4-2: Medial view of the assembly of a bone-inclusive, multi-material FE model of the early OA knee. Linear, tetrahedral elements with 1 mm edge length were used for all structures derived from the co-registered, dual-modality images of bone (CT-derived) and soft tissue (MRI-derived). Each colour (a) represents a unique material property assigned from literature values or using a known BMD-to-elastic modulus conversion, allowing for accurate representation of stress throughout the knee (b; scale in MPa). A 750 N load was applied vertically downward along the cortical bone of the femur, whose elements were limited to movement in the vertical axis. A 150 N tensile load, which simulated passive tension during full knee extension, was applied normally to a transverse section of the superior surface of the patellar tendon.

The maximum stress values within the cartilage and menisci did not differ by more than 3% when the bones were assigned as rigid bodies, or having either a homogeneous elastic modulus (5 GPa) or a heterogeneous modulus derived from the CT data (Table 4-2). However, upon 3D display it is evident that the maximum stress values – in particular within the meniscus and subchondral bone – occur in different locations given the same patient knee ($n = 4$, Figure 4-3). Furthermore, when the vertically reduced model was compared to the full-length results, stress values within the subchondral bone and lateral meniscus were underestimated and the area wherein these high stress values occur was diminished.

The average maximum values for stress, contact pressure and area for all of the multi-material bone FE models ($n = 8$) are summarized in Table 4-3. Under single-leg stance loading (750 N) the highest resultant stress occurred within the menisci (14.2 ± 1.76 and 11.3 ± 1.73 MPa, for the lateral and medial meniscus, respectively), followed by the bones (14.4 ± 2.5 and 6.60 ± 0.78 MPa, for the tibia and femur, respectively). The contact between the femoral cartilage and the menisci resulted in the highest pressure values (Figure 4-4), though the contact area was approximately half of the contact area between the tibia and the menisci, which were attached to the tibia via the series of linear springs simulating the ligaments on the anterior and posterior horns.

Table 4-2: Pilot study assessing the effect of assigning different elastic moduli for bone on resultant soft tissue stress. Values shown are the mean maximum von Mises stress (\pm SE), derived from all FE elements within the femur and tibia cartilage (cart.) and the lateral (lat.) and medial (med.) menisci observed in four FE models. The percent change relative to the multi-material model is shown.

BONE PROPERTIES	FEMUR CARTILAGE	TIBIA CARTILAGE	LATERAL MENISCUS	MEDIAL MENISCUS
MULTI-MATERIAL	3.06 (0.320)	1.97 (0.294)	17.6 (1.92)	10.7 (0.369)
HOMOGENEOUS	3.10 (0.331)	1.95 (0.290)	18.1 (2.03)	10.6 (0.193)
RIGID BODY	3.07 (0.320)	2.03 (0.326)	17.4 (1.76)	10.9 (0.382)
% CHANGE	1.3, 0.33	-1.01, 3.05	2.8, -1.1	-0.93, 1.9

Table 4-3: Resultant maximal values for the equivalent, von Mises stress, contact pressure, and contact area within all tissues under 750 N load. Values are mean (\pm SE) for the bone inclusive, patient-specific FE models ($n = 8$) of the early OA knee. Overlapping columns in rows 2, 3 indicate contact pairs between the medial and lateral meniscus, and the cartilage on the femur or tibia.

	Femur Cart.	Meniscus Med.	Tibia Cart.	Meniscus Lat.	Femur Bone	Tibia Bone
von Mises Stress (MPa)	2.97 (0.184)	11.3 (1.73)	1.94 (0.154)	14.2 (1.76)	6.60 (0.777)	14.4 (2.50)
Contact Pressure (MPa)	16.9 (2.57)		8.43 (2.10)	16.9 (2.64)	25.0 (4.61)	5.89 (1.33)
Contact Area (mm²)	86.6 (18.1)		149 (22.0)	208 (18.1)	104 (12.2)	95.5 (22.3)

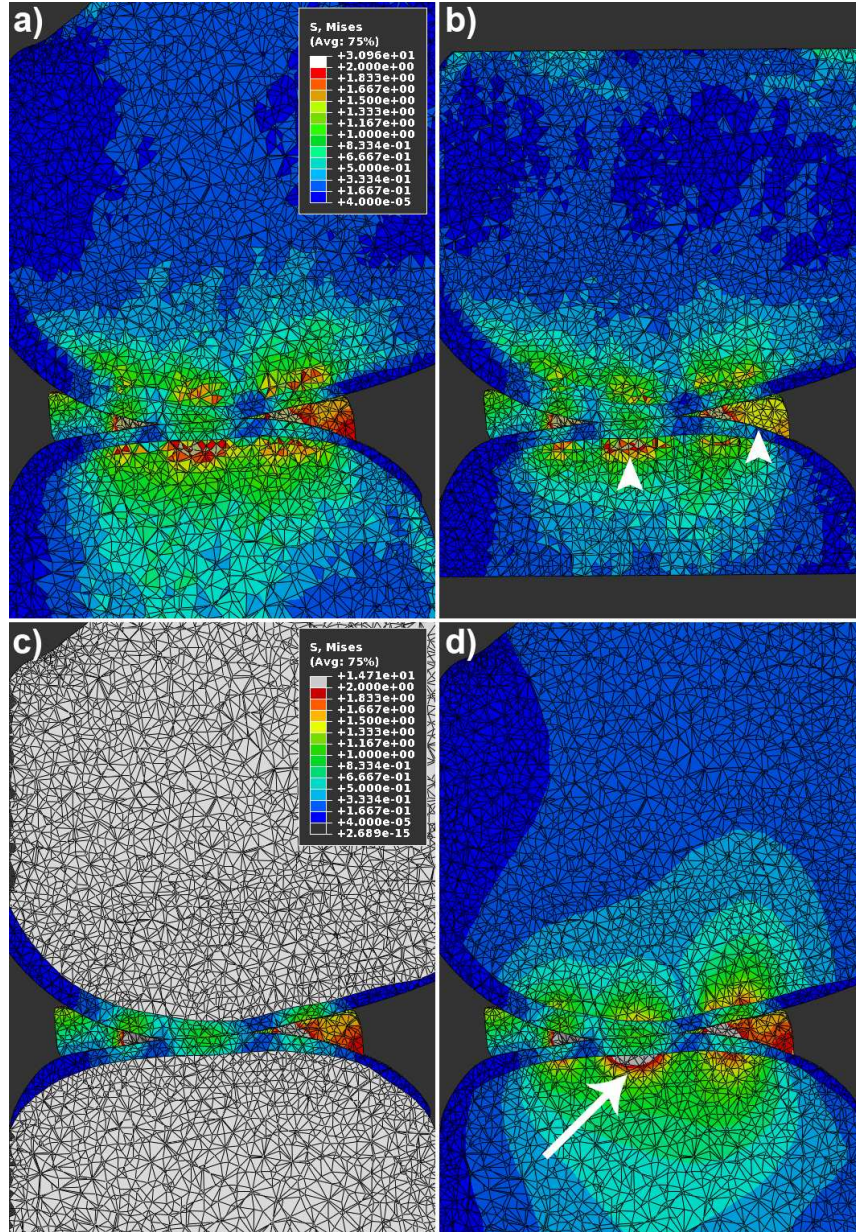


Figure 4-3: Cross-section of the lateral compartment in four FE models of the same knee. Effect of the use of a sub-model (b), or rigid body (c) or a homogeneous (d) modulus for bone on the resultant stress values within a patient-specific FE model simulation. All pilot studies underwent identical (750 N) loading conditions along a 4 mm wide section of the cortical bone, which was simulated in the 50 mm sub-model and resulted in lower stress values within the meniscus (b – right arrowhead). Maximum stress values within the bone did not appear in the same location; areas near the joint surface were either underestimated (b - left arrowhead) in the sub-model, or overestimated (d – arrow) when a uniform modulus (5 GPa) was chosen when compared to the full FE model (a), which had heterogeneous material mapping assigned from the patient’s CT image. Scale values are in MPa.

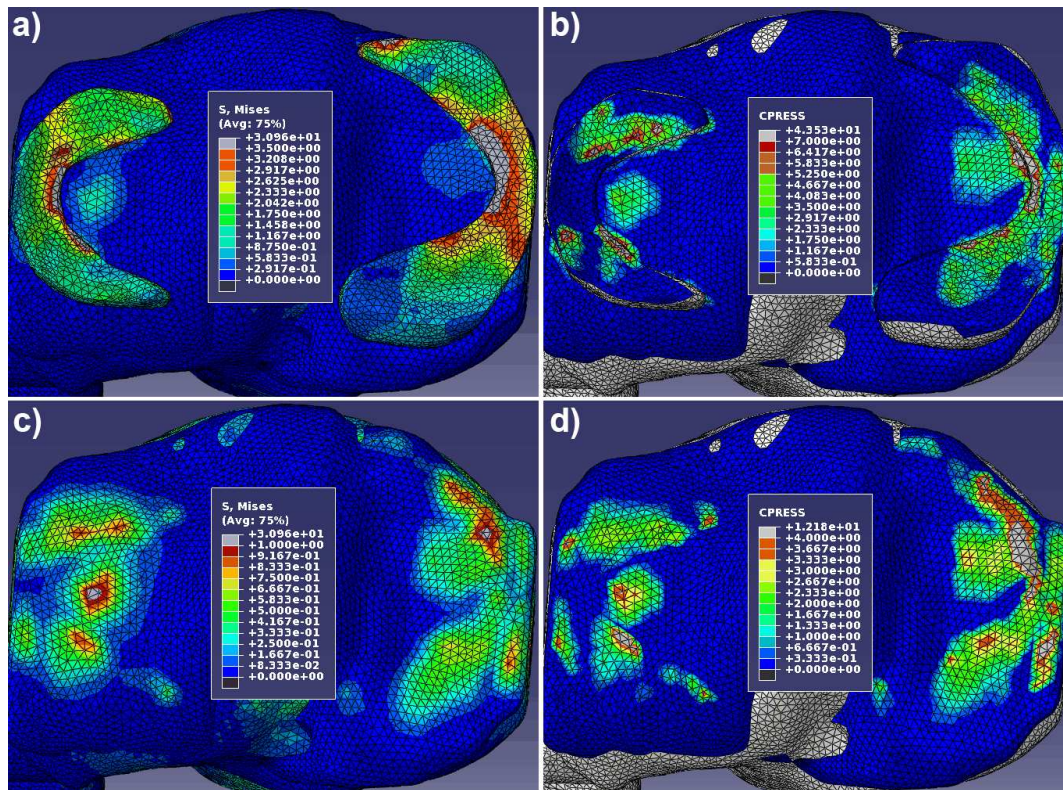


Figure 4-4: Pattern of stress and contact pressure on the tibial surface of the left knee. Values are in MPa with (a,b) and without (c,d) the menisci present to demonstrate the weight-bearing pattern distributed onto the cartilage surface. The femur was loaded onto the tibia that was fixed at the inferior end.

4.4 Discussion

To the best of our knowledge, this study is the first to produce patient-specific FEA models of the early OA knee that incorporates *in vivo*, dual-modality imaging with heterogeneous material properties assigned to the bones, which are entirely unique to the individual and derived from an established BMD-to-modulus relationship [21, 22]. In addition, this study utilized a relatively high sample number to demonstrate the feasibility of high-throughput biomechanical analyses for all bone and soft tissue structures that comprise the knee joint. The FE software and computing hardware used to obtain these results are both commercially available, and the patient data had been previously acquired indicating the potential for patient-specific FE clinical trials.

Few studies incorporate both MRI and CT scans when constructing subject or patient-specific FE models of joints [35], and many have used cadaveric samples with the intent of future *in vivo* applications [27, 38]. However, the benefits of the dual-modality approach used in this study should not be overlooked, especially when an accurate segmentation of cartilage is desired. Due to the known chemical shift artifacts associated with MR imaging along the bone-cartilage interface [39, 40], a co-registered CT scan provides a better depiction of this interface, which will lead to more accurate approximations of cartilage thickness. The delineation of the bone-cartilage interface via threshold-based rendering within the CT image precludes the manual segmentation normally required by MRI-based FE modeling alone, thus increasing efficiency (Fig. 4-1). Consequently, the user can focus on the cartilage-cartilage interfaces of the tibial-femoral and patella-femoral joints exclusively, which are better represented in the MRI. Furthermore, as changes to the layer of calcified cartilage and subchondral bone thickness, degree of mineralization, and presence of edema or cyst [21, 41, 42] have been implicated in both the progression of cartilage damage [2, 26] and risk of joint replacement [43], biomechanical investigations concerned with inhibiting OA progression require an accurate and precise depiction of the bone-cartilage interface.

Early FE model development in the knee was derived from bones imaged with CT that produced realistic geometries [15], but still required assumptions regarding the mechanical properties of the bones, which were assigned as rigid bodies (or having a homogeneous elastic modulus) to reduce solution times [35]. The inclusion of multi-material mapping of bones has led to enhanced detection of fracture risk and estimates of strength [18, 44] with a conversion from the BMD derived in each voxel to an elastic modulus in that exact 3D location [33]. We chose to build upon this existing technique by combining precise bone modeling with the soft tissues relevant to single-leg stance to enhance our ability to monitor stress and potentially OA progression. Based on the literature, we did not expect to find significant difference in stress values for the cartilage and menisci when the bone properties were not heterogeneous.

However, the pattern of stress distribution was altered with a homogeneous bone modulus (or rigid body) that lead to over or underestimations of values in both the bone and soft tissues when comparing the exact 3D location in the heterogeneous FE model (Figure 4-3). This distribution throughout the knee is of particular importance for those interested in the patient-specific differences in composition of bone or cartilage that may influence the positioning of an osteotomy plate [10] or determine the stage of fracture healing [11]. Therefore, for future clinical FEA studies interested in the surgical viability of diseased bone and cartilage – such as choosing between a hemi-arthroplasty and high-tibial osteotomy – we recommend the inclusion of heterogeneous material properties assigned from quantitative 3D imaging data. The models produced in this study could also be applied to simulations of joint damage caused by trauma, often leading to secondary OA. Studies looking at the effect of an osteochondral defect [14, 26] or varying degrees of meniscectomy [32] have shown the value of FEA but were limited to cadaveric or virtual tissue. One study demonstrated the effect of bone bruises in conjunction with varying cartilage lesions within the lateral tibial compartment [26] through a geometrically reduced FE model. Our pilot study indicates that although heterogeneous bone material properties were assigned in a vertically reduced model (50 mm), the stress pattern did not match that derived from a the full-length model, although the computational time was only reduced by a factor of two. The full-length models could greatly enhance these investigations by providing biomechanical data from *in vivo* patient knees, and we have recently shown the capability of simulating damage within the knee in a simplified case [21].

It is important to note that this was a retrospective study that only focused on structures (and loading) within the knee that were readily observable and easily measurable. Given that the MRI protocol was designed for rapid, high quality cartilage imaging we were unable to accurately segment the collateral ligaments; hence the boundary condition limiting the movement of the femur in the vertical direction only.

Prospective studies could use more current MR acquisition protocols over a larger field of view, which will enable the incorporation of ligaments and other supportive tissues (i.e. hamstring tendons) and possibly greater ranges of motion. Our bone-inclusive, full-length FE models required the greatest amount of computational time (i.e. approximately four-fold increase using heterogeneous versus rigid body bones) though we do not feel this warrants an exclusion of vital intra-osseous biomechanical data, which may be achieved in shorter time as computer-processing power increases with time. Rapid image acquisition for either CT or MRI, or custom fabrication of knee splints (which incorporate the necessary calibration phantoms needed for HU-density-modulus scaling), will further enhance the registration of dual-modality images while decreasing complexities and time associated with FE assembly. Furthermore, the advent of T2-weighted or contrast-enhanced imaging [45, 46] that can indirectly quantify subject-specific cartilage material properties (based on water concentrations) could greatly increase patient FEA specificity when used in conjunction with a co-registered CT scan. Thus, the major contributing structures – the health of which greatly contributes to overall disease progression or prognosis for recovery after therapy – could be quantified in a manner entirely unique to the patient.

The ability to monitor the biomechanical abilities within the knee of OA patients provides a tremendous utility to clinicians and scientists. Previous research focused on individual structures and their contribution to OA pathogenesis, but few have tried to fully integrate all of the relevant hard and soft tissues in a comprehensive manner. Whether due to the computational expense or the lack of dual-modality imaging, assumptions about either the bone or cartilage are made at the expense of capturing the subject-specific biomechanical variations in the knee. In order to implement FEA analysis into surgical or pharmaceutical clinical trials, we feel it is paramount to use bone-inclusive patient-specific models where the material properties of bones are easily assigned through an established voxel-based conversion of BMD-to-modulus. This is particularly important as the interplay between cartilage and bone is not entirely understood, and any assumptions or simplifications in cartilage or bone FE design reduces the ability to objectively and quantitatively monitor the individual's response to treatment. This study demonstrates that our dual-modality, bone-inclusive FEA

technique is capable of performing these studies in a high-throughput manner, and has been successfully demonstrated using a retrospective data set.

4.5 References

1. Hunter, D.J., et al., *Cartilage markers and their association with cartilage loss on magnetic resonance imaging in knee osteoarthritis: the Boston Osteoarthritis Knee Study*. *Arthritis Res Ther*, 2007. **9**(5): p. R108.
2. Radin, E.L. and R.M. Rose, *Role of subchondral bone in the initiation and progression of cartilage damage*. *Clinical Orthopaedics & Related Research*, 1986(213): p. 34-40.
3. Carr, A.J., *Beyond disability: measuring the social and personal consequences of osteoarthritis*. *Osteoarthritis and Cartilage*, 1999. **7**(2): p. 230-8.
4. Badley, E.M. and P.P. Wang, *The contribution of arthritis and arthritis disability to nonparticipation in the labor force: a Canadian example*. *Journal of Rheumatology*, 2001. **28**(5): p. 1077-82.
5. Fajardo, M. and P.E. Di Cesare, *Disease-modifying therapies for osteoarthritis : current status*. *Drugs Aging*, 2005. **22**(2): p. 141-61.
6. Andriacchi, T.P., S. Koo, and S.F. Scanlan, *Gait mechanics influence healthy cartilage morphology and osteoarthritis of the knee*. *J Bone Joint Surg Am*, 2009. **91 Suppl 1**: p. 95-101.
7. Felson, D.T. and T. Neogi, *Osteoarthritis: is it a disease of cartilage or of bone?* *Arthritis Rheum*, 2004. **50**(2): p. 341-4.
8. McCann, L., et al., *Influence of the meniscus on friction and degradation of cartilage in the natural knee joint*. *Osteoarthritis Cartilage*, 2009. **17**(8): p. 995-1000.
9. Strait, D.S., et al., *Modeling elastic properties in finite-element analysis: how much precision is needed to produce an accurate model?* *Anat Rec A Discov Mol Cell Evol Biol*, 2005. **283**(2): p. 275-87.

10. Blecha, L.D., et al., *How plate positioning impacts the biomechanics of the open wedge tibial osteotomy; a finite element analysis*. *Comput Methods Biomech Biomed Engin*, 2005. **8**(5): p. 307-13.
11. Vetter, A., et al., *The mechanical heterogeneity of the hard callus influences local tissue strains during bone healing: a finite element study based on sheep experiments*. *J Biomech*, 2011. **44**(3): p. 517-23.
12. Mawatari, T., et al., *Vertebral strength changes in rheumatoid arthritis patients treated with alendronate, as assessed by finite element analysis of clinical computed tomography scans: a prospective randomized clinical trial*. *Arthritis Rheum*, 2008. **58**(11): p. 3340-9.
13. Brown, T.D., et al., *Finite element studies of some juxtarticular stress changes due to localized subchondral stiffening*. *J Biomech*, 1984. **17**(1): p. 11-24.
14. Papaioannou, G., C.K. Demetropoulos, and Y.H. King, *Predicting the effects of knee focal articular surface injury with a patient-specific finite element model*. *Knee*, 2010. **17**(1): p. 61-8.
15. Donahue, T.L., et al., *A finite element model of the human knee joint for the study of tibio-femoral contact*. *J Biomech Eng*, 2002. **124**(3): p. 273-80.
16. Papaioannou, G., et al., *Patient-specific knee joint finite element model validation with high-accuracy kinematics from biplane dynamic Roentgen stereogrammetric analysis*. *J Biomech*, 2008. **41**(12): p. 2633-8.
17. Bevill, G., F. Farhamand, and T.M. Keaveny, *Heterogeneity of yield strain in low-density versus high-density human trabecular bone*. *J Biomech*, 2009. **42**(13): p. 2165-70.
18. Crawford, R.P., C.E. Cann, and T.M. Keaveny, *Finite element models predict in vitro vertebral body compressive strength better than quantitative computed tomography*. *Bone*, 2003. **33**(4): p. 744-50.

19. Schileo, E., et al., *An accurate estimation of bone density improves the accuracy of subject-specific finite element models*. J Biomech, 2008. **41**(11): p. 2483-91.
20. Rohl, L., et al., *Tensile and compressive properties of cancellous bone*. J Biomech, 1991. **24**(12): p. 1143-9.
21. McErlain, D.D., et al., *Subchondral cysts create increased intra-osseous stress in early knee OA: A finite element analysis using simulated lesions*. Bone, 2011. **48**(3): p. 639-46.
22. Austman, R.L., et al., *The effect of the density-modulus relationship selected to apply material properties in a finite element model of long bone*. J Biomech, 2008. **41**(15): p. 3171-6.
23. Morgan, E.F., H.H. Bayraktar, and T.M. Keaveny, *Trabecular bone modulus-density relationships depend on anatomic site*. J Biomech, 2003. **36**(7): p. 897-904.
24. Viceconti, M., et al., *Automatic generation of accurate subject-specific bone finite element models to be used in clinical studies*. J Biomech, 2004. **37**(10): p. 1597-605.
25. Gu, K.B. and L.P. Li, *A human knee joint model considering fluid pressure and fiber orientation in cartilages and menisci*. Med Eng Phys, 2011.
26. Shirazi, R. and A. Shirazi-Adl, *Computational biomechanics of articular cartilage of human knee joint: effect of osteochondral defects*. J Biomech, 2009. **42**(15): p. 2458-65.
27. Schileo, E., et al., *Subject-specific finite element models can accurately predict strain levels in long bones*. J Biomech, 2007. **40**(13): p. 2982-9.
28. Li, W., et al., *Patient-specific finite element analysis of chronic contact stress exposure after intraarticular fracture of the tibial plafond*. J Orthop Res, 2008. **26**(8): p. 1039-45.

29. Moro-oka, T.A., et al., *Dynamic activity dependence of in vivo normal knee kinematics*. J Orthop Res, 2008. **26**(4): p. 428-34.
30. Suan, J.C., et al., *4 T MRI of chondrocalcinosis in combination with three-dimensional CT, radiography, and arthroscopy: a report of three cases*. Skeletal Radiol, 2005. **34**(11): p. 714-21.
31. Chen, G., et al., *A new approach for assigning bone material properties from CT images into finite element models*. J Biomech, 2009.
32. Zielinska, B. and T.L. Donahue, *3D finite element model of meniscectomy: changes in joint contact behavior*. J Biomech Eng, 2006. **128**(1): p. 115-23.
33. Austman, R.L., et al., *Development of a customized density-modulus relationship for use in subject-specific finite element models of the ulna*. Proc Inst Mech Eng H, 2009. **223**(6): p. 787-94.
34. O'Brien, T.D., et al., *Mechanical properties of the patellar tendon in adults and children*. J Biomech, 2010. **43**(6): p. 1190-5.
35. Pena, E., et al., *A three-dimensional finite element analysis of the combined behavior of ligaments and menisci in the healthy human knee joint*. J Biomech, 2006. **39**(9): p. 1686-701.
36. Quapp, K.M. and J.A. Weiss, *Material characterization of human medial collateral ligament*. J Biomech Eng, 1998. **120**(6): p. 757-63.
37. Coupe, C., et al., *Habitual loading results in tendon hypertrophy and increased stiffness of the human patellar tendon*. J Appl Physiol, 2008. **105**(3): p. 805-10.
38. Rajapakse, C.S., et al., *Computational biomechanics of the distal tibia from high-resolution MR and micro-CT images*. Bone, 2010. **47**(3): p. 556-63.

39. McGibbon, C.A., *Inter-rater and intra-rater reliability of subchondral bone and cartilage thickness measurement from MRI*. Magn Reson Imaging, 2003. **21**(7): p. 707-14.
40. Peh, W.C. and J.H. Chan, *Artifacts in musculoskeletal magnetic resonance imaging: identification and correction*. Skeletal Radiol, 2001. **30**(4): p. 179-91.
41. Durr, H.D., et al., *The cause of subchondral bone cysts in osteoarthritis: a finite element analysis*. Acta Orthop Scand, 2004. **75**(5): p. 554-8.
42. Crema, M.D., et al., *Contrast-enhanced MRI of subchondral cysts in patients with or at risk for knee osteoarthritis: The MOST study*. Eur J Radiol, 2009.
43. Tanamas, S.K., et al., *The association between subchondral bone cysts and tibial cartilage volume and risk of joint replacement in people with knee osteoarthritis: a longitudinal study*. Arthritis Res Ther, 2010. **12**(2): p. R58.
44. Cody, D.D., et al., *Femoral strength is better predicted by finite element models than QCT and DXA*. J Biomech, 1999. **32**(10): p. 1013-20.
45. Nissi, M.J., et al., *Estimation of mechanical properties of articular cartilage with MRI - dGEMRIC, T2 and T1 imaging in different species with variable stages of maturation*. Osteoarthritis Cartilage, 2007. **15**(10): p. 1141-8.
46. Rauscher, I., et al., *Meniscal measurements of T1rho and T2 at MR imaging in healthy subjects and patients with osteoarthritis*. Radiology, 2008. **249**(2): p. 591-600.

Chapter 5

5 Conclusion and Future Directions

The purpose of this thesis was to improve our knowledge regarding the pathological changes in the subchondral bone, in particular the formation of subchondral cysts (SBC), within the OA knee. The pathological features were identified through dual-modality (i.e. CT and MRI) imaging of the ACLX knee in a validated preclinical model, which produced SBC in an identical location and pattern as seen human OA. The effect of SBC on the weight-bearing ability of the human knee was assessed using FEA of simulated lesions within a knee OA cohort that had *in vivo* CT scans acquired prior to arthroscopic surgery. Finally, an application to incorporate dual-modality knee imaging in humans with FEA to produce comprehensive patient-specific, biomechanical models of the early OA joint was developed. A summary of the findings from these studies is included below.

5.1 Summary

5.1.1 Chapter 2: *in vivo*, preclinical model of Subchondral Cyst formation

In this chapter, rats were subject to ACLX injury to initiate knee OA. Longitudinal micro-CT and MRI scans were performed at four-week intervals to track the formation of SBC within the MTP. The SBC appeared as vacant sites of bone resorption that became filled within increasing amounts of fibrous tissue and a moderate amount of mineralization by 12 weeks post-ACLX. Histological analysis confirmed the presence of a breach in the subchondral bone plate; a feature proposed as the site where SBC initiate. However, these gaps in the subchondral bone were completely filled with fibrocartilage, and are more likely caused by micro-fracture due to the overloaded joint. We conclude from this study that SBC form in response to the focal increase in mechanical loads inflicted on the bone that exceeds its compressive strength. Based on our thorough quantitative and pathological analyses, we believe the term ‘subchondral cyst’ is a

misnomer, and that SBC should be referred to as focal, ischemic OA-induced osteonecrosis (FION) to more accurately reflect their etiology.

5.1.2 Chapter 3: FEA of Simulated SBC in the early OA knee

Chapter 3 examined the effect that an intra-osseous lesion has on the weight-bearing ability of the femur and tibia. Simulated SBC or FION lesions were placed in four compartments of the knee (i.e. a spherical void within the CT volume), with known shape and dimensions derived from the literature. Two subject-specific, FEA models were designed from the CT volumes of each knee ($n = 20$) – where the material properties of the bones were assigned based on a BMD to modulus conversion – one with, and one without a SBC for statistical comparison. Under mild loading (i.e. single-leg stance, 750 N), the presence of SBC lead to an almost two-fold increase in peri-cystic bone stress. The stress distribution pattern was different from previous investigations of SBC in the OA hip, which could explain why SBC in the knee are typically smaller and more numerous. From this work, we conclude that FION lesions in the knee produce increased intra-osseous stress that exceeds the known strength of trabecular bone. Thus, the lesion is likely to expand due to stress induced bone resorption of the surrounding tissue, with sclerotic formation adjacent to the joint space.

5.1.3 Chapter 4: Patient-specific FEA modeling of the early OA knee

In the final chapter, we proposed to expand our knee FEA modeling technique by incorporating subject-specific soft-tissue geometries. Eight early knee OA patients had co-registered MRI and CT scans acquired prior to arthroscopic surgery. This data was used retrospectively to produce comprehensive knee FEA models, where both the geometry and material properties are derived solely from the unique, patient data set. Individual CT-derived bones were assembled in the MR image space and combined with semi-automatically segmented geometries for cartilage, tendon, ligaments, and meniscus. The material properties for the soft-tissues were assigned based on literature values. A pilot study was performed to test various aspects of FEA design, such as homogeneous material mapping of bone, and their effect on the final results. The full-knee FEA models

produced a realistic weight-bearing and stress distribution pattern for all tissues relevant to single-leg stance loading. From this work, we conclude that comprehensive FEA modeling is a valuable tool for assessing the *in vivo* biomechanical ability of the knee. We propose that this method can be used prospectively to monitor the changes in joint composition and load distribution in response to therapeutic or surgical interventions within a patient population.

5.2 Future Directions

5.2.1 FEA of OA patients with actual SBC

A natural progression from our investigation into the effect of SBC on OA bone (Chapter 3) would be the incorporation of this technique with cohort of patients with advanced OA. SBC occur in as many as 47% of individuals with painful knee OA [1], which should allow for a sufficiently large cohort of patients. Based on the literature, these patients are normally referred for MR imaging to confirm the presence of SBC [1-4]. Using the techniques developed in Chapter 4, the pathological knees can be semi-automatically segmented and the FEA models created. Furthermore, if a co-registered CT can be acquired the bones containing SBC can be incorporated into the FEA model with little input from the user, and minimal dose to the patient. Thus, no assumptions regarding the shape (segmented from CT) and composition (assigned based on MR signal) need to be made.

The result of this study would further validate our hypothesis that these lesions initiate and expand as the product of overloading within the bone and reduced cartilage integrity. The CT-derived, peri-cystic BMD values would be accurately measured to confirm an active remodeling process, as found in the rat knee (Chapter 1), and the effect that sclerotic bone has on intra-osseous stress distribution. Furthermore, FE simulations of the knee, with early stage SBC formation, may predict the extent of SBC expansion that can be confirmed with longitudinal images of the patient's knee [1]. Finally, due to the known risk of total knee replacement (TKR) associated with SBC presence, post-TKA

tissue samples could be analyzed with similar histology and immunohistochemistry techniques to verify an active remodeling process [5].

5.2.2 FEA in virtual High-Tibial Osteotomy planning

As previously mentioned, the ability to create patient-specific OA models can allow us to monitor changes to tissue composition and load distribution patterns in response to surgical interventions. The high-tibial osteotomy (HTO) is one such intervention that seeks to correct abnormal varus alignment while shifting the weight axis away from the damaged regions of the joint [6]. HTO is thought of as an alternative therapy that can be used to salvage viable bone and cartilage, with the intention of preventing or prolonging the need for total knee replacement (TKR) [7]. Similar to the bone defect we simulated in Chapter 3, the wedge of bone that is removed during the HTO procedure can be done virtually within a presurgical, FEA model of the patient's knee. The model can be derived easily from presurgical CT scans with heterogeneous material properties mapped in the bones (provided that a tissue calibration phantom is included). Once the patient's FEA model is assembled, a skilled user (guided by an orthopaedic surgeon) can virtually plan and simulate the osteotomy by assigning a wedge of bone negligible material properties; we have implemented a "proof-of-concept" test of this procedure with one of the human datasets used in Chapter 4 (Figure 5-1, i.e. 0.7 MPa). The surgical hardware – usually consisting of several screws and a large metal plate – can be scanned with high-resolution, micro-CT to allow for more accurate geometries that will better depict the helical nature upon FE mesh (Fig. 5-1b). However, finer FE meshes ($\leq 1\text{mm}$) lead to longer solution times, and therefore we propose using a combined edge-length element set, similar to Chapter 3. Therefore, fine-detailed results regarding the stresses and strains in the bone adjacent to the osteotomy, and the hardware components, can be achieved without too great a computing cost. The ultimate goal of this study would be to validate the implementation of a high-throughput, patient-specific FE surgical planning tool.

Single-leg stance loading can be applied to the FEA model based on the actual body-weight of the patient, and the values for intra-osseous stress and strain can be observed surrounding the proposed surgical site. However, recent reports indicate that the use of an

absolute value for applied force may be more sensitive to predicting OA progression [8], which could also be easily tested using the proposed FEA technique. The position of the

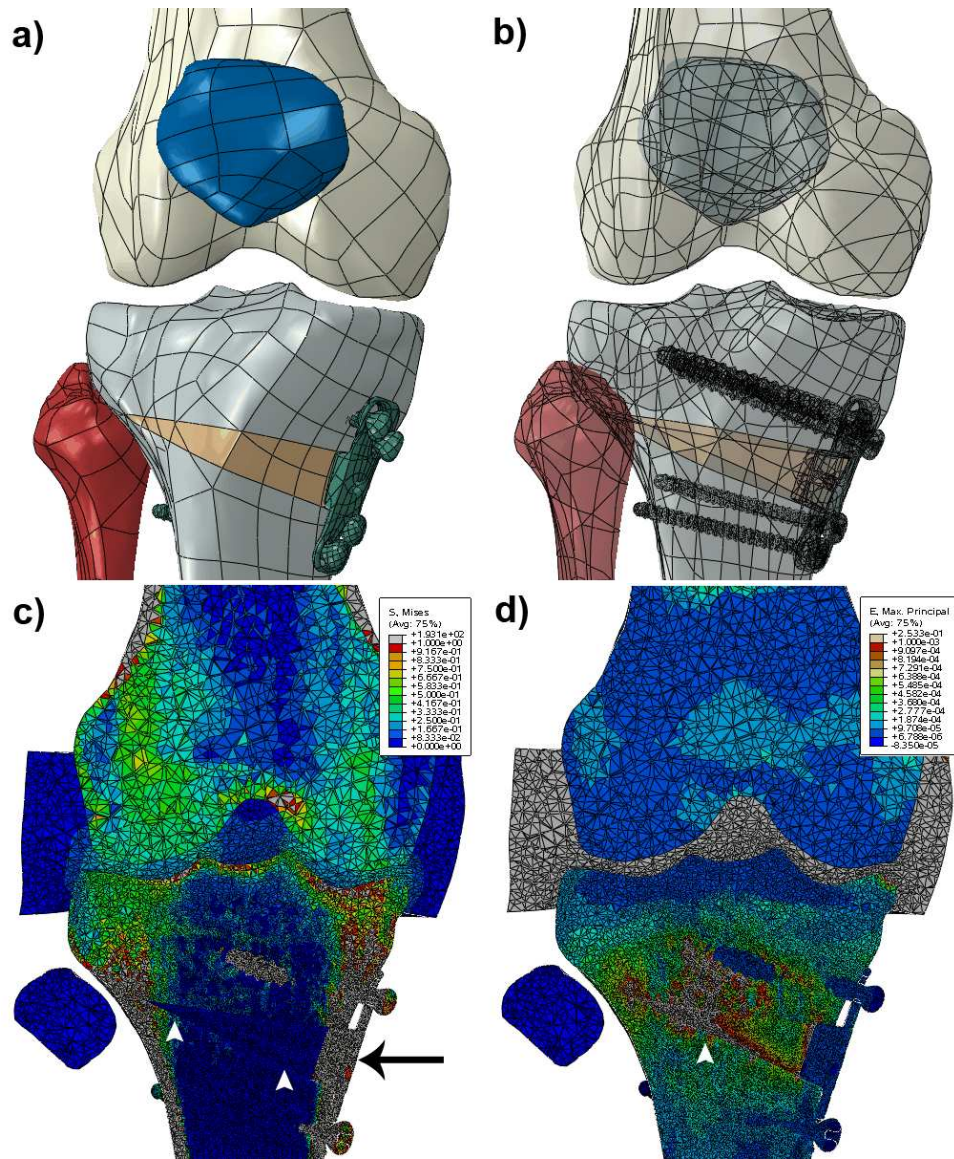


Figure 5-1: Proof of concept for the use of patient-specific FEA in surgical planning of high-tibial osteotomy. Geometries of the bones and surgical hardware (a,b) were derived from CT and micro-CT scans, respectively. Approximately, 2.5 million elements (linear, tetrahedrals) were used and the knee was subjected to a vertical 750 N load. Peak values for stress (c-MPa) and strain (d), were observed adjacent to the hardware and within the bone gap, respectively.

plate and screws can also be modified to determine the likelihood of surgical failure or the possibility of non-union healing within the bone [9].

5.3 References

1. Tanamas, S.K., et al., *The association between subchondral bone cysts and tibial cartilage volume and risk of joint replacement in people with knee osteoarthritis: a longitudinal study*. *Arthritis Res Ther*, 2010. **12**(2): p. R58.
2. Crema, M.D., et al., *Contrast-enhanced MRI of subchondral cysts in patients with or at risk for knee osteoarthritis: The MOST study*. *Eur J Radiol*, 2009.
3. Kornaat, P.R., et al., *Osteoarthritis of the knee: association between clinical features and MR imaging findings*. *Radiology*, 2006. **239**(3): p. 811-7.
4. Marra, M.D., et al., *MRI features of cystic lesions around the knee*. *Knee*, 2008. **15**(6): p. 423-38.
5. Sabokbar, A., et al., *Macrophage-osteoclast differentiation and bone resorption in osteoarthrotic subchondral acetabular cysts*. *Acta Orthop Scand*, 2000. **71**(3): p. 255-61.
6. Giffin, J.R. and F.J. Shannon, *The role of the high tibial osteotomy in the unstable knee*. *Sports Med Arthrosc*, 2007. **15**(1): p. 23-31.
7. Dettoni, F., et al., *High tibial osteotomy versus unicompartmental knee arthroplasty for medial compartment arthrosis of the knee: a review of the literature*. *Iowa Orthop J*, 2010. **30**: p. 131-40.
8. Robbins, S.M., et al., *Comparative diagnostic accuracy of knee adduction moments in knee osteoarthritis: a case for not normalizing to body size*. *J Biomech*, 2011. **44**(5): p. 968-71.
9. Blecha, L.D., et al., *How plate positioning impacts the biomechanics of the open wedge tibial osteotomy; a finite element analysis*. *Comput Methods Biomech Biomed Engin*, 2005. **8**(5): p. 307-13.

6 Appendix

6.1 Ethics Approval



03.01.2010

***This is the 3rd Renewal of this protocol**

*A Full Protocol submission will be required in **02.28.2011**

Dear Dr. **Beier**

Your Animal Use Protocol form entitled:

Molecular Mechanisms of Pain and Fatigue in Osteoarthritis: Interplay of Nerve and Joint

has had its yearly renewal approved by the Animal Use Subcommittee.

This approval is valid from **03.01.2010 to 02.28.2011**

The protocol number for this project remains as **2007-003**

1. This number must be indicated when ordering animals for this project.
2. Animals for other projects may not be ordered under this number.
3. If no number appears please contact this office when grant approval is received.
If the application for funding is not successful and you wish to proceed with the project, request that an internal scientific peer review be performed by the Animal Use Subcommittee office.
4. Purchases of animals other than through this system must be cleared through the ACVS office. Health certificates will be required.

REQUIREMENTS/COMMENTS

Please ensure that individual(s) performing procedures on live animals, as described in this protocol, are familiar with the contents of this document.

The holder of this *Animal Use Protocol* is responsible to ensure that all associated safety components (biosafety, radiation safety, general laboratory safety) comply with institutional safety standards and have received all necessary approvals. Please consult directly with your institutional safety officers.

c.c. V. Pitelka; W. Lagerwerf

The University of Western Ontario
Animal Use Subcommittee / University Council on Animal Care
Health Sciences Centre, ● London, Ontario ● CANADA – N6A 5C1
PH: 519-661-2111 ext. 86770 ● FL 519-661-2028 ● www.uwo.ca / animal

Curriculum Vitae

Name: David D McErlain

Post-secondary Education and Degrees: The University of Western Ontario
London, Ontario, Canada
1998-2002 B.Sc.

The University of Western Ontario
London, Ontario, Canada
2003-2005 M.Sc.

The University of Western Ontario
London, Ontario, Canada
2006-2011 Ph.D.

Honours and Awards: Ontario Graduate Scholarship
2007-2008

Member of CIHR Training program in Musculoskeletal Health Research and Leadership – *Joint Motion Program* (JuMP – STIHR)
2010-2011

Related Work Experience Teaching Assistant
The University of Western Ontario
2002/01-2002/05

Research Assistant
The University of Western Ontario
2004, 2008-2011

Publications:

- 1 **D.D. McErlain**, J.S. Milner, T.G. Ivanov, L. Jencikova-Celerin, S.I. Pollmann, and D.W. Holdsworth, Subchondral cysts create increased intra-osseous stress in early knee OA: A finite element analysis using simulated lesions. *Bone*, 2011. 48(3): p. 639-46.
- 2 M.G. Teeter, D.D. Naudie, **D.D. McErlain**, J.M. Brandt, X. Yuan, S.J. Macdonald, et al., In vitro quantification of wear in tibial inserts using microcomputed tomography. *Clin Orthop Relat Res*, 2011. 469(1): p. 107-12.
- 3 A.C. Waspe, **D.D. McErlain**, V. Pitelka, D.W. Holdsworth, J.C. Lacefield, and A. Fenster, Integration and evaluation of a needle-positioning robot with volumetric microcomputed tomography image guidance for small animal stereotactic interventions. *Med Phys*, 2010. 37(4): p. 1647-59.
- 4 N. Veselka, **D.D. McErlain**, D.W. Holdsworth, J.L. Eger, R.K. Chhem, M.J. Mason, et al., A bony connection signals laryngeal echolocation in bats. *Nature*, 2010. 463(7283): p. 939-42.
- 5 V. Ulici, K.D. Hoenselaar, H. Agoston, **D.D. McErlain**, J. Umoh, S. Chakrabarti, et al., The role of Akt1 in terminal stages of endochondral bone formation: angiogenesis and ossification. *Bone*, 2009. 45(6): p. 1133-45.
- 6 **D.D. McErlain**, C.T. Appleton, R.B. Litchfield, V. Pitelka, J.L. Henry, S.M. Bernier, et al., Study of subchondral bone adaptations in a rodent surgical model of OA using in vivo micro-computed tomography. *Osteoarthritis Cartilage*, 2008. 16(4): p. 458-69.
- 7 C.T. Appleton, **D.D. McErlain**, J.L. Henry, D.W. Holdsworth, and F. Beier, Molecular and histological analysis of a new rat model of experimental knee osteoarthritis. *Ann N Y Acad Sci*, 2007. 1117: p. 165-74.
- 8 C.T. Appleton, **D.D. McErlain**, V. Pitelka, N. Schwartz, S.M. Bernier, J.L. Henry, et al., Forced mobilization accelerates pathogenesis: characterization of a preclinical surgical model of osteoarthritis. *Arthritis Res Ther*, 2007. 9(1): p. R13.
- 9 **D.D. McErlain**, R.K. Chhem, R.N. Bohay, and D.W. Holdsworth, Micro-computed tomography of a 500-year-old tooth: technical note. *Can Assoc Radiol J*, 2004. 55(4): p. 242-5.